Nicolás Ablanque Mejía

UPC   **CTTC**

Numerical Simulation and Experimental Validation of Vapor Compression Refrigerating Systems. Special Emphasis on Natural Refrigerants.

DOCTORAL THESIS

Centro Tecnológico de Transferencia de Calor
Departamento de Máquinas y Motores Térmicos
Universidad Politécnica de Catalunya

Nicolás Ablanque Mejía
Doctoral Thesis

UPC − julio 2010

Numerical Simulation and Experimental Validation of Vapor Compression Refrigerating Systems. Special Emphasis on Natural Refrigerants.

Nicolás Ablanque Mejía

TESIS DOCTORAL

presentada al

Departamento de Máquinas y Motores Térmicos
E.T.S.E.I.A.T.
Universidad Politécnica de Catalunya

para la obtención del grado de

Doctor Ingeniero Industrial

Terrassa, julio 2010

Numerical Simulation and Experimental Validation of Vapor Compression Refrigerating Systems. Special Emphasis on Natural Refrigerants.

Nicolás Ablanque Mejía

Directores de la Tesis

Dr. Joaquim Rigola Serrano

Dr. Carles Oliet Casasayas

Dr. Assensi Oliva Llena

Tribunal Calificador

Dr. Carlos-David Pérez-Segarra
Universitat Politècnica de Catalunya

Dr. Antonio Lecuona Neumann
Universidad Carlos III de Madrid

Dr. José Fernández Seara
Universidad de Vigo

Contents

Acknowledgements

Para empezar quiero agradecerle a todos mis compañeros del CTTC por intentar mantener siempre un buen ambiente de trabajo.

A Assensi por darme la oportunidad de realizar esta Tesis y por haber confiado en mí desde un principio.

A mis directores de Tesis por todo lo que me han aportado a lo largo de estos años, a Quim por motivame continuamente y transmitirme entusiasmo, y a Carles por sus valiosos aportes y su rigurosidad para trabajar.

A Sergio por su apoyo en los modelos de flujo bifásico y a Manolo por su ayuda indispensable en los temas experimentales.

A Deniz y a Rashmin por todo lo compartido y por la gran amistad que ha surgido a lo largo de estos años.

A Santiago, mi compañero de puesto, por su constante actitud de alegría.

A todos los integrantes de la Guardería (Alex, Joan, Lluís, Fei, Hamdi y Mohammed) como también a sus visitantes esporádicos (Pou, Willy, Dani) por haber hecho más divertido el día a día.

A los miembros de la Termosecta por esos pequeños momentos de gloria.

Para terminar quiero aprovechar este espacio para agradecerle a las personas que más quiero.

A mi primo Javier por todas las vivencias compartidas durante tanto tiempo.

A mi hermana Ursula por todos los recuerdos y el gran cariño que le tengo.

A mi padre Enrique y a mi madre Beatriz, a quienes no sólo les dedico este trabajo sino todo lo que soy, por todo el tiempo y apoyo que me han dedicado a lo largo de toda mi vida. Es algo que valoro infinitamente y que siempre tendré en cuenta.

A Nathalia por darle significado a todo lo que he vivido en los últimos años y por ser la compañera con la cual me he embarcado en el proyecto más grande de mi vida.

12

Abstract

The aim of this work is to study the thermal and fluid-dynamic behavior of vapor compression refrigerating systems and their constitutive elements (heat exchangers, expansion devices, compressors and connecting tubes) focused on the use of natural refrigerants (carbon dioxide, isobutane and ammonia). The specific topics analyzed throughout this Thesis have arisen from the growing interest in environmentally friendly refrigerants that has led the CTTC group (Centro Tecnológico de Transferencia de Calor) to undertake significant research efforts and to take part in several projects with national and European institutions. The information reported herein represents a summary of the work carried out by the author during the last years together with the contributions provided by other members of the CTTC group. This Thesis has led to the creation of some publications in International Conferences and Indexed Journals.

The main achievement of this work has been the development of a flexible numerical tool based on several subroutines. The whole numerical infrastructure is the result of coupling the specific resolution procedures for each vapor compression refrigerating system component together with the whole system resolution algorithm. The simulations have been oriented to study the system thermodynamic characteristics as well as some relevant aspects of its particular elements. In addition to the numerical results, a significant experimental work has also been carried out in the CTTC facilities due to the need for experimental validation. The author has been fully involved in data acquisition procedures and has also collaborated in the setting up of the experimental units.

In general, all the studies conducted in this work have been presented following the same structure: i) numerical model and resolution procedure explanation; ii) model validation against experimental data; and iii) simulation results. The specific topics tackled within this Thesis include the implementation of a two-phase numerical model to simulate the thermal and fluid-dynamic behavior of single- and two-phase flows inside ducts, the study of heat transfer coefficient empirical correlations for both cooling of carbon dioxide at transcritical conditions and evaporation of ammonia at overfeed conditions, the implementation of a numerical model to simulate capillary tubes in order to study their behavior at typical operational conditions found in household refrigerators working with isobutane, the development of a two-phase flow distribution model to simulate heat exchangers made up by manifold systems, and the study of vapor compression refrigeration cycles with special emphasis on carbon dioxide transcritical situations.

The set of the numerical models implemented has proven to be a flexible tool as several different aspects of refrigeration vapor compression systems have been successfully simulated and studied. It has also proven to be an accurate tool as the numerical

results achieved have shown good agreement against experimental data.

Chapter 1

Introduction

1.1 Background

Vapor compression systems have been used for refrigeration and cooling purposes since the 19th century. They are still commonly used to provide mechanical cooling in a wide variety of applications such as food processing, cold storage, refrigeration at different levels (domestic, medical, industrial, commercial, transport, cryogenic), air conditioning (in vehicles and public or private enclosed spaces), electronic cooling, oil refineries and chemical processing plants.

A vapor compression refrigeration system is made up of four basic components connected in series (see Figure 1.1): a compressor, a heat exchanger to reject heat (usually a condenser or a gas-cooler), an expansion device, and a heat exchanger to absorb heat (usually an evaporator). The system works with a refrigerant fluid that flows through all the components. On one side, the compressor receives the refrigerant fluid from the evaporator and raises both its pressure and temperature, in order to attain appropriate conditions to reject heat during the condensation process, and on the other side, the expansion device causes the refrigerant fluid temperature and pressure to drop, in order to become a low-temperature vapor/liquid mixture able to absorb heat in the evaporator.

Vapor compression refrigeration systems have been widely studied since their first appearance. The increasing knowledge of the thermal and fluid-dynamic behavior of such equipments is closely related to the continuous theoretical and experimental research. In fact, the resolution of the main equations used to describe the involved phenomena (continuity, momentum and energy equations) is extremely complex, hence the experiences and results accumulated over the last years are essential for further understanding. In the latest decades vapor compression refrigeration is facing new challenges due to the increasing concern about the environment preservation. The efforts to face this major issue are focused on replacing the synthetic refrigerants (which increase the global warming and are harmful to the ozone layer) with more
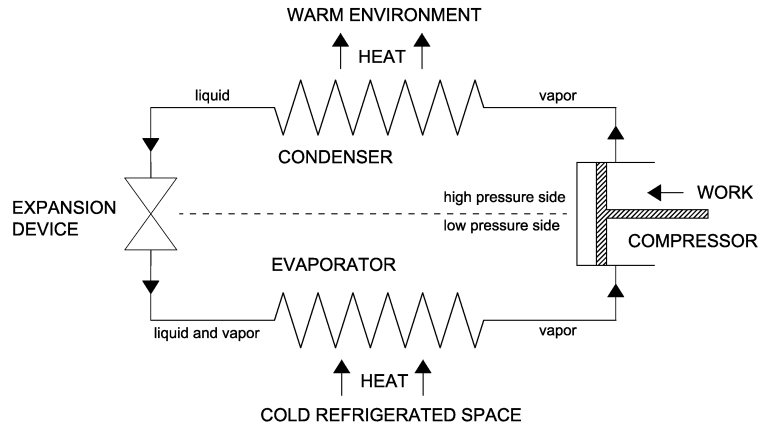
Figure 1.1: Typical vapor compression refrigeration cycle structure.

environmentally friendly refrigerants like the natural substances and also on designing more efficient refrigeration systems in order to reduce energy consumption.

This Thesis is defined as a software development and improvement focused on the set up of a numerical model able to predict the thermal and fluid-dynamic behavior of refrigerating systems. The numerical infrastructure that has been developed is the result of coupling the specific resolution procedures for each system component together with the system resolution algorithm. The numerical simulations that have been carried out were oriented to study refrigerating systems and to report relevant information of their thermodynamic characteristics as well as detailed aspects of their constitutive elements like the heat exchangers. The emphasis was put on the use of natural refrigerants. The particular topics studied within the Thesis framework were: the set up of a two-phase flow numerical model and the implementation of appropriate empirical correlations for natural refrigerants, the study of capillary tubes for domestic refrigeration with isobutane, the development of a numerical model for predicting two-phase flow distribution in heat exchanger manifolds, and the implementation of a numerical model to study the influence of an internal heat exchanger in small capacity carbon dioxide vapor compression refrigerating systems. The experimental facilities available at the CTTC and the experimental results reported in the open literature were used to validate the numerical models.

The work presented in this document represents a contribution to refrigeration knowledge and makes part of an important research field of the Centro Tecnológico de Transferencia de Calor (CTTC). In fact, the growing interest in refrigeration with

natural refrigerants has led the CTTC research group to take part in different projects with national and European institutions. Several of these projects are related to the work reported in this Thesis. For instance, the study carried out on overfeed evaporators with ammonia as the refrigerant fluid is related to the European project *Efficient Refrigerated Food Storage* (EFROST), financed by the Commission of the European Communities (ref. COOP-CT-2004-513106) and coordinated by the CTTC. The study of carbon dioxide vapor compression cycles is part of the research project *Development of Virtual Numerical and Laboratory Experimental Prototypes for One-Stage or Two-Stage Hermetic and Semi-Hermetic Reciprocating Compressors Working with Carbon Dioxide as Fluid Refrigerant. Integration to Numerical and Experimental Trans-Critical Cycles*, carried out with Cubigel S.A. División Unidad Hermética ACC Compressors (ref. C06244). The study on capillary tubes working with isobutane is included in the research project *Optimization of the Domestic Refrigerators Design with Emphasis on Efficiency Improvement and Conception of New Design*, carried out with Fagor Electrodomésticos (ref. C07308). Another project to mention is: *Numerical Simulation and Experimental Validation of Liquid-Vapour Phase Change Phenomena. Application to Thermal Systems and Equipments*, financed by the Spanish government (ref. ENE2008-06667/CON)

Finally, it may be mentioned that some publications in International Conferences and indexed Journals have been generated from this research [1–11].

1.2   Refrigeration and natural refrigerants

During the first decades of the 20th century the main refrigerants in practical use were ammonia (in medium and large systems often with brine as a secondary refrigerant), carbon dioxide (in most marine installations due to its safety), and sulphur dioxide (in household applications and small commercial equipments) [12]. However, in the 1930s new artificial refrigerants, the chlorofluorocarbons (CFCs) and the hydrochlorofluorocarbons (HCFCs), were rapidly introduced in many applications. These halocarbons were seen as safer refrigerants because of their non-flammability and low toxicity. In fact, by the end of the 1980s, they were widely used for small refrigeration, air conditioning, heat pumps and marine equipments, only ammonia has remained the preferred refrigerant in large industrial machines [13].

The Montreal Protocol scheduled the phase out of CFCs in developed countries by the end of 1995 and of HCFCs by the end of 2030 due to their ozone depleting properties [14]. In order to overcome this problem, new synthetic compounds, the so-called hydrofluorocarbons (HFCs), were introduced in the market. They have null ozone depletion potential (ODP) as they lack chlorine (which is thought to harm to the ozone layer). However HFCs are covered by the Kyoto Protocol as they are extremely potent greenhouse gases due to their large global warming potential (GWP).

The efforts on finding an environmentally friendly refrigerant from an artificial substance have not been successfull until now. As a consequence, the industry interest is again focused on naturally occurring substances, namely ammonia, hydrocarbons, carbon dioxide, water and air. Their extended use in the future is possible because of their null ODP and null/low GWP [14]. Some of them, such as the carbon dioxide, were used for many years in the past, and then, completely abandoned and replaced with the halocarbons. Table 1.1 shows a comparison between some characteristics of the most common synthetic and natural refrigerants.

Refrigerant	R-12 (CFC)	R-22 (HCFC)	R-134a (HFC)	R-717 (NH_3)	R-744 (CO_2)	R-600 (butane)
Natural substance	no	no	no	yes	yes	yes
ODP (compared with R-11)	0.9	0.05	0	0	0	0
GWP (compared with R-11)	3	0.34	0.29	0	0^a	<0.03
Toxicity TLV ($ppm, volume$)^b	1000	500	1000	25	5000	1000
Flammability	no	no	no	yes	no	yes
Critical temperature (^oC)	115.5	96.2	100.6	133	31.1	152.1
Critical pressure (bar)	40.1	49.9	40.7	114.2	73.7	38.0
Normal boiling point (^oC)	-30	-40.8	-26	-33.3	-78.4	-0.4
Max. ref. capacity at 0 ^oC (kJ/m^3)	2733	4344	2864	4260	22600	1040

[a]Zero effective GWP, because more than sufficient quantities of it can be recovered from waste gases.
[b]Threshold limit value for exposure of 8h/day, 40 h/week, without any adverse effect.

Table 1.1: Characteristics of some common synthetic and natural refrigerants [14].

The present Thesis considers some of the recent applications of vapor compression systems working with natural refrigerants, namely overfeed evaporators working with ammonia for commercial refrigeration, capillary tubes working with isobutane for domestic refrigeration, ramified evaporators working with carbon dioxide for automotive air conditioning and transcritical cycles working with carbon dioxide for commercial refrigeration.

1.3   Research objectives

The phenomena and geometry complexity of refrigeration units demand a continuous research effort in order to find more appropriate, accurate and solid simulations. In this sense, starting from all the knowhow and computer tools of the CTTC, the present project has the following goals:

- To develop and implement numerical simulation models for predicting the thermal and fluid-dynamic phenomena present in the main vapor compression re-

frigeration system components (compressor, connecting tubes, heat exchangers and expansion devices).

- To develop and implement a numerical simulation method for predicting the thermodynamic behavior of vapor compression refrigeration systems (considering and linking the different numerical subroutines of the system components).

- To validate both the numerical models of the system components and the whole cycle resolution procedure by means of experimental results obtained from both the open literature and the CTTC experimental facilities.

- To carry out experimental tests in the CTTC units (specially designed to study refrigeration systems) in order to obtain new experimental data and to increase the research group experience and knowhow in experimental data acquisition.

- To modify and adapt the numerical models implemented in order to study different applications with natural refrigerants such as ammonia, carbon dioxide and isobutane.

1.4 Outline of the Thesis

Apart of the present chapter the Thesis is composed of six additional chapters, which are briefly described in the following lines.

In Chapter 2 a one-dimensional quasi-homogeneous numerical model to simulate the thermal and fluid-dynamic behavior of single- and two-phase flows inside ducts is presented. Two different resolution algorithms are detailed together with the empirical information needed for closure. The formulation and resolution of the thermal behavior of the solid parts (tubes, insulation) is also presented. A global numerical procedure that links the fluid and solid domains allows to simulate both single and tube-in-tube geometric configurations and also to consider different kind of boundary conditions (temperature, heat flux, external convection) as well as an external thermal insulation layer. The two-phase flow numerical model is an important element of this Thesis as it is constantly used throughout the whole Thesis. The chapter ends with an illustrative study on double tube counter flow heat exchangers working with carbon dioxide at transcritical conditions.

Chapter 3 is devoted to study the accuracy of the available empirical correlations to calculate the heat transfer coefficient inside tubes at typical conditions of ammonia liquid overfeed evaporators. The reliability of some of the most well known correlations is directly tested against experimental data reported in the open literature at the mentioned conditions. The simulations were carried out with the two-phase flow model and the results show that additional experimental works should be done in order to develop an appropriate correlation for such operational conditions.

In Chapter 4 a numerical model to predict the flow behavior inside capillary tubes is detailed. The method is based on the two-phase flow model but including specific modifications in order to predict the particular phenomena found inside capillary tubes. The algorithm allows the prediction of both critical and non-critical flows. The model has been extensively validated against experimental results from the technical literature and a parametric study on household refrigerators capillary tubes working with isobutane has been carried out.

The numerical model presented in Chapter 5 predicts the two-phase flow distribution in devices with multiple branching tubes like heat exchanger manifolds. The algorithm links and simultaneously solves the flow phenomena occurring at tubes and junctions. The flow inside tubes is simulated with the two-phase flow model while the flow convergence/divergence at combining/dividing junctions is predicted with appropriate junction models from the literature. The numerical method has been validated and different parametric studies have been carried out considering several fluids (water, R-134a and carbon dioxide).

In Chapter 6 a numerical model to predict the whole vapor compression refrigeration cycle thermodynamic behavior is presented. The cycle resolution is based on a successive substitution method where all the system elements (heat exchangers, compressor, expansion device and connecting tubes) are called sequentially. The main cycle aspect studied in this chapter is the effect of adding an internal heat exchanger (IHE) to a small capacity single-stage cycle working with carbon dioxide at transcritical conditions. The numerical model is compared against experimental data obtained from the CTTC facilities.

Finally, conclusions about the work done in the present Thesis and comments about the future actions are given in the last chapter.

References

[1] N. Ablanque, C. Oliet, J. Rigola, C. D. Pérez-Segarra, and A. Oliva. Two-phase flow distribution in multiple parallel tubes. *International Journal of Thermal Sciences*, 49(6):909–921, 2010.

[2] J. Rigola, N. Ablanque, C. D. Pérez-Segarra, and A. Oliva. Numerical simulation and experimental validation of internal heat exchanger influence on CO_2 transcritical cycle performance. *International Journal of Refrigeration*, 33(4):664–674, 2010.

[3] N. Ablanque, J. Rigola, C. Oliet, and J. Castro. Critical analysis of the available ammonia horizontal in-tube flow boiling heat transfer correlations for liquid overfeed evaporators. *Journal of Heat Transfer - Transactions of the ASME*, 130(3):34502, 2008.

[4] N. Ablanque, C. Oliet, J. Rigola, and C. D. Pérez-Segarra. Numerical simulation of two-phase flow in multiple T-junctions. In *Proceedings of the 8th IIR Gustav Lorentzen Natural Working Fluids Conference*, 2008.

[5] J. Rigola, N. Ablanque, C. D. Pérez-Segarra, and A. Oliva. Numerical simulation and experimental validation of internal heat exchanger influence in CO_2 transcritical cycles under real working conditions for small cooling applications. In *Proceedings of the 8th IIR Gustav Lorentzen Natural Working Fluids Conference*, 2008.

[6] J. Rigola, N. Ablanque, C. D. Pérez-Segarra, O. Lehmkuhl, and A. Oliva. Numerical analysis of CO_2 trans-critical cycles using semi-hermetic reciprocating compressors for small cooling applications. Study of the internal heat exchanger influence under real working conditions. In *Proceedings of the International Congress of Refrigeration*, 2007.

[7] C. Oliet, N. Ablanque, J. Rigola, C. D. Pérez-Segarra, and A. Oliva. Numerical studies of two-phase flow distribution in evaporators. In *Proceedings of the International Congress of Refrigeration*, 2007.

[8] J. Rigola, G. Raush, C. D. Pérez-Segarra, N Ablanque, A. Oliva, J. M. Serra, J. Pons, M. Jornet, and J. Jover. Numerical analysis and experimental validation of trans-critical CO_2 cycles for small cooling capacities. Hermetic and semi-hermetic CO_2 reciprocating compressor comparison. In *Proceedings of the 7th IIR Gustav Lorentzen Natural Working Fluids Conference*, 2006.

[9] J. Rigola, C.D. Pérez-Segarra, G. Raush, S. Morales, N. Ablanque, and A. Oliva. Simulación numérica y validación experimental de compresores herméticos y semi-herméticos de una sola etapa trabajando con CO_2 en condiciones transcríticas. In *Avances en Ciencias y Técnicas del Frío - III. Vol. 1*, pages 29–38, 2005.

[10] J. Rigola, G. Raush, N. Ablanque, C. D. Pérez-Segarra, A. Oliva, J. M. Serra, M. Escribà, J. Pons, and J. Jover. Comparative analysis of R134a sub-critical cycle vs. CO_2 trans-critical cycle. Numerical study and experimental comparison. In *Proceedings of the 6th IIR Gustav Lorentzen Natural Working Fluids Conference*, 2004.

[11] J. Rigola, S. Morales, G. Raush, C.D. Pérez-Segarra, and N. Ablanque. Numerical study and experimental validation of a transcritical carbon dioxide refigerating cycle. In *Proceedings of the 2004 International Refrigeration and Air Conditioning Conference at Purdue*, 2004.

[12] G. Lorentzen. Revival of carbon dioxide as a refrigerant. *International Journal of Refrigeration*, 17(5):292–301, 1994.

[13] G. Lorentzen. Ammonia: an excellent alternative. *International Journal of Refrigeration*, 11(4):248–252, 1988.

[14] S. B. Riffat, C. F. Afonso, A. C. Oliveira, and D. A. Reay. Natural refrigerants for refrigeration and air-conditioning systems. *Applied Thermal Engineering*, 17(1):33–42, 1997.

Chapter 2

Numerical Simulation of Two-Phase Flow Inside Tubes. Application to Double Pipe Gas-Coolers

ABSTRACT

This chapter is devoted to describe a one-dimensional and transient model for predicting the two-phase flow thermal and fluid-dynamic behavior inside tubes. The fluid domain is discretized in consecutive control volumes where the governing equations (continuity, momentum and energy) are solved simultaneously and coupled by means of the step-by-step or SIMPLE method. The formulation requires the use of empirical correlations for the evaluation of the convective heat transfer, the shear stress and the void fraction. The solid domain is also discretized in consecutive control volumes and solved iteratively with the Gauss-Seidel or TDMA method. The converged solution of the whole system is achieved by solving the fluid and solid domains in a segregated manner.

In this chapter the main numerical aspects of the two-phase flow model are presented together with a numerical verification study. In the last section, an illustrative study on double tube counter flow heat exchangers working with carbon dioxide at transcritical conditions is carried out.

2.1   Introduction

Heat exchangers are widely employed in common applications such as refrigeration, air conditioning and heat pumps. Nowadays, the design of such devices is facing new challenges due to both phenomena: the global warming and the ozone layer depletion. The research efforts are focused on improving the energy efficiency of heat exchangers (in order to reduce the power consumption of systems) and on replacing the harmful artificial working fluids to environmentally friendly refrigerants. For these reasons, accurate and general methods for predicting the thermal and fluid-dynamic behavior of heat exchangers are required.

In several heat exchangers, like condensers and evaporators, the refrigerant fluid circulates through tubes while the secondary fluid circulates through the tubes external part. Among the huge variety of heat exchangers types and geometries, the double pipe counter flow heat exchanger is used in many experimental and numerical applications due to the relatively simple geometric configuration of the secondary fluid path (an annular duct).

The design of double tube heat exchangers can be achieved by means of different methodologies: analytical and numerical. The analytical approaches allow quick results and are useful to study the heat exchanger global behavior. However, the accuracy of these methods is limited because a large number of hypothesis and stringent simplifications are assumed. Examples are the commonly used F-factor and ϵ-NTU methods [1, 2]. More general and accurate procedures require the use of numerical approaches. In these methods, the flow domain is usually represented in a one-dimensional form and subdivided in elemental volumes where the governing equations are solved (mass, momentum and energy). Special consideration is taken in the two-phase flow region because the formulation of the fluid equations is more complex as two different phases are present. In this case, the relation between phases is studied with three main type of models: the homogeneous models [3], the drift-flux models [4] or the separated models [5, 6]. However, the numerical treatment usually offers limited possibilities when multi-dimensionality is considered.

In the present chapter a numerical one-dimensional quasi-homogeneous two-phase flow model is presented [7, 8]. The model allows to predict the thermal and fluid-dynamic behavior of two-phase flows through ducts (single-phase represents a particular case of the formulation). The fluid flow domain is divided in concatenated control volumes where the governing equations are discretized and solved. Two different resolution algorithms are used: step-by-step and SIMPLE. The fluid formulation is fed with empirical information to calculate the parameters needed for closure, namely the heat transfer coefficient, the void fraction, and the friction factor. The solid elements (tubes and insulation) are also taken into account and solved by means of a TDMA algorithm that considers multidimensional heat transfer effects. The solution of the whole domain is obtained iteratively by linking the fluid and solid domains. In fact,

the simulation of different domains (fluid flows, tubes, insulation covers, etc.) together with the large variety of possible external conditions (heat flux, temperature, natural convection, etc.) allow to simulate more complex systems such as double tube heat exchangers.

In the following sections, the model details, verification and results are presented. Firstly, the main aspects of the numerical model are explained: the fluid mathematical formulation and two resolution algorithms (step-by-step and SIMPLE), the empirical information required by the fluid model, both the mathematical formulation and resolution algorithm of the solid parts, and the whole system resolution procedure. Secondly, a numerical verification of the model is carried out. And thirdly, a brief study on gas-coolers working with carbon dioxide is presented.

It is worth to point out that the two-phase flow model detailed in this chapter is a basic element of the present Thesis. The two-phase flow formulation has been constantly used throughout all the chapters of this Thesis. The studies carried out on ammonia correlations (Chapter 3) and the development of the capillary tube numerical model (Chapter 4) have been derived from the two-phase flow model. The model has been also extensively used in the two-phase flow distribution model (Chapter 5) and in the vapor compression refrigerating cycle simulations (Chapter 6).

2.2 Two-phase fluid flow mathematical formulation

The main assumptions considered in the two-phase flow model are listed as follows:

- The fluid flow is one-dimensional.

- The two-phase flow model is quasi-homogeneous.

- The fluid is newtonian.

- The radiation medium is non-participant.

- The radiant heat exchange between surfaces is neglected.

- The axial heat conduction through the fluid is neglected.

The two-phase flow thermal and fluid-dynamic behavior is described from the conservative equations of mass, momentum and energy which are respectively expressed as follows:

$$\frac{\partial}{\partial t} \int_v \rho dV + \int_s \rho \vec{v} \cdot \vec{n} dS = 0 \tag{2.1}$$

$$\frac{\partial}{\partial t} \int_v \vec{v} \rho dV + \int_s \vec{v} \rho \vec{v} \cdot \vec{n} dS = \vec{F_s} + \vec{F}_{body} \tag{2.2}$$

$$\frac{\partial}{\partial t} \int_v \left(h + \frac{v^2}{2} - \frac{p}{\rho} + g \cdot y \right) \rho dV + \int_s \left(h + \frac{v^2}{2} + g \cdot y \right) \rho \vec{v} \cdot \vec{n} dS = \dot{Q} - \dot{W}_{shaft} \quad (2.3)$$

Where the flow work ($\dot{W}_{flow} = -\int_s \vec{v} \cdot pd\vec{S}$) of the energy equation is included inside its convective term.

2.3 Step-by-step resolution algorithm

In the step-by-step resolution algorithm, the fluid domain is divided in concatenated control volumes where the governing equations are discretized and solved. The resolution is achieved by consecutively solving the control volumes from the inlet to the outlet tube cross sections. The information obtained at each control volume is transferred to its neighbor following the flow direction. In this section, the main aspects of this algorithm (geometric discretization of the fluid domain, discretization of the governing equations, resolution procedure, boundary conditions, etc.) are presented.

2.3.1 Discretization

The fluid flow domain inside tubes is discretized in a one-dimensional form as shown in Figure 2.1. The discretization consists in series of control volumes and nodes. The control volumes are placed consecutively between the tube inlet and outlet cross sections, while the nodes are placed at the control volumes inlet $(i-1)$ and outlet (i) cross sections. Both the fluid properties (e.g. enthalpy and pressure) and the mass flow rate are defined at nodes.

The value of any variable inside a fluid flow control volume is approximated from an arithmetic mean as follows:

$$\bar{\phi} = \frac{\phi_{i-1} + \phi_i}{2} \quad (2.4)$$

2.3.2 Discretized equations

The fluid governing equations presented in Section 2.2 are discretized over the control volumes defined in Section 2.3.1. They are also rearranged in order to obtain the fluid values at each control volume downstream position (i) from the values at its upstream position $(i-1)$. In the following paragraphs the discretization procedure of each equation is explained and its final expression is presented.
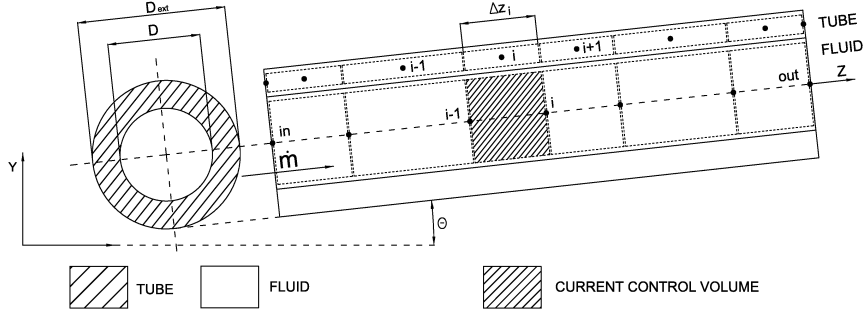
Figure 2.1: Single tube. Fluid and solid domains geometric discretization (step-by-step algorithm).

Mass equation

The transient term of the continuity equation (Equation 2.1) is expressed by means of the two-phase flow density value at the previous time step as follows:

$$\frac{\partial}{\partial t} \int_v \rho dV = \frac{\bar{\rho}_{tp} - \bar{\rho}_{tp}^o}{\Delta t} S \Delta z \qquad (2.5)$$

Where the two-phase flow density (ρ_{tp}) is calculated from the void fraction value (ϵ_g) as follows:

$$\rho_{tp} = \rho_g \epsilon_g + \rho_l (1 - \epsilon_g) \qquad (2.6)$$

The convective term of the continuity equation (Equation 2.1) is calculated between the upstream and downstream cross sections of the control volume as follows:

$$\int_s \rho \vec{v} \cdot d\vec{S} = \dot{m}_i - \dot{m}_{i-1} \qquad (2.7)$$

Finally all the terms of the continuity equation are rearranged in order to obtain the mass flow rate at the downstream face of the control volume:

$$\dot{m}_i = \dot{m}_{i-1} - \frac{\bar{\rho}_{tp} - \bar{\rho}_{tp}^o}{\Delta t} S \Delta z \qquad (2.8)$$

Momentum equation

The transient term in the momentum equation (Equation 2.2) is discretized as shown in the following expression:

$$\frac{\partial}{\partial t} \int_v \vec{v} \cdot (\rho dV) = \frac{\bar{v}\bar{\rho}_{tp} - \bar{v}^o\bar{\rho}_{tp}^o}{\Delta t} S \Delta z = \frac{\bar{\dot{m}} - \bar{\dot{m}}^o}{\Delta t} \Delta z \tag{2.9}$$

And the corresponding convective term is discretized as follows:

$$\int_s \vec{v}(\rho\vec{v} \cdot d\vec{S}) = \dot{m}_i v_i - \dot{m}_{i-1} v_{i-1} \tag{2.10}$$

On one side, the mean mass flow rate at each control volume face is obtained by adding the corresponding gas and liquid mass flow rates ($\dot{m}_g$ and $\dot{m}_l$) which are calculated from the gas weight fraction (x_g):

$$\dot{m}_i = \dot{m}_{g,i} + \dot{m}_{l,i} \tag{2.11}$$

$$\dot{m}_{g,i} = \dot{m}_i x_{g,i} \tag{2.12}$$

$$\dot{m}_{l,i} = \dot{m}_i (1 - x_{g,i}) \tag{2.13}$$

On the other side, both the gas and liquid velocities are calculated by means of the vapor weight fraction (x_g) and the void fraction (ϵ_g):

$$v_{g,i} = \frac{\dot{m}_i x_{g,i}}{\rho_{g,i} \epsilon_{g,i} S} \tag{2.14}$$

$$v_{l,i} = \frac{\dot{m}_i (1 - x_{g,i})}{\rho_{l,i} (1 - \epsilon_{g,i}) S} \tag{2.15}$$

In addition to the transient and convective terms, the momentum equation includes the surface force and the body force terms. Two surface forces are considered and evaluated on each control volume: the force due to the pressure difference between the upstream and downstream faces of the control volume and the force due to friction between the fluid flow and the tube wall. They are calculated as follows:

$$\vec{F}_s = (p_{i-1} - p_i)S - \bar{\tau}P\Delta z \tag{2.16}$$

While the only body force considered in this analysis is due to the gravity:

$$\vec{F}_{body} = -mg \sin(\theta) \tag{2.17}$$

All the discretized terms of the momentum equation are rearranged in order to find the pressure at the control volume downstream position:

$$p_i = p_{i-1} - \left(\frac{\dot{m}_i}{S}\right)^2 \left(\frac{x_{g,i}^2}{\rho_{g,i}\epsilon_{g,i}} + \frac{(1-x_{g,i})^2}{\rho_{l,i}(1-\epsilon_{g,i})}\right)$$
$$+ \left(\frac{\dot{m}_{i-1}}{S}\right)^2 \left(\frac{x_{g,i-1}^2}{\rho_{g,i-1}\epsilon_{g,i-1}} + \frac{(1-x_{g,i-1})^2}{\rho_{l,i-1}(1-\epsilon_{g,i-1})}\right) \quad (2.18)$$
$$- \left(\frac{\bar{\dot{m}} - \bar{\dot{m}}^o}{S\Delta t} + \frac{\bar{\tau}P}{S} + \bar{\rho}_{tp}g\sin(\theta)\right)\Delta z$$

Energy equation

The transient term of the energy equation (Equation 2.3) is discretized as follows:

$$\frac{\partial}{\partial t}\int_v \left(h + \frac{v^2}{2} - \frac{p}{\rho} + g\cdot y\right)\rho dV = \frac{\bar{\rho}_{tp}\bar{h} - \bar{\rho}_{tp}^o\bar{h}^o}{\Delta t}S\Delta z$$
$$+ \frac{\bar{\rho}_g\bar{\epsilon}_g\left(\frac{\bar{v}_g^2}{2}\right) - \bar{\rho}_g^o\bar{\epsilon}_g^o\left(\frac{\bar{v}_g^{o2}}{2}\right)}{\Delta t}S\Delta z$$
$$+ \frac{\bar{\rho}_l(1-\bar{\epsilon}_g)\left(\frac{\bar{v}_l^2}{2}\right) - \bar{\rho}_l^o(1-\bar{\epsilon}_g^o)\left(\frac{\bar{v}_l^{o2}}{2}\right)}{\Delta t}S\Delta z \quad (2.19)$$
$$- \frac{\bar{p} - \bar{p}^o}{\Delta t}S\Delta z$$
$$+ \frac{(\bar{\rho}_{tp}\bar{y} - \bar{\rho}_{tp}^o\bar{y}^o)g}{\Delta t}S\Delta z$$

While the convective term is discretized as follows:

$$\int_s \left(h + \frac{v^2}{2} + g\cdot y\right)\rho\vec{v}\cdot d\vec{S} = \dot{m}_i(h_i) - \dot{m}_{i-1}(h_{i-1})$$
$$+ \dot{m}_{g,i}\left(\frac{v_{g,i}^2}{2}\right) - \dot{m}_{g,i-1}\left(\frac{v_{g,i-1}^2}{2}\right)$$
$$+ \dot{m}_{l,i}\left(\frac{v_{l,i}^2}{2}\right) - \dot{m}_{l,i-1}\left(\frac{v_{l,i-1}^2}{2}\right) \quad (2.20)$$
$$+ \dot{m}_i gy_i - \dot{m}_{i-1}gy_{i-1}$$

Additional hypotheses and modifications have been done to the discretized energy equation in order to have an easier numerical resolution (e.g. the mean density of the

control volume at the current time step is eliminated). They are listed as follows: i) the discretized continuity equation (Equation 2.8) is multiplied by the specific energy of the control volume ($\bar{e} = \bar{h} + \bar{v}^2/2 + g\bar{y}$) and subtracted to the discretized energy equation; ii) the height is considered constant at every time step ($y = y^o$); iii) The shaft work is neglected ($\dot{W}_{shaft} = 0$); iv) the values of the flow variables in the control volumes ($\bar{\phi}$) are calculated as arithmetic means between the upstream and downstream values (Equation 2.4); v) the resulting equation is multiplied by 2; vi) the height step is expressed from the axial step ($\Delta y = sin(\theta)\Delta z$); and vii) the gas and liquid velocities are replaced with the expressions of Equations 2.14 and 2.15, respectively. Finally, the obtained equation is rearranged in order to calculate the enthalpy at the control volume downstream face:

$$h_i = \frac{2\dot{Q} - \dot{m}_i a + \dot{m}_{i-1} b + \frac{S\Delta z}{\Delta t} c}{\frac{\bar{\rho}^o S\Delta z}{\Delta t} + \dot{m}_i + \dot{m}_{i-1}} \tag{2.21}$$

Where:

$$
\begin{aligned}
a = {} & \frac{x_{g,i}}{2}\left(\frac{\dot{m}_i^2 x_{g,i}^2}{\rho_{g,i}^2 \epsilon_{g,i}^2 S^2} - \frac{\dot{m}_{i-1}^2 x_{g,i-1}^2}{\rho_{g,i-1}^2 \epsilon_{g,i-1}^2 S^2}\right) \\
& + \frac{(1 - x_{g,i})}{2}\left(\frac{\dot{m}_i^2(1 - x_{g,i})^2}{\rho_{g,i}^2(1 - \epsilon_{g,i})^2 s^2} - \frac{\dot{m}_{i-1}^2(1 - x_{g,i-1})^2}{\rho_{l,i-1}^2(1 - \epsilon_{g,i-1})^2 S^2}\right) \\
& + (gsin(\theta)\Delta z - h_{i-1})
\end{aligned}
\tag{2.22}
$$

$$
\begin{aligned}
b = {} & \frac{x_{g,i-1}}{2}\left(\frac{\dot{m}_{i-1}^2 x_{g,i-1}^2}{\rho_{g,i-1}^2 \epsilon_{g,i-1}^2 S^2} - \frac{\dot{m}_i^2 x_{g,i}^2}{\rho_{g,i}^2 \epsilon_{g,i}^2 S^2}\right) \\
& + \frac{(1 - x_{g,i-1})}{2}\left(\frac{\dot{m}_{i-1}^2(1 - x_{g,i-1})^2}{\rho_{l,i-1}^2(1 - \epsilon_{g,i-1})^2 s^2} - \frac{\dot{m}_i^2(1 - x_{g,i})^2}{\rho_{l,i}^2(1 - \epsilon_{g,i})^2 S^2}\right) \\
& + (-gsin(\theta)\Delta z + h_{i-1})
\end{aligned}
\tag{2.23}
$$

$$
\begin{aligned}
c =\ & \bar{\rho}^o(h_i^o + h_{i-1}^o - h_{i-1}) + [(p_{i-1} + p_i) - (p_{i-1}^o + p_i^o)] \\
& - \frac{\bar{\rho}_g^o \bar{\epsilon}_g^o}{2} \left(\frac{\dot{m}_{i-1}^2 x_{g,i-1}^2}{\rho_{g,i-1}^2 \epsilon_{g,i-1}^2 S^2} + \frac{\dot{m}_i^2 x_{g,i}^2}{\rho_{g,i}^2 \epsilon_{g,i}^2 S^2} \right) \\
& - \frac{\bar{\rho}_l^o(1 - \bar{\epsilon}_g^o)}{2} \left(\frac{\dot{m}_{i-1}^2(1 - x_{g,i-1})^2}{\rho_{l,i-1}^2(1 - \epsilon_{g,i-1})^2 S^2} + \frac{\dot{m}_i^2(1 - x_{g,i})^2}{\rho_{l,i}^2 1 - \epsilon_{g,i})^2 S^2} \right) \\
& + \frac{\bar{\rho}_g^o \bar{\epsilon}_g^o}{2} \left(\frac{\dot{m}_{i-1}^{o2} x_{g,i-1}^{o2}}{\rho_{g,i-1}^{o2} \epsilon_{g,i-1}^{o2} S^2} + \frac{\dot{m}_i^{o2} x_{g,i}^{o2}}{\rho_{g,i}^{o2} \epsilon_{g,i}^{o2} S^2} \right) \\
& + \frac{\bar{\rho}_l^o(1 - \bar{\epsilon}_g^o)}{2} \left(\frac{\dot{m}_{i-1}^{o2}(1 - x_{g,i-1}^o)^2}{\rho_{l,i-1}^{o2}(1 - \epsilon_{g,i-1}^o)^2 S^2} + \frac{\dot{m}_i^{o2}(1 - x_{g,i}^o)^2}{\rho_{l,i}^{o2} 1 - \epsilon_{g,i}^o)^2 S^2} \right)
\end{aligned}
\tag{2.24}
$$

2.3.3   Resolution procedure

The resolution is carried out on the basis of a step-by-step numerical scheme. The control volumes in which the fluid domain is discretized are solved sequentially, starting from the first control volume, moving forward in the flow direction, and transferring information from one control volume to the next through their shared node. The values of the flow variables at the outlet section of each control volume (e.g. p_i, h_i and $\dot{m}_i$) are obtained from its inlet section values (e.g. p_{i-1}, h_{i-1} and $\dot{m}_{i-1}$) by solving the set of discretized algebraic equations mentioned in the previous section (continuity, momentum and energy).

At each control volume, the fluid formulation requires the use of empirical correlations to evaluate three specific parameters. First, the local gas void fraction ($\epsilon_{g,i}$) which indicates the volume of space occupied by the gas. Second, the local shear stress ($\bar{\tau}_i$) which is usually related to a friction factor (f_i):

$$
\bar{\tau}_i = \frac{f_i}{4} \frac{\bar{m}^2}{2\bar{\rho}_i S^2}
\tag{2.25}
$$

And third, the heat transfer coefficient (α_i) which is used to evaluate the heat transfer between the tube and the fluid:

$$
\bar{\dot{q}}_i = \alpha_i (T_{wall,i} - \bar{T})
\tag{2.26}
$$

Where $T_{wall,i}$ is the wall temperature that corresponds to the current fluid control volume. More information about empirical correlations is presented in Section 2.5. The resolution of each control volume is iterative because the empirical correlations are calculated from the control volume mean values. The convergence at each control volume is verified using the following criterion:

$$\left| \frac{(\phi - \phi^*)}{\phi} \right| \leq \xi \tag{2.27}$$

Where ϕ refers to the dependent variables (pressure, enthalpy, etc.) and ϕ^* represents the dependent variables at the previous iteration.

In the transitory solution, an initial map is defined and the fluid domain is solved for each time step (Δt) until the final condition is reached. Two main final conditions can be considered: final time or steady state. In the latter case, all the flow variables calculated at the fluid domain nodes (ϕ) must be equal to the values calculated at the previous time step (ϕ^o) according to the defined convergence criterion (Equation 2.27). The steady state condition can also be achieved by neglecting the transient term or considering a sufficiently large time step.

2.3.4 Boundary conditions

The boundary conditions for solving directly the step-by-step algorithm are the pressure, enthalpy and mass flow rate at the inlet position of the tube, namely p_{in}, h_{in} and $\dot{m}_{in}$, respectively. The fluid state is defined from its enthalpy and pressure. However, it can be alternatively defined in single- and two-phase flows from its pressure and temperature (p_{in} and T_{in}) and from its pressure and gas weight fraction (p_{in} and $x_{g,in}$), respectively.

The model allows to consider other boundary conditions (p_{in} and p_{out}, p_{in} and $\dot{m}_{out}$, p_{out} and $\dot{m}_{in}$) but additional iterations of the whole fluid domain must be carried out. In this case the convergence can be achieved by means of any iterative algorithm (e.g. Newton-Raphson).

2.4 SIMPLE(C) resolution algorithm

In the SIMPLE resolution algorithm, the fluid domain is divided in control volumes where the conservation equations are discretized and iteratively solved. The main aspects of this algorithm (geometric discretization of the fluid domain, discretization of the governing equations, resolution procedure, boundary conditions, etc.) are presented in this section.

2.4.1 Discretization

The fluid domain is discretized in a one-dimensional form as shown in Figure 2.2. It consists in series of control volumes placed sequentially. Each control volume has a corresponding node at its center where the fluid flow variables are defined. Two different meshes are used: the main mesh as shown in Figure 2.2(a) (where both
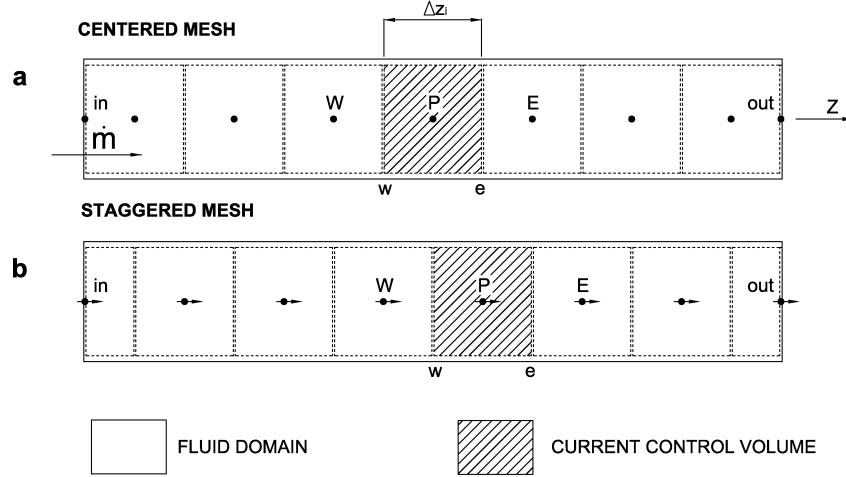
Figure 2.2: Fluid domain geometric discretization (SIMPLE algorithm).

the mass and energy equations are discretized, and the fluid properties are defined at nodes) and the staggered mesh as shown in Figure 2.2(b) (where the momentum equation is discretized, and the mass flow rate is defined at nodes). The staggered grid approach is done to avoid unrealistic solutions due to possible discontinuities when the fluid variables are evaluated (e.g. if only the centered mesh is used the pressure changes could be inadequately calculated from two alternate grid points and not between adjacent ones) as shown by Patankar [9].

2.4.2 Discretized equations

The fluid governing equations presented in Section 2.2 are discretized over the control volumes defined in Section 2.4.1 and rearranged in a generic form:

$$a_P \phi_P = a_E \phi_E + a_W \phi_W + b \tag{2.28}$$

The resulting set of algebraic equations is coupled using a semi-implicit pressure based method (SIMPLE algorithm) and iteratively solved. The discretization and generic expressions of the governing equations are presented in this section.

Pressure correction equation

The continuity expression (Equation 2.1) is discretized according to the centered mesh of Figure 2.2(a):

$$\frac{\rho_P - \rho_P^o}{\Delta t} S\Delta z + \dot{m}_e - \dot{m}_w = 0 \qquad (2.29)$$

This equation is modified in order to obtain an equation for the pressure correction which is needed for the resolution algorithm (see Section 2.4.3). For this purpose, the mass flow is evaluated from Equation 2.45 and the resulting pressure correction equation is:

$$\frac{\rho_P - \rho_P^o}{\Delta t} S\Delta z + \dot{m}_e^* + d_e(p'_P - p'_E) - \dot{m}_w^* - d_w(p'_W - p'_P) = 0 \qquad (2.30)$$

The coefficients d_e and d_w are calculated from Equation 2.46. The pressure correction equation is rewritten in terms of the generic discretized equation:

$$a_P p'_P = a_E p'_E + a_W p'_W + b \qquad (2.31)$$

Where the coefficients are defined as follows:

$$
\begin{aligned}
a_E &= d_e \\
a_W &= d_w \\
a_P &= d_e + d_w \\
b &= -\frac{\rho_P - \rho_P^o}{\Delta t} S\Delta z - \dot{m}_e^* + \dot{m}_w^*
\end{aligned}
\qquad (2.32)
$$

Momentum equation

The momentum equation is discretized according to the staggered mesh of Figure 2.2(b) and considering the gas and liquid velocities defined in Equations 2.14 and 2.15, respectively. The force terms are obtained from Equations 2.16 and 2.17. Thus, the resulting discretized momentum equation is:

$$\frac{\dot{m}_P - \dot{m}_P^o}{\Delta t}\Delta z + \left(\frac{\dot{m}^2 x_g^2}{\rho_g \epsilon_g S} + \frac{\dot{m}^2(1-x_g)^2}{\rho_l(1-\epsilon_g)S}\right)_e - \left(\frac{\dot{m}^2 x_g^2}{\rho_g \epsilon_g S} + \frac{\dot{m}^2(1-x_g)^2}{\rho_l(1-\epsilon_g)S}\right)_w =$$
$$(p_w - p_e)S - \dot{m}_P \frac{f}{4}\frac{|\dot{m}_P|}{2\rho_P S^2} P\Delta z - g\rho_P sin(\theta)S\Delta z \qquad (2.33)$$

This equation can be also expressed in the generic form:

$$a_P \dot{m}_P = a_E \dot{m}_E + a_W \dot{m}_W + b + (p_w - p_e)S \tag{2.34}$$

Where the coefficients are:

$$a_E = -(1 - A_f(F_e)) \left(\frac{\dot{m}_e}{S} \left(\frac{x_g^2}{\rho_g \epsilon_g} + \frac{(1 - x_g)^2}{\rho_l(1 - \epsilon_g)} \right) \right)_e$$

$$a_W = A_f(F_w) \left(\frac{\dot{m}_w}{S} \left(\frac{x_g^2}{\rho_g \epsilon_g} + \frac{(1 - x_g)^2}{\rho_l(1 - \epsilon_g)} \right) \right)_w$$

$$a_P = A_f(F_e) \left(\frac{\dot{m}_e}{S} \left(\frac{x_g^2}{\rho_g \epsilon_g} + \frac{(1 - x_g)^2}{\rho_l(1 - \epsilon_g)} \right) \right)_e - \tag{2.35}$$

$$(1 - A_f(F_w)) \left(\frac{\dot{m}_w}{S} \left(\frac{x_g^2}{\rho_g \epsilon_g} + \frac{(1 - x_g)^2}{\rho_l(1 - \epsilon_g)} \right) \right)_w + \frac{f}{4} \frac{|\dot{m}_P|}{2\rho_P S^2} P \Delta z + \frac{\Delta z}{\Delta t}$$

$$b = \frac{\dot{m}_P^o}{\Delta t} \Delta z - g \rho_P \sin(\theta) S \Delta z$$

The mass flow rate values at the control volume faces ($\dot{m}_e$ and $\dot{m}_w$) can be evaluated by means of different schemes. In this work two main schemes were implemented: the Central-Difference scheme which consists in calculating the control volume face value as the arithmetic mean between the upstream and downstream nodal values, and the Upwind scheme which consists in replacing the face value with the upstream nodal value. The function A_f is used in the momentum equation (Equation 2.35) in order to calculate the coefficients according to the selected scheme. The terms F_e and F_w account for the mass flow rates of the east and west control volume faces, respectively. The schemes and their corresponding functions A_f are presented in Table 2.1.

Central-Difference:	$\dot{m}_e = \frac{1}{2}(\dot{m}_E + \dot{m}_P)$	$A_f(F_e) = \frac{1}{2}$
	$\dot{m}_w = \frac{1}{2}(\dot{m}_W + \dot{m}_P)$	$A_f(F_w) = \frac{1}{2}$
Upwind:	if $F_e > 0$ $\dot{m}_e = \dot{m}_P$	$A_f(F_e) = 1$
	if $F_e < 0$ $\dot{m}_e = \dot{m}_E$	$A_f(F_e) = 0$
	if $F_w > 0$ $\dot{m}_w = \dot{m}_W$	$A_f(F_w) = 1$
	if $F_w < 0$ $\dot{m}_w = \dot{m}_P$	$A_f(F_w) = 0$

Table 2.1: Schemes for evaluating the mass flow rate values at the control volume faces.

The density of a control volume in the stagerred grid is calculated from the arithmetic mean as follows:

$$\rho_P = \frac{\rho_e + \rho_w}{2} \tag{2.36}$$

Energy equation

The energy equation is discretized considering the centered mesh of Figure 2.2(a). It takes the following form:

$$
\frac{\rho_l h_l (1 - \epsilon_g) - \rho_l^o h_l^o (1 - \epsilon_g^o)}{\Delta t} S \Delta z + \frac{\rho_g h_g \epsilon_g - \rho_g^o h_g^o \epsilon_g^o}{\Delta t} S \Delta z
$$
$$
+ \frac{\rho_l (1 - \epsilon_g) v_l^2 - \rho_l^o (1 - \epsilon_g^o) v_l^{o2}}{2 \Delta t} S \Delta z + \frac{\rho_g \epsilon_g v_g^2 - \rho_g^o \epsilon_g^o v_g^{o2}}{2 \Delta t} S \Delta z
$$
$$
+ \frac{\rho_g \epsilon_g g y_g - \rho_g^o \epsilon_g^o g y_g^o}{\Delta t} S \Delta z + \frac{\rho_l (1 - \epsilon_l) g y_l - \rho_l^o (1 - \epsilon_l^o) g y_l^o}{\Delta t} S \Delta z \tag{2.37}
$$
$$
- \frac{p - p^o}{\Delta t} S \Delta z - [\dot{m}_g (h_g + \frac{v_g^2}{2} + g y_g)]_w - [\dot{m}_l (h_l + \frac{v_l^2}{2} + g y_l)]_w
$$
$$
+ [\dot{m}_g (h_g + \frac{v_g^2}{2} + g y_g)]_e + [\dot{m}_l (h_l + \frac{v_l^2}{2} + g y_l)]_e = \dot{Q} - \dot{W}_{shaft}
$$

Additional hypotheses and modifications have been done to the discretized energy equation in order to have an easier numerical resolution. For this purpose, the mass conservation equation (Equation 2.29) is multiplied by the control volume nodal enthalpy value:

$$\frac{\rho_P h_P - \rho_P^o h_P}{\Delta t} S \Delta z + \dot{m}_e h_P - \dot{m}_w h_P = 0 \tag{2.38}$$

Then, the resulting expression (Equation 2.38) is subtracted to the discretized energy expression (Equation 2.37) and rearranged to obtain its generic form:

$$a_P h_P = a_E h_E + a_W h_W + b \tag{2.39}$$

In this case the coefficients are:

$$a_E = -\dot{m}_e A_f(-F_e)$$

$$a_W = \dot{m}_w A_f(F_w)$$

$$a_P = \dot{m}_e A_f(F_e) - \dot{m}_w A_f(-F_w) - \dot{m}_e + \dot{m}_w + \frac{\rho_g^o \epsilon_g^o + \rho_l^o(1 - \epsilon_g^o)}{\Delta t} S \Delta z$$

$$\begin{aligned}
b = &\dot{Q} + \frac{p - p^o}{\Delta t} S \Delta z - \frac{1}{2}\dot{m}_e v_e^2 + \frac{1}{2}\dot{m}_w v_w^2 - \dot{m}_e g y_e + \dot{m}_w g y_w \\
&+ \frac{\rho_g \epsilon_g + \rho_l(1 - \epsilon_g)}{\Delta t} h_P S \Delta z - \frac{\rho_g h_g \epsilon_g + \rho_l h_l(1 - \epsilon_g)}{\Delta t} S \Delta z \\
&+ \frac{\rho_g^o h_g^o \epsilon_g^o + \rho_l^o h_l^o(1 - \epsilon_g^o)}{\Delta t} S \Delta z - \frac{\rho_g \epsilon_g v_g + \rho_l(1 - \epsilon_g)v_l}{2\Delta t} S \Delta z \\
&+ \frac{\rho_g^o \epsilon_g^o v_g^o + \rho_l^o(1 - \epsilon_g^o)v_l^o}{2\Delta t} S \Delta z - \frac{\rho_g \epsilon_g g y_g + \rho_l(1 - \epsilon_g)g y_l}{\Delta t} S \Delta z \\
&+ \frac{\rho_g^o \epsilon_g^o g y_g^o + \rho_l^o(1 - \epsilon_g^o)g y_l^o}{\Delta t} S \Delta z
\end{aligned} \tag{2.40}$$

2.4.3 Resolution procedure

The resolution is carried out on the basis of a SIMPLE resolution algorithm which is explained in the following lines.

The correct pressure field (p) is obtained from both the supposed pressure field (p^*) and the pressure correction field (p'), while the correct mass flow rate field $(\dot{m})$ is obtained from both the calculated mass flow rate field $(\dot{m}^*)$ and the mass flow rate correction field $(\dot{m}')$:

$$\begin{aligned}
p &= p^* + p' \\
\dot{m} &= \dot{m}^* + \dot{m}'
\end{aligned} \tag{2.41}$$

Considering a supposed pressure field (p^*) is possible to predict the mass flow field (m^*) by means of the momentum equation. Thus, according to the staggered grid nomenclature shown in Figure 2.2(b), the momentum equation is expressed as follows:

$$a_P \dot{m}_P^* = a_E \dot{m}_E^* + a_W \dot{m}_W^* + b + (p_w^* - p_e^*)S_P \tag{2.42}$$

If Equation 2.42 (supposed values) is subtracted to Equation 2.34 (correct values), and the relations presented in Equation 2.41 are taken into account, an equation for the correction values is deduced:

$$a_P \dot{m}_P' = a_E \dot{m}_E' + a_W \dot{m}_W' + b + (p_w' - p_e')S_P \tag{2.43}$$

From the latter equation the correction mass flow rate can be expressed as:

$$\dot{m}'_P = d_P(p'_w - p'_e) \tag{2.44}$$

Thus, the exact mass flow rate is deduced:

$$\dot{m}_P = \dot{m}^*_P + d_P(p'_w - p'_e) \tag{2.45}$$

Where the term d_P is evaluated as follows:

$$d_P = \frac{S_P}{a_P} \quad SIMPLE$$
$$d_P = \frac{S_P}{a_P - a_E - a_W} \quad SIMPLEC \tag{2.46}$$

The iterative resolution process for the whole fluid domain is done as follows:

- Guess or define an initial pressure field (p^*).

- The supposed mass flow rate field $(\dot{m}^*)$ is obtained from Equation 2.42.

- The pressure correction field (p') is obtained from Equation 2.31.

- The correct pressure field is calculated $(p = p' + p^*)$.

- The correct mass flow rate field $(\dot{m})$ is obtained from Equation 2.45.

- The supposed and correct values of the pressure and mass flow rate fields are compared. If the convergence criteria is not reached (Equation 2.27), the resolution process starts again with the updated pressure field $(p^* = p)$.

- The enthalpy field is solved from Equation 2.39.

The mentioned algorithm includes equations in the generic form (e.g. Equations 2.42 and 2.31). These equations are solved by means of a node-by-node method (Gauss-Seidel) or a direct method (TDMA). The former is the simplest of all iterative methods (the values of the variable are calculated by visiting each grid point in a certain order), while the latter has a faster convergence.

In the transient solution, an initial map is defined and the whole domain is solved for each time step (Δt) until the final condition is reached. Two main final conditions can be considered: final time or steady state. In the latter case, all the flow variables calculated at the fluid domain nodes (ϕ) must be equal to the values calculated at the previous time step (ϕ^o) according to a defined convergence criteria (Equation 2.27). The steady state condition can also be achieved by neglecting the transient term or considering a sufficiently large time step.

2.4.4 Boundary conditions

The SIMPLE method allows to define the same boundary conditions mentioned for the step-by-step method (p_{in} and p_{out}, p_{in} and $\dot{m}_{out}$, p_{out} and $\dot{m}_{in}$, p_{in} and $\dot{m}_{in}$) but they can all be solved directly without additional iterations. In fact, this method is more general as it considers reflux.
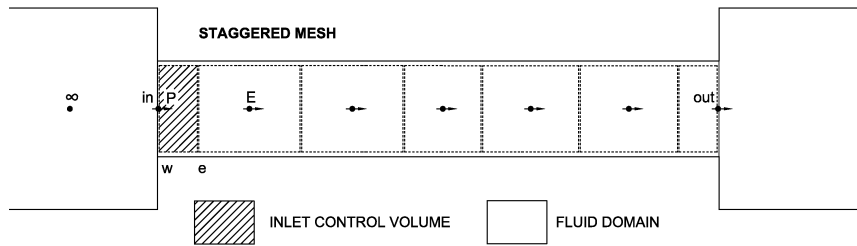
Figure 2.3: Discretization of the boundary condition for (p_{in} and p_{out}).

In this work the boundary condition consisting in defining the pressures at both ends of the fluid domain is studied (e.g. p_{in} and p_{out}). However, this boundary condition can be alternatively defined by means of the outer plenum pressures (e.g p_{∞} in Figure 2.3). For that purpose two equations are defined at the two boundary control volumes of the staggered grid (see Figure 2.3): i) an energy balance considering the plenum pressure (the pressure defined outside of the domain limits, p_{∞}) and the pressure at the boundary cross section (p_{in} or p_{out}), and ii) the discretized momentum expression (Equation 2.33) applied at the boundary control volume.

As shown in Figure 2.3 the position *in* is equal to the positions P and w for the inlet control volume. In this case, the two boundary equations are defined as follows:

$$p_{\infty} - p_P = K_P \frac{\rho v_P^2}{2} = K_P \frac{|\dot{m}_P| v_P}{2S} \tag{2.47}$$

$$\frac{\dot{m}_P - \dot{m}_P^o}{\Delta t} \Delta z + \left(\frac{\dot{m}^2 x_g^2}{\rho_g \epsilon_g S} + \frac{\dot{m}^2 (1-x_g)^2}{\rho_l (1-\epsilon_g) S} \right)_e - \left(\frac{\dot{m}^2 x_g^2}{\rho_g \epsilon_g S} + \frac{\dot{m}^2 (1-x_g)^2}{\rho_l (1-\epsilon_g) S} \right)_w =$$
$$(p_P - p_e)S - \dot{m}_P \frac{f}{4} \frac{|\dot{m}_P|}{2\rho_P S^2} P \Delta z - g \rho_P \sin(\theta) S \Delta z \tag{2.48}$$

Where K_P represents the singularity coefficient. The pressure value at the boundary (p_P) is eliminated by adding Equations 2.47 and 2.48 and a single boundary equation is obtained. The generic form of the resulting expression has the following coefficients:

$$a_E = -(1 - A_f(F_e)) \left(\frac{\dot{m}_e}{S} \left(\frac{x_g^2}{\rho_g \epsilon_g} + \frac{(1 - x_g)^2}{\rho_l(1 - \epsilon_g)} \right)_e \right)$$

$$a_W = 0$$

$$a_P = A_f(F_e) \left(\frac{\dot{m}_e}{S} \left(\frac{x_g^2}{\rho_g \epsilon_g} + \frac{(1 - x_g)^2}{\rho_l(1 - \epsilon_g)} \right)_e \right) \tag{2.49}$$

$$- \left(\frac{\dot{m}_w}{S} \left(\frac{x_g^2}{\rho_g \epsilon_g} + \frac{(1 - x_g)^2}{\rho_l(1 - \epsilon_g)} \right)_w \right) + \frac{f}{4} \frac{|\dot{m}_P|}{2\rho_P S^2} P \Delta z + \frac{\Delta z}{\Delta t} + \frac{|\dot{m}_P|}{2\rho_P S}$$

$$b = \frac{\dot{m}_P^o}{\Delta t} \Delta z - g\rho_P sin(\theta) S \Delta z + (p_\infty - p_e)S$$

Where the function A_f is defined as detailed in Table 2.1. A similar analysis is done for the outlet control volume of the fluid domain.

2.5 Empirical information

In this section a brief description of the empirical information needed for the closure of the two-phase flow model is given. Three parameters are predicted from empirical correlations, namely, the shear stress, the heat transfer coefficient and the void fraction. The reliability of the two-phase flow model simulations is directly related to the accurate prediction of these parameters. Thus, appropriate correlations must be used for each simulation. Special care should be taken when choosing the correlations for two-phase flow because the thermal and fluid-dynamic phenomena are not as well understood as those of single-phase flow. In such cases, no single set of correlations can be used to predict pressure drops or heat transfer rates, instead the correlations are for specific thermal and fluid-dynamic conditions. A comprehensive review on correlations is presented in García [10].

2.5.1 Shear stress

The in-tube two-phase flow pressure drop is mainly due to frictional, accelerational and gravitational effects. The gravitational term accounts for the elevation change that the mixture experiences, the accelerational term accounts for the pressure change

due to density changes, and the frictional term (usually the largest contribution) accounts for the viscous action of the fluid on the duct walls and for the interphase effects. In the quasi-homogeneous two-phase flow model presented in this chapter the frictional effect is expressed by means of the shear stress ($\bar{\tau}$).

For single-phase flow, the shear stress can be determined from the Fanning friction factor (f) as follows:

$$\bar{\tau} = \frac{f}{4} \frac{\dot{m}^2}{2\rho S^2} \tag{2.50}$$

Several correlations for predicting the friction factor have been reported in the literature. The often quoted correlation of Churchill [11] was written to curve fit the Moody diagram without involving any iterative process. In fact, the friction factor is obtained explicitly from the flow Reynolds number and the tube roughness. This correlation spans the entire range of laminar, transition, and turbulent flow in pipes.

For supercritical single-phase flow the correlation of Blasius [12] is usually recommended [13–16].

For two-phase flow, the shear stress can be determined from a two-phase frictional multiplier (ϕ^2):

$$\bar{\tau}_{tp} = \bar{\tau}_k \phi_k^2 \tag{2.51}$$

Where k accounts either for the gas or the liquid phase. Several correlations for predicting the two-phase flow multiplier have been reported in the literature. The correlation of Friedel [17] provides good accuracy as it is based on a very large data set comprising about 25000 data points.

2.5.2 Heat transfer coefficient

The heat transfer between fluids and solids can be determined from the heat transfer coefficient (α). It is a proportionality coefficient between the heat flux ($\dot{q}$) and the driving force of the heat flow (ΔT):

$$\alpha = \frac{\dot{q}}{\Delta T} \tag{2.52}$$

Several correlations for predicting the heat transfer coefficient have been reported in the open literature.

In single-phase flow, relatively simple, reliable and general correlations have been proposed for in-tube forced convection with neither boiling nor condensing effects. In these cases, the heat transfer coefficient between the bulk of the fluid and the tube surface can be directly expressed from the Nusselt dimensionless number:

$$\alpha = \frac{Nu\lambda}{D} \tag{2.53}$$

The correlation of Gnielinski [18] predicts the value of the Nusselt number. It has been tested in smooth tubes and for a wide range of experimental conditions.

For supercritical single-phase flow, many correlations have been proposed during the last decades (e.g. Pitla et al. [19] and Yoon et al. [13]).

However, when two-phase flow is considered (e.g. evaporation and condensation) the phenomena complexity increases (e.g. great variety of flow configurations) and general correlations are not anymore available. Some examples of correlations are the well known expressions of Shah [20] and Gungor and Winterton [21] for condensation and evaporation, respectively. The latest correlations reported in the literature are focused on map oriented approaches where the heat transfer coefficient is calculated according to the fluid flow pattern (e.g. Kattan et al. [22]).

2.5.3 Void fraction

In any gas-liquid system, the gas void fraction (ϵ_g) is the volume of space occupied by the gas. In two-phase fluid flows inside tubes, the void fraction at a given cross section is the ratio of gas flow area to total flow area. In the quasi-homogeneous two-phase flow model the void fraction is necessary to calculate important parameters such as the two-phase flow density (Equation 2.6) and the gas/liquid phase velocity (Equations 2.14 and 2.15).

An extensive review and performance comparison of several void fraction correlations was reported by Melkamu et al. [23]. The correlations/models used to determine the void fraction can be classified in four different groups according to Vijayan et al. [24]. First, the slip ratio correlations approach which consists in assuming that the liquid and vapor phases are separated into two streams that flow through the tube with different velocities, v_g and v_l, the ratio of which is given by the split ratio (v_g/v_l):

$$\epsilon_g = \frac{1}{1 + \left(\frac{1-x_g}{x_g}\right)\left(\frac{\rho_g}{\rho_l}\right)\left(\frac{v_g}{v_l}\right)} \tag{2.54}$$

In the present Thesis all of the results have been obtained from this approach and the split ratio has been estimated with the expression reported by Premoli et al. [25]. Second, the K_{ϵ_H}-correlations which are a constant or some functional multiple of the non-split homogeneous void fraction ($\epsilon_{g,H}$):

$$\epsilon_{g,H} = \left[1 + \left(\frac{1-x_g}{x_g}\right)\left(\frac{\rho_g}{\rho_l}\right)\left(\frac{\mu_l}{\mu_g}\right)\right]^{-1} \tag{2.55}$$

Third, the drift flux correlations which take into consideration the non-uniformity in the flow captured by both a distribution parameter and the drift velocity (defined as the velocity of the gas phase with respect to the volume center of the mixture). And fourth, the general void fraction correlations which are mostly empirical in nature with the basic underlaying physical principles incorporated into the different physical parameters when developing them.

2.6 Solid elements. Formulation and resolution

The energy balance over the solid part of the tube is also considered. The tube is discretized in a way that for each fluid flow control volume there is a corresponding tube temperature (see Figure 2.1). The balance takes into account the heat exchanged with the internal fluid and the heat transferred to/from an external boundary condition (e.g. heat flux, secondary fluid flow or heat transfer coefficient). The discretized energy equation applied at each solid control volume is expressed as follows:

$$\rho c_p \frac{T_{wall,i} - T^o_{wall,i}}{\Delta t} S \Delta z_i = -\lambda_{i_-} \frac{T_{wall,i} - T_{wall,i-1}}{z_i - z_{i-1}} S + \lambda_{i_+} \frac{T_{wall,i+1} - T_{wall,i}}{z_{i+1} - z_i} S$$
$$+ \bar{\bar{q}}_{ext,i} \pi D_{ext} \Delta z_i - \bar{\bar{q}}_i \pi D \Delta z_i$$
$$(2.56)$$

Where λ_{i_-} and λ_{i_+} are the material thermal conductivities evaluated at the solid tube control volume faces by means of an harmonic mean, $\bar{\bar{q}}_i$ is the heat flux between the fluid and the solid, and $\bar{\bar{q}}_{ext,i}$ is the external heat flux. The set of algebraic equations of the solid domain are solved by means of a node-by-node method (Gauss-Seidel) or a direct method (TDMA). In the case of a two-dimensional mesh the line-by-line TDMA method is recommended to reduce the convergence time.

2.7 Global resolution algorithm (fluid and solid)

The thermal and fluid-dynamic behavior of the whole system (inner fluid, tube and surroundings) is obtained by means of a numerical resolution algorithm that couples the fluid and solid domains. It consists in a fully implicit numerical scheme where the fluid and solid domains are solved in a segregated manner, transferring information between each other, until convergence is reached.

More complex configurations than single tubes can be simulated with this algorithm. Figure 2.4 shows the discretization of a double tube heat exchanger. It consists of different domains: i) the inner fluid (discretized and solved with the step-by-step resolution procedure of Section 2.3); ii) the inner tube (discretized in a one-dimensional
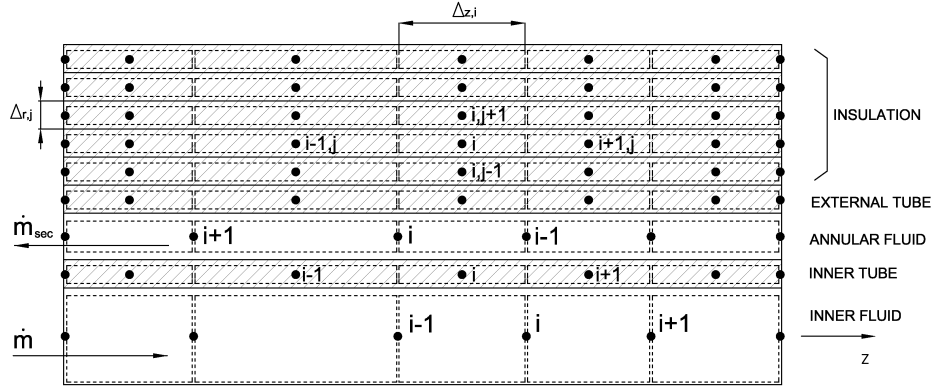
Figure 2.4: Geometric discretization of a double tube heat exchanger with insulation.

way and solved as shown in Section 2.6); iii) the counter flow secondary fluid (discretized and solved with the step-by-step resolution procedure of Section 2.3); and iv) the outer tube which includes an insulation cover and two different materials (discretized in a two-dimensional way and solved as shown in Section 2.6). All kind of external conditions can be considered (e.g. temperature, heat flux, convective/natural heat transfer coefficient).

The transient solution is achieved for each time step (Δt) when all the fluid and solid variables (p, h, $\dot{m}$, T_{wall}) of the previous and current iterations have the same values according to a convergence criterion (see Equation 2.27). The steady state solution is achieved when enough time steps have passed and the fluid and solid variables of the previous and current time steps have the same values according to a convergence criterion. The numerical procedure to solve a double tube heat exchanger is detailed in Figure 2.5.

The thermodynamic properties are iteratively evaluated at each local position by means of the NIST database [26] as function of the local pressure and enthalpy.

2.8 Numerical verification of the two-phase flow simulation model

In this section a numerical analysis of the two-phase flow model is carried out in order to ensure that the model has been correctly implemented. The work is focused on
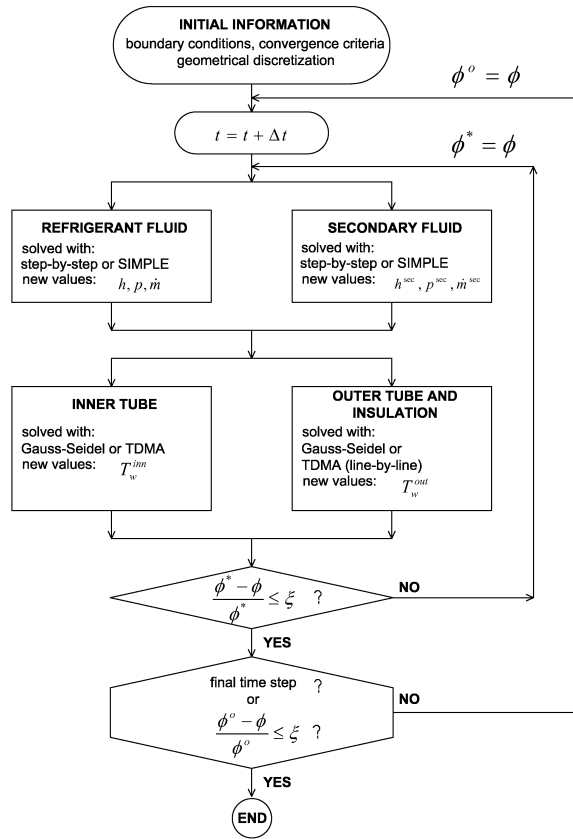
Figure 2.5: Resolution procedure of a double tube heat exchanger with insulation.

studying two different sources of computational errors: convergence and discretization errors. For this purpose two different cases of carbon dioxide flowing through tubes have been simulated with the two-phase flow model. The first case corresponds to an evaporation process, while the second case is a gas-cooling process. In both cases the solid tube and the fluid flow are solved iteratively considering a constant heat flux as the external condition. The main geometric and operational characteristics of the cases are detailed in Table 2.2.

The empirical parameters used in the simulations were obtained from well known correlations found in the open literature. In single-phase flow (gas-cooling process)

	Evaporation	Gas-cooling
Tube length (m)	1	2
Tube inner diameter (m)	0.00386	0.00386
Tube outer diameter (m)	0.00635	0.00635
Heat flux (W/m^2)	5000	-5000*
Inlet pressure (bar)	25.10	100
Inlet enthalpy (kJ/kg)	395.23	520
Mass flow rate (kg/s)	0.0036	0.0041

* Heat transferred from the fluid to the environment.

Table 2.2: Detailed conditions of verification cases.

the heat transfer coefficient and the friction factor were determined from the Yoon et al. [13] and the Blasius [27] correlations, respectively, while in two-phase flow evaporation the heat transfer coefficient and the shear stress were determined from the Gungor and Winterton [21] and the Friedel [17] correlations, respectively. In both cases the correlation of Premoli et al. [25] was used to predict the void fraction.

	Evaporation		Gas-cooling	
Conv. criterion	$h_{out}(J/kg)$	$p_{out}(Pa)$	$h_{out}(J/kg)$	$p_{out}(Pa)$
10^{-3}	422933	2505277	471165	9996721
10^{-5}	422933	2505159	471342	9996720
10^{-7}	422935	2505159	471343	9996720
10^{-9}	422935	2505159	471343	9996720
10^{-11}	422935	2505159	471343	9996720
Mesh density	$h_{out}(J/kg)$	$p_{out}(Pa)$	$h_{out}(J/kg)$	$p_{out}(Pa)$
20	422935	2505158	471344	9996720
50	422935	2505159	471344	9996720
100	422935	2505159	471344	9996720
200	422935	2505159	471343	9996720
400	422935	2505159	471343	9996720
800	422935	2505159	471343	9996720
1600	422935	2505159	471343	9996720
2000	422935	2505159	471343	9996720

Table 2.3: Numerical study of in-tube evaporation and gas-cooling considering the step-by-step resolution algorithm.

Table 2.3 shows the refrigerant fluid outlet conditions of both the evaporation and gas-cooling processes when the step-by-step resolution algorithm is used. For these simulations the boundary condition consisted on the fluid inlet cross section values

$(p_{in}, h_{in}$ and $\dot{m}_{in})$. The convergence of the numerical resolution algorithm is analyzed for two different parameters. First, the convergence criterion (see Equation 2.27) is varied from 10^{-3} to 10^{-11} for a mesh of 2000 control volumes, and second, the mesh is incremented from 20 to 2000 control volumes for a convergence criterion of 10^{-11}. On one side, the results show an asymptotic behavior of the solution as the convergence criterion decreases. On the other, the mesh density influence is less significant due to both the resolution algorithm nature (control volumes are independently calculated from the outlet results of the previous control volume) and the external condition selected (constant heat flux along the whole tube). A reference numerical solution is found for a sufficiently refined mesh (2000 control volumes) and a sufficiently low convergence criterion (10^{-11}).

	Evaporation		Gas-cooling	
Conv. criterion	$h_{out}(J/kg)$	$\dot{m}(kg/s)$	$h_{out}(J/kg)$	$\dot{m}(kg/s)$
10^{-3}	422396	0.003623	471408	0.004109
10^{-5}	422928	0.003601	471335	0.004101
10^{-7}	422938	0.003601	471335	0.004101
10^{-9}	422938	0.003601	471335	0.004101
10^{-11}	422938	0.003601	471335	0.004101
Mesh density	$h_{out}(J/kg)$	$\dot{m}(kg/s)$	$h_{out}(J/kg)$	$\dot{m}(kg/s)$
20	422915	0.003693	471101	0.004182
50	422935	0.003636	471233	0.004132
100	422937	0.003618	471284	0.004116
200	422938	0.003609	471311	0.004108
400	422938	0.003604	471325	0.004104
800	422938	0.003602	471331	0.004102
1600	422938	0.003601	471335	0.004101
2000	422938	0.003601	471335	0.004101

Table 2.4: Numerical study of in-tube evaporation and gas-cooling considering the SIMPLE resolution algorithm.

Table 2.4 shows the simulation results for the same verification cases but using the SIMPLE resolution algorithm (Upwind scheme). In this case the boundary conditions considered were the inlet and outlet pressures obtained in the step-by-step reference case (2000 control volumes and convergence criterion of 10^{-11}). The inlet and outlet plenum pressures were derived from Equation 2.47. The studied parameters were the refrigerant fluid mass flow rate and its outlet enthalpy. It is observed that both parameters present appropriate asymptotic trends as the convergence criterion is decreased and as the mesh is refined.

The tested resolution algorithms (step-by-step and SIMPLE) have been appropriately implemented as their predictions were consistent with each other. In both cases,

evaporation and gas-cooling, the mass flow rate calculated with the SIMPLE method (considering the most refined mesh and the lower convergence criterion) present insignificant differences ($\leq 0.02\%$) with the mass flow rate used as boundary condition in the step-by-step method. The differences found in the outlet enthalpy are even less significant.

It is worth to comment that in addition to the verification study, global balances have been performed for all the equations (mass, momentum and energy) and for all the control volumes finding no inconsistencies in neither of the resolution algorithms.

2.9 Illustrative study. Carbon dioxide double tube gas-coolers

The chlorine-containing CFC and HCFC refrigerants used in applications such as automotive air conditioning, heat pump and low temperature refrigeration systems are now being phased out due to their ozone depleting effect. These refrigerants work under conventional refrigerating cycles where two-phase flow phenomena occur during the heat rejection and absorption processes. Carbon dioxide has recently been investigated as an alternative refrigerant for the mentioned applications. However, this natural refrigerant works under transcritical conditions due to its low critical temperature. In this case, phase change does not occur during the heat rejection so that the heat exchanger is called gas-cooler instead of condenser. More information about transcritical cycles is presented in Chapter 6.

In this section an illustrative analysis of double tube counter flow gas-coolers working with carbon dioxide is presented. A brief comparison of empirical heat transfer coefficient correlations against experimental data is presented followed by an analysis of the in-tube carbon dioxide transcritical cooling heat transfer and by a parametric study on double tube gas-coolers.

2.9.1   Validation of heat transfer coefficient correlations

The usual single-phase heat transfer coefficient correlations are not appropriate for the transcritical zone because large variations of the thermodynamic and transport properties are observed above the critical point. Figures 2.6 shows the carbon dioxide specific heat and density evolution considering a common temperature range (from 30 to 80 ^oC) and three different transcritical pressures (80, 90 and 100 bar), while Figure 2.7 shows the viscosity and thermal conductivity evolution. The values were obtained from the NIST database [26]. The temperature where the isobaric heat capacity reaches a maximum is called the pseudo-critical temperature (T_{pc}). In fact, at each pressure there is a unique pseudo-critical temperature and a pseudo-critical

line (e.g. $T_{pc}(p)$ or $p_{pc}(T)$), which is also considered as a sort of prolongation of the saturation line.
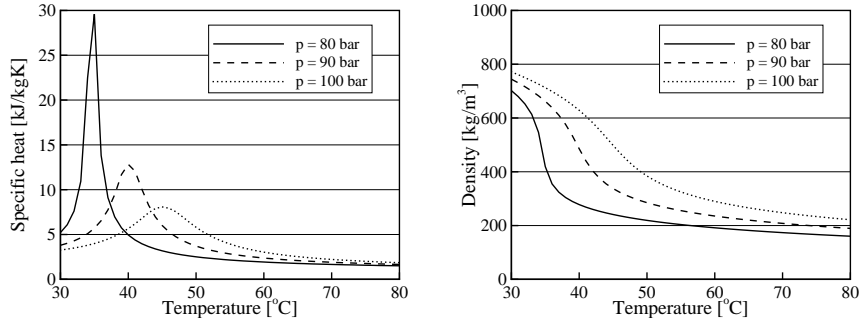
Figure 2.6: Evolution of thermophysical properties of carbon dioxide at trans-critical conditions. Specific heat and density.

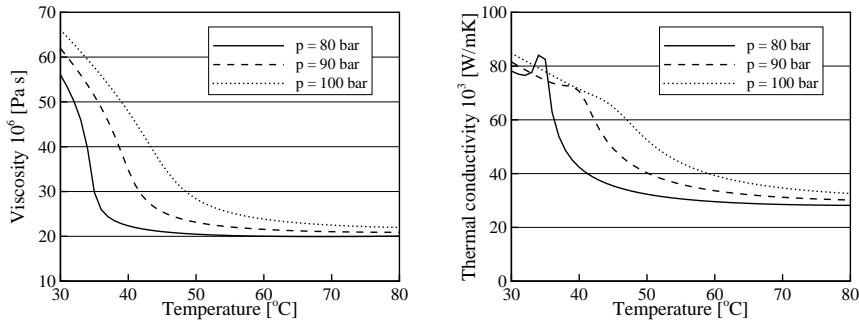**Figure 2.7:** Evolution of thermophysical properties of carbon dioxide at trans-critical conditions. Viscosity and thermal conductivity.

In this section two heat transfer coefficient correlations are compared against experimental data from the technical literature. This validation is only illustrative due to the scarcity of appropriate available experimental data sets (as stated by Cheng et al. [28]).

Experimental data

During the last decade several experimental analyses of in-tube transcritical carbon dioxide gas-coolers have been reported in the open literature, but few provide enough information to be adequately reproduced with numerical models. Some examples are Liao and Zhao [29], Yoon et al. [13], Dang and Hihara [15], Son and Park [16] and Dang et al. [30]. In all of those experimental works a double tube counter flow heat exchanger was used as the test section and water as the secondary fluid. In general no information about the operational conditions of the secondary fluid is provided and in the best-case scenario only the mean heat flux transferred to the water is reported (this is not fully appropriate as the heat flux value varies along the test section).

	Case a	Case b
Conditions		
$\dot{m}_{CO_2}$ (kg/s)	0.02862	0.01963
$\dot{m}_{H_2O}$ (kg/s)	0.08408	0.04011
inner tube material	stainless steel	stainless steel
inner tube ID (mm)	4.72	4.72
inner tube OD (mm)	6.35	6.35
outer tube material	copper	copper
outer tube ID (mm)	15.75	15.75
outer tube OD (mm)	19.05	19.05
Part 1 inlet conditions		
Length (m)	3.6	3.6
h_{CO_2} (kJ/kg)	534.1	539.4
p_{CO_2} (Pa)	10797000	9438800
T_{H_2O} (^oC)	49.54	65.46
p_{H_2O} (Pa)	101300	101300
Part 2 inlet conditions		
Length(m)	9.3	9.3
h_{CO_2} (kJ/kg)	379.1	441.4
p_{CO_2} (Pa)	10740000	9390000
T_{H_2O} (^oC)	19.27	21.72
p_{H_2O} (Pa)	101300	101300

Table 2.5: Gas-cooler experimental cases reported by Pitla et al. [19].

However, among the experimental works found in the open literature, the work done by Pitla et al. [19] includes complete information to be appropriately simulated with the two-phase flow model. The gas-cooler experimental set-up presented by Pitla et al. [19] was made up of eight test sections connected in series. Each test section consisted in a double tube counter flow heat exchanger where the temperature and pressure of the primary and secondary fluids were measured with sensors placed at the corresponding inlet and outlet cross sections. The mean heat transfer coefficient of each test section was deduced from the experimental measurements. It is worth to comment that an external warm-up of the secondary fluid occurred between sections two and three. Thus, the properties of the secondary fluid presented a discontinuity

at that position. Two experimental cases have been selected (cases a and b) and their operational characteristics are detailed in Table 2.5. Each case is divided in two parts: before the water warm-up (part 1) and after it (part 2).

Two-phase flow model numerical predictions

The experimental measurements have been compared against the simulations carried out with the two-phase flow model. The correlation of Blasius [12] has been used to calculate the friction factor, while the correlations of Yoon et al. [13] and Pitla et al. [19] have been used to evaluate the heat transfer coefficient.
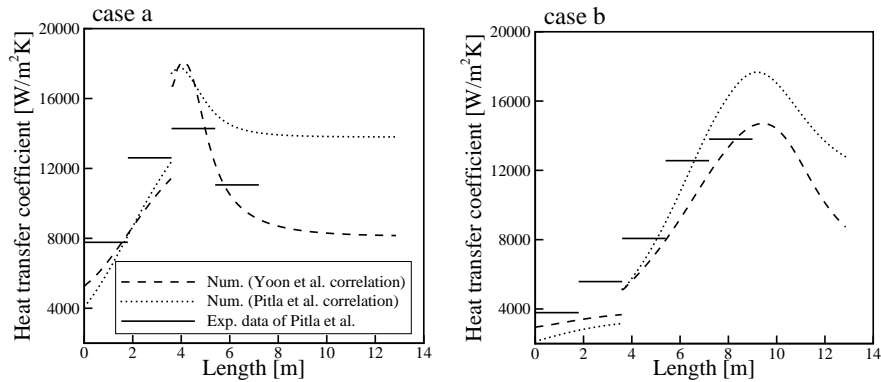
Figure 2.8: Heat transfer coefficient vs. gas-cooler length.

The heat transfer coefficient predictions are shown in Figure 2.8 for the whole gas-cooler length. The experimental mean heat transfer coefficient of each test section is represented by means of an horizontal line. The numerical heat transfer coefficient discontinuity observed at 3.6 m is due to the secondary fluid warm-up previously commented. It is observed that the trends of the heat transfer coefficient predictions are similar for both correlations (e.g. same prediction of the heat transfer coefficient peak). The performance of the correlations is compared by means of the mean prediction error (MPE):

$$MPE = 100 \frac{\sum_{i=1}^{n} \left(\frac{|\alpha_{exp} - \alpha_{calc}|}{\alpha_{exp}} \right)_i}{n} \tag{2.57}$$

The correlation of Yoon et al. has better mean prediction error and standard deviation (17% and 10% respectively) than the correlation of Pitla et al. (23% and
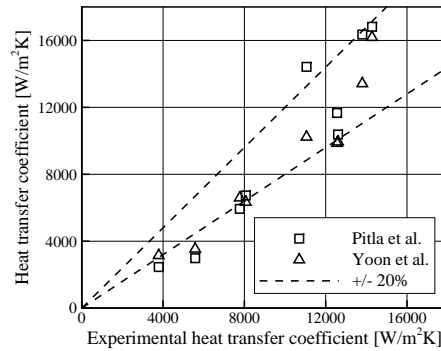
Figure 2.9: Predicted heat transfer coefficient vs. experimental heat transfer coefficient.

12% respectively). The numerical vs. experimental scatter is shown in Figure 2.9 where the experimental values are compared against the mean numerical values of the corresponding section (see Figure 2.8).

2.9.2 Transcritical cooling of carbon dioxide

In this section the heat transfer characteristics of carbon dioxide transcritical in-tube cooling are analized. Firstly, some experimental results from selected studies are presented to illustrate the general heat transfer behavior during the mentioned process. And secondly, a similar analysis is achieved by means of numerical simulations obtained with the two-phase flow model. The experimental trends are consistent with the numerical results.

Experimental studies

The influence of relevant parameters on the heat transfer coefficient during the carbon dioxide in-tube gas-cooling process have been experimentally studied in the literature.

The experimental results of Figure 2.10 (left) show the influence of the refrigerant mass velocity. The measurements were carried out by Yoon et al. [13] for different mass velocities (241, 338 and 464 kg/m^2s) at a pressure of 85 bar. It is observed that the heat transfer coefficient increases with increasing mass velocity near the pseudocritical temperature (far from this region the effect of mass velocity is less notorious). The same behavior was observed in other experimental works where different pressures
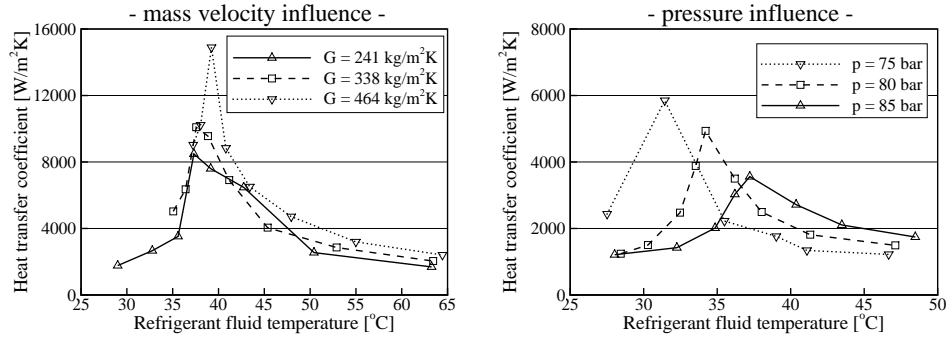
Figure 2.10: Experimental studies on carbon dioxide heat transfer coefficient at transcritical conditions. Mass velocity influence (case a, Yoon et al. [13]) and pressure influence (case b, Huai et al. [14]).

and diameters were considered (e.g. [15, 16, 29]).

The experimental results of Figure 2.10 (right) show the influence of the working pressure. The measurements were reported by Huai et al. [14] for different pressure levels (75, 80 and 85 *bar*). It is observed that for each pressure level the heat transfer coefficient reaches its maximum value near the pseudo-critical temperature (the pseudo-critical temperature increases as the pressure increases). In addition to this, the heat transfer coefficient peak is larger at lower pressure levels due to the proximity of the critical point. This is mainly due to the dramatic increase of the specific heat near the critical point (see Figure 2.6). The same conclusions were deduced in other experimental works (e.g. [15, 16, 29]).

Two-phase flow model numerical results

The two-phase flow model has been used to predict the fluid behavior of a double tube counter flow heat exchanger considering the heat transfer coefficient correlations mentioned above: Yoon et al. [13] and Pitla et al. [19]. The main geometric and operational conditions of the simulated gas-cooler are presented in Table 2.6.

The numerical results plotted in Figure 2.11 show the influence of the refrigerant mass velocity in the heat transfer coefficient. Both correlations present similar trends as the maximum heat transfer coefficient occurs near the pseudo-critical temperature and its value increases with increasing mass velocity. The same behavior is observed in experimental data (see Figure 2.10, left). However, the predicted heat transfer coefficients are higher with the correlation of Pitla et al. [19].
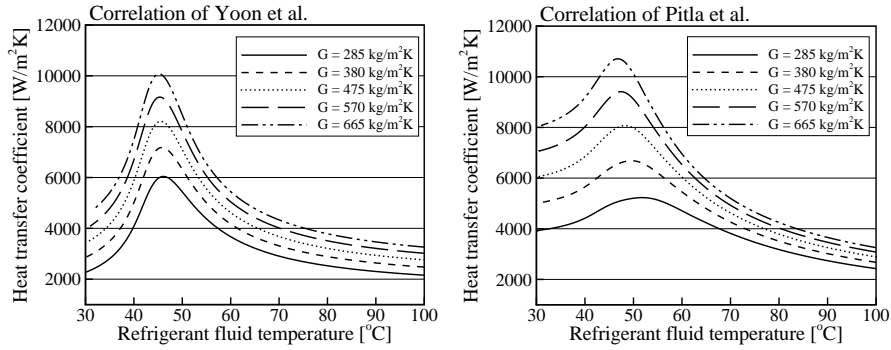
Figure 2.11: Mass velocity influence. Heat transfer coefficient vs. refrigerant fluid temperature.

The numerical results plotted in Figure 2.12 show the influence of the refrigerant pressure in the heat transfer coefficient. Both correlations present similar trends as the maximum heat transfer coefficient occurs near the pseudo-critical temperature and its value decreases with increasing pressure. The same behavior is observed in experimental data (see Figure 2.10, right). Again, higher heat transfer coefficients are predicted with the correlation of Pitla et al. [19].

Figure 2.12: Pressure influence. Heat transfer coefficient vs. refrigerant fluid temperature.

2.9.3 Parametric study on double tube gas-coolers

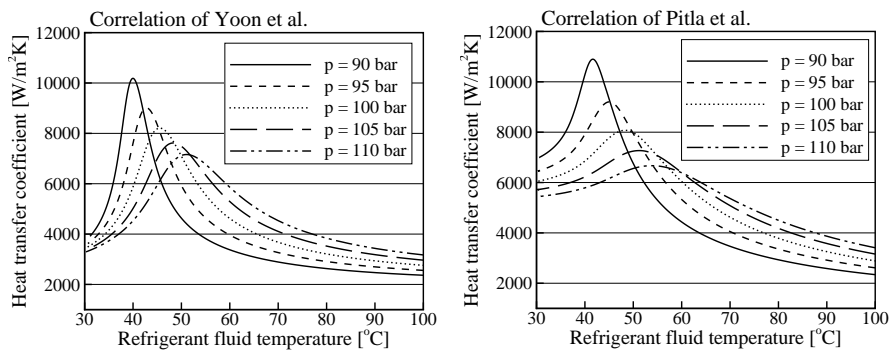The two-phase flow model has been used to carry out a numerical study on double tube counter flow gas-coolers. The geometry of the simulated device is presented in Table 2.6 together with the operational conditions considered. This heat exchanger is equivalent to the experimental gas-cooler used in the vapor compression refrigerating system analyzed in Chapter 6.

Appropriate empirical expressions have been selected for the simulations. On one hand, the correlations of Yoon et al. [13] and Blasius [12] have been used to evaluate the heat transfer coefficient and the friction factor of the refrigerant fluid, respectively. On the other, the correlations of Gnielinski [18] and Churchill [11] have been used to evaluate the heat transfer coefficient and the friction factor of the secondary fluid, respectively. The correlations used for the annular fluid have been appropriately adapted by means of the hydraulic diameter.

Geometric parameters	
Heat exchanger length (m)	1.5,3.0,**4.5**,6.0,7.5
Inner tube inner diameter (m)	0.00386
Inner tube outer diameter (m)	0.00635
Outer tube inner diameter (m)	0.01021
Outer tube outer diameter (m)	0.01270
Insulation diameter (m)	0.05
Operational conditions	
Refrigerant	carbon dioxide
Refrigerant mass velocity (kg/m^2s)	285,380,**475**,570,665
Refrigerant inlet pressure (bar)	90,95,**100**,105,110
Refrigerant inlet temperature (^oC)	130,140,**150**,160,170
Secondary fluid	water
Secondary fluid mass flow rate (kg/s)	0.0333
Secondary fluid inlet temperature (^oC)	30
Secondary fluid inlet pressure (Pa)	101300

Table 2.6: Gas-cooler numerical simulation. Geometric parameters and operational conditions (reference conditions in bold).

The results of the reference case (see Table 2.6) are shown in Figure 2.13 where both the temperature and heat transfer coefficient profiles of both the refrigerant and secondary fluids are plotted. The refrigerant fluid temperature rapidly falls at the gas-cooler inlet portion (from the inlet section to the first meter) due to the high heat fluxes caused by the large temperature gradients. The heat transfer coefficient profiles of the primary and secondary fluids show very different trends along the heat exchanger: i) almost constant for the secondary fluid; and ii) with great variations for the transcritical refrigerant. The heat transfer rate in the heat exchanger is mainly limited by the secondary fluid as its heat transfer coefficient is much lower than that of the refrigerant fluid (over most of the tube length).

The global performance of the gas-cooler is analyzed at different conditions in
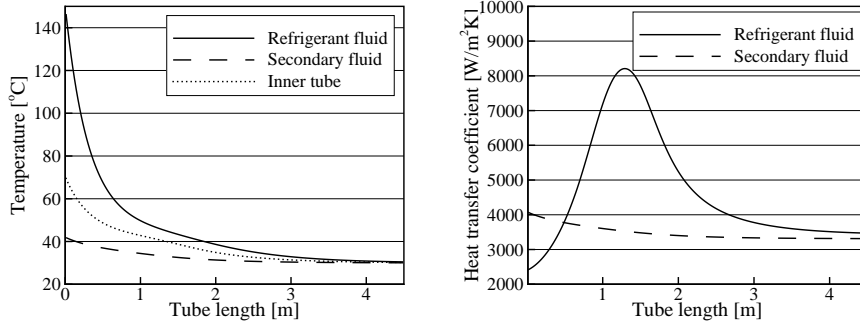
Figure 2.13: Gas-cooler numerical simulation of the reference case. Evolution of temperatures and heat transfer coefficients.

Table 2.7. The secondary fluid inlet conditions have remained constant for all the cases. First, the pressure influence is studied and varied from 90 to 110 bar. As the pressure level increases the Reynolds number decreases and a progressive reduction of the pressure drop is observed (the frictional pressure drop depends mainly on the Reynolds number) but the heat transferred by the whole gas-cooler remains almost constant (an almost imperceptible peak is observed at $p_{in} = 100\ bar$). The effect on heat transfer of the refrigerant inlet pressure is very low due to the secondary flow limiting condition (lower heat transfer coefficient).

Second, the refrigerant inlet temperature is varied from 130 to 170 ^oC. It is observed that both the pressure drop and the heat rejected rise when the refrigerant inlet temperature increases. As expected, the refrigerant fluid outlet temperature gently increases and a greater heat transfer is obtained due to the larger temperature gradients. Third, the refrigerant mass flow rate is varied from 12 to 28 kg/h. In this case, an increase in the mass flow rate results in both a clear improvement of the heat transferred and a noticeable pressure drop increase. And fourth, the heat exchanger length is varied from 1.5 to 7.5 m. The heat transfer increment is significant up to 4.5 m but beyond this position the increment becomes negligible. Thus, a gas-cooler length of 4.5 m is a good compromise between size and maximum heat transfer.

2.10   Conclusions

In this chapter the main details of the two-phase flow model have been presented including two different resolution schemes (step-by-step and SIMPLE). The empirical

p_{in} (**bar**)	Δp (Pa)	$\dot{Q}$ (W)	T_{out} (^oC)
90	6834	1648	31.1
95	6252	1659	30.66
100	5842	1662	30.46
105	5536	1661	30.34
110	5300	1657	30.27
T_{in} (^oC)	Δp (Pa)	$\dot{Q}$ (W)	T_{out} (^oC)
130	5657	1522	30.43
140	5752	1593	30.44
150	5842	1662	30.46
160	5928	1730	30.47
170	6010	1797	30.49
$\dot{m}$ (**kg/h**)	Δp (Pa)	$\dot{Q}$ (W)	T_{out} (^oC)
12	2155	1001	30.09
16	3712	1333	30.2
20	5842	1662	30.46
24	8523	1985	30.91
28	11792	2297	31.6
L (**m**)	Δp (Pa)	$\dot{Q}$ (W)	T_{out} (^oC)
1.5	2913	1380	41.71
3.0	4454	1623	32.51
4.5	5842	1662	30.46
6.0	7203	1669	30.11
7.5	8560	1670	30.05

Table 2.7: Gas-cooler parametric study. Reference conditions: p_{in}=100 bar, T_{in}=150 ^oC, $\dot{m}$=20 kg/h and L=4.5 m

information that feeds the model has also been described. The simulation of solid parts has also been considered and coupled with the two-phase flow model by means of an implicit numerical resolution procedure. The model has been verified by means of a numerical analysis on convergence to ensure its correct implementation. The results show appropriate numerical behavior of the model and consistency between both numerical schemes. The model flexibility and its wide range of possibilities have been shown by studying a double tube counter flow gas-cooler working with carbon dioxide. Special emphasis has been paid to the heat transfer correlations for transcritical cooling of carbon dioxide and to the gas-cooler global performance.

Nomenclature

A_f	scheme function
a	equation coefficient
b	equation source term
c_p	specific heat capacity, $J \cdot kg^{-1} \cdot K^{-1}$
D	tube diameter, m

F	force, $kg \cdot m \cdot s^{-2}$
f	friction factor
g	acceleration due to gravity, $m \cdot s^{-2}$
h	specific enthalpy, $J \cdot kg^{-1}$
K	singularity coefficient
MPE	mean prediction error, %
m	mass, kg
$\dot{m}$	mass flow rate, $kg \cdot s^{-1}$
Nu	Nusselt number
n	number of data
$\vec{n}$	unitary normal vector
P	perimeter, m
p	pressure, Pa
$\dot{Q}$	heat transfer, W
$\dot{q}$	heat flux, $W \cdot m^{-2}$
S	surface, cross section, m^2
T	temperature, K
t	time, s
V	volume, m^3
v	velocity, $m \cdot s^{-1}$
$\dot{W}$	work, W
x_g	gas weight fraction
y	height, m
z	axial position, m

Greek symbols

α	heat transfer coefficient, $W \cdot m^{-2} \cdot K^{-1}$
Δt	temporal step, s
Δz	axial step, m
ϵ_g	gas void fraction
ξ	convergence accuracy criterion
θ	inclination angle, rad
μ	dynamic viscosity, $kg \cdot m^{-1} \cdot s^{-1}$
λ	thermal conductivity, $W \cdot m^{-1} \cdot K^{-1}$
ρ	density, $kg \cdot m^{-3}$
τ	shear stress, Pa
ϕ	discretized variable
ϕ^2	two-phase frictional multiplier

Subscripts

$calc$	calculated value
E	east node
e	control volume east face
exp	experimental value
ext	external
g	gas phase
H	homogeneous
i	axial grid position
j	radial grid position
in	inlet position
l	liquid phase
out	outlet position
P	current node
pc	pseudo-critical
s	surface
tp	two-phase
v	volume
W	west node
w	control volume west face

Superscripts

$'$	correction value
$*$	previous iteration value
inn	inner tube
o	previous time step value
out	outer tube
sec	secondary fluid

References

[1] D. Q. Kern. *Process heat transfer*. McGraw-Hill, 1950.

[2] S. Kakaç and H. Liu. *Heat exchangers: selection, rating and thermal design*. CRC Press, 1998.

[3] S. Levy. *Two-phase flow in complex systems*. Wiley Interscience Publications, New York, 1999.

[4] G. B. Wallis. *One-dimensional two-phase flow*. McGraw-Hill Book Company, New York, 1969.

[5] G. Yadigaroglu and R. T. Lahey Jr. On the various forms of the conservation equations in two-phase flow. *International Journal of Multiphase Flow*, 2(5-6):477–494, 1976.

[6] M. Ishii and T. Hibiki. *Thermo-fluid dynamics of two-phase flow*. Springer, New York, 2006.

[7] F. Escanes, C. D. Pérez-Segarra, and A. Oliva. Numerical simulation of capillary tube expansion devices. *International Journal of Refrigeration*, 18(2):113–122, 1995.

[8] O. García-Valladares, C. D. Pérez-Segarra, and J. Rigola. Numerical simulation of double-pipe condensers and evaporators. *International Journal of Refrigeration*, 27(6):656–670, 2004.

[9] S. V. Patankar. *Numerical heat transfer and fluid flow*. McGraw-Hill, New York, 1980.

[10] O. García-Valladares. *Simulación numérica y validación experimental de evaporadores, condensadores y tubos capilares. integración en sistemas de refrigeración por compresión*. PhD thesis, Universitat Politècnica de Catalunya, 2000.

[11] S. W. Churchill. Frictional equation spans all fluid flow regimes. *Chemical Engineering*, 84(24):91–92, 1977.

[12] F. P. Incropera and D. P. DeWitt. *Fundamentals of Heat and Mass Transfer, 4th ed.*, volume 10. John Wiley and Sons Inc., 1999.

[13] S. H. Yoon, J. H. Kim, Y. W. Hwang, M. S. Kim, K. Min, and Y. Kim. Heat transfer and pressure drop characteristics during the in-tube cooling process of carbon dioxide in the supercritical region. *International Journal of Refrigeration*, 26(8):857–864, 2003.

[14] X. L. Huai, S. Koyama, and T. S. Zhao. An experimental study of flow and heat transfer of supercritical carbon dioxide in multi-port mini channels under cooling conditions. *Chemical Engineering Science*, 60(12):3337–3345, 2005.

[15] C. Dang and E. Hihara. In-tube cooling heat transfer of supercritical carbon dioxide. Part 1. Experimental measurement. *International Journal of Refrigeration*, 27(7):736–747, 2004.

[16] C. H. Son and S. J. Park. An experimental study on heat transfer and pressure drop characteristics of carbon dioxide during gas cooling process in a horizontal tube. *International Journal of Refrigeration*, 29(4):539–546, 2006.

[17] L. Friedel. Improved friction pressure drop correlation for horizontal and vertical two-phase pipe flow. In *Proceedings of the European Two-Phase Flow Group Meeting*, 1979.

[18] V. Gnielinski. New equations for heat and mass transfer in turbulent pipe and channel flow. *International Chemical Engineering*, 16(2):359–368, 1976.

[19] S. S. Pitla, E. A. Groll, and S. Ramadhyani. New correlation to predict the heat transfer coefficient during in-tube cooling of turbulent supercritical CO_2. *International Journal of Refrigeration*, 25(7):887–895, 2002.

[20] M. M. Shah. A general correlation for heat transfer during film condensation inside pipes. *International Journal of Heat and Mass Transfer*, 22(4):547–556, 1979.

[21] K. E. Gungor and R. H. S. Winterton. Simplified general correlation for saturated flow boiling and comparisons of correlations with data. *Chemical Engineering Research and Design*, 65(2):148–156, 1987.

[22] N. Kattan, J. R. Thome, and D. Favrat. Flow boiling in horizontal tubes: part 3 - development of a new heat transfer model based on flow pattern. *Journal of Heat Transfer*, 120(1):156–165, 1998.

[23] A. Melkamu, M. A. Woldesemayat, and A. J. Ghajar. Comparison of void fraction correlations for different flow patterns in horizontal and upward inclined pipes. *International Journal of Multiphase Flow*, 33(4):347–370, 2006.

[24] P. K. Vijayan, A. P. Patil, D. S. Pilkhawal, D. Saha, and V. Venkat Raj. An assessment of pressure drop and void fraction correlations with data from two-phase natural circulation loops. *Heat and Mass Transfer*, 36(6):541–548, 2000.

[25] A. Premoli, D. Francesco, and A. Prima. An empirical correlation for evaluating two-phase mixture density under adiabatic conditions. In *Proceedings of the European Two-Phase Flow Group Meeting*, 1970.

[26] REFPROP v 7.0 NIST. *Thermodynamic properties of refrigerants and refrigerant mixtures database, Standard Reference Data Program*. USA, 2002.

[27] F. P. Incropera and D. P. DeWitt. *Introduction to heat transfer, 3rd ed.* John Wiley and Sons Inc. New York, 1996.

[28] L. Cheng, G. Ribatski, and Thome J. R. Analysis of supercritical CO_2 cooling in macro- and micro-channels. *International Journal of Refrigeration*, 31(8):1301–1316, 2008.

[29] S. M. Liao and T. S. Zhao. An experimental investigation of convection heat transfer to supercritical carbon dioxide in miniature tubes. *International Journal of Heat and Mass Transfer*, 45(25):5025–5034, 2002.

[30] C. Dang, K. Lino, K. Fukuoka, and E. Hihara. Effect of lubricating oil on cooling heat transfer of supercritical carbon dioxide. *International Journal of Refrigeration*, 30(4):724–731, 2007.

Chapter 3

Flow Boiling Heat Transfer Correlations for R-717 in Liquid Overfeed Evaporators

ABSTRACT

The in-tube evaporation of hydrofluorocarbons and other commercial refrigerants has been widely studied in the technical literature and consequently several heat transfer correlations with an acceptable level of accuracy have been reported. However, in the field of natural refrigerants, and specially for ammonia, there is still an important lack of fundamental and empirical information. This problem is particularly important for fin-and-tube-type air-to-refrigerant liquid overfeed evaporation conditions. This chapter is focused on analysing the state-of-the-art of the ammonia heat transfer coefficient correlations for horizontal in-tube boiling at the mentioned working conditions. Firstly, a compilation of the experimental works carried out with ammonia is presented together with a brief summary of the most relevant two-phase flow boiling correlations. Subsequently, in accordance with the selected data, a detailed analysis of each correlation performance has been carried out. The results show that there is an important divergence between the experimental data sets and that the presently available correlations have considerable discrepancies in predicting the heat transfer coefficient at typical overfeed conditions. The main contents of this chapter are published in the *Journal of Heat Transfer - Transactions of the ASME*.

3.1 Introduction

Since the beginning of mechanical refrigeration in the nineteenth century, ammonia has been used as a refrigerant in many applications due to its advantageous heat transfer qualities: it has an extremely high latent heat which provides more refrigerating effect per unit mass flow than any other refrigerant used in traditional vapor compression systems. The relatively low gas density of ammonia - due to its low molecular weight - requires a larger compressor swept volume in comparison with the heavier fluorocarbon refrigerants, but the combination of its high latent heat and volume results in a high volumetric refrigerating effect. It also has the advantage of covering a wide field of applications, from common freezing to high temperature heat pumps, because of its high critical point (133 ^oC and 114.2 bar).

However, ammonia should be used with precaution and appropriate safety conditions because of its toxicity and flammability. These limiting conditions may lead to important changes in refrigerating systems, namely the use of indirect systems in presence of food or public, low-charge refrigerant units, etc. Other aspects to consider are the unsuitable use of copper alloys with ammonia, and its high specific volume at low temperature applications. Detailed information about ammonia properties is found in [1–4] while reviews of its most important advantages and drawbacks are presented in [5–7].

The interest in environmentally friendly refrigerants has greatly increased as the atmosphere preservation is becoming a primary challenge for humanity. Some synthetic refrigerants, specially those containing chlorine which is extremely harmful to the ozone layer, were decided to be phased out in the Montreal Protocol and subsequent international agreements. Ammonia is a natural refrigerant, whose null Ozone Depletion Potential (ODP) and null Global Warming Potential (GWP) make it an excellent choice for replacing the environment damaging refrigerants.

Nowadays, ammonia is still the refrigerant of choice among many different industrial applications such as food processing, dairy, brewery and cold storage refrigeration. Even considering its limitations, this refrigerant has appropriate thermodynamic and ecological characteristics for being an important refrigerant in the present and future.

During the last decades many correlations to calculate the heat transfer coefficient for two-phase flow boiling inside horizontal tubes have been proposed in the open literature. The aim of most authors consists on finding a general correlation that could be applied to any fluid and to any particular flow condition. However, the confident applicability of a correlation is usually related to both the refrigerants and the flow parameter ranges used for its development. The well known correlation of Shah [8, 9] was an attempt to obtain a solid formulation - able to predict the heat transfer coefficient for many refrigerants and for a wide range of operational conditions -. Other efforts that are worth to be mentioned are the correlations proposed by Gungor

and Winterton [10, 11] and by Kandlikar [12]. The latter includes a specific parameter (F_{fl}) that must be chosen depending on the working fluid. Most of the correlations reported in the open literature are continuously tested against new experimental data which can confirm, extend or reduce their reliable operational ranges, or even lead to major modifications of the correlation. For instance, the flow map based correlation presented by Kattan, Thome and Favrat [13–15] has been modified several times [16–18] in order to improve its accuracy, extend its range of applicability and make it easier to implement.

Most of the correlations referenced above were developed considering a wide variety of fluids, but without including ammonia in their databases [8–15]. Few efforts have been made to sort out that situation: Zurcher et al. [16] recommended some modifications to the original correlation of Kattan et al. [13–15] based on new experimental data for ammonia, and Zamfirescu and Chiriac [19] extended the applicability of the correlation proposed by Kandlikar [12] by determining the appropriate value of the fluid parameter (F_{fl}) for ammonia boiling in vertical tubes.

As regards the experimental works focused on the ammonia in-tube heat transfer coefficients, few have been published in the open literature. However, some important contributions should be highlighted. Shah [20] presented abundant data for ammonia but specifying that no devices for measuring or controlling the oil amount were available in the test facility used, Chaddock and Buzzard [21] published some experimental results for ammonia with different oil percent content, Kelly et al. [22] presented a study of pure ammonia evaporation in both smooth and microfin tubes, and Zurcher et al. [16] published some data that were later enlarged in a subsequent article [23]. Other experimental works were carried out by Zamfirescu and Chiriac [19], Kabelac and Buhr [24], and Boyman et al. [25]. In fact, a detailed survey of the ammonia experimental data available in the literature was presented by Kelly et al. [26]. However, as Ohadi et al. [27] stated, no formal database is still available on heat transfer of pure ammonia. This lack of available data is specially serious for common air-cooled liquid overfeed evaporator conditions: low heat fluxes (limited air cooling capacity), low refrigerant mass velocities (high ammonia latent heat of evaporation and low heat flux) and low vapor weight fractions (inlet near saturated liquid and outlet usually around 0.2/0.3) [28]. The difficulties of getting experimental data at these extreme conditions are commented in Kelly et al. [22].

In the present chapter, a selection and comparison of the ammonia experimental data found in the open literature at liquid overfeed conditions (G<150 kg/m^2s, x_g <0.6, $\dot{q}$ <8 kW/m^2 and T_{sat} <10 ^oC) is presented followed by a summary of the available heat transfer correlations for horizontal in-tube boiling. Then, a detailed comparative study of the correlations accuracy in predicting the data is carried out.

3.2 Ammonia available experimental data

Ammonia is widely used to accomplish refrigeration industrial tasks including a broad range of air-cooled evaporators usually working at overfeed conditions: low mass velocities (G<150 kg/m^2s), low heat fluxes ($\dot{q}$ <8 kW/m^2), low qualities (x_g <0.6) and low temperatures (T_{sat} <10 ^oC). In the current section a short review of the empirical available data for ammonia heat transfer coefficients at these conditions is presented. The study is focused on horizontal in-tube boiling of pure ammonia.

3.2.1 Data selection

A complete survey of the tests conducted with ammonia was presented by Kelly et al. [26]. The updated summary presented in Table 3.1 includes the experimental works listed by Kelly et al. [26] and the more recent works - except those at adiabatic conditions and those with heat flux values not reported - [16, 19–25, 29–31].

source	*D* (*mm*)	*G* (kg/m^2s)	$\dot{q}$ (kW/m^2)	T_{sat} (^oC)	*Oil* (%)	x_g (%)	Pos.*
Van Male & Cosijn [29]	15	3.1-140	1-2.9	-20 to -2.5	Unknown	0-100	H
Shah [20]	26.2	31-1545	0.5-2.3	-40 to 0	Unknown	0-100	H
Chiriac & Sandru [30]	-	200-600	7-25	-5 to 5	0	0.2-2	H
Chaddock & Buzzard [21]	13.4	16-136	1.5-25	-40 to -23	0-4.3	0-100	H
Colin & Malek [31]	21.6	27-542	2-30	30 to 75	0	0-100	H/V
Zurcher et al. [16, 23]	14	10-140	5-70	4	0	0-100	H
Kabelac & Buhr [24]	10	50-150	17-75	-40 to 4	0	0-90	H
Zamfirescu & Chiriac [19]	32	4-136	0.5-6.5	-5 to 10	(99.6% pure)	0-51	V
Kelly et al. [22]	10.9	9-61	0.8-5.4	-20 to 5	0	10-95	H
Boyman et al. [25]	14	40-170	10-50	-10 to 10	0-3	15-100	H

* Test tube position: V, vertical; H, horizontal.

Table 3.1: Operational conditions of the experimental works carried out with ammonia.

As shown in Table 3.1, the experimental conditions from some sources are not

typical of air-cooled liquid overfeed evaporators: Kabelac and Buhr [24] tests are not appropriate as they were conducted at very high heat fluxes ($\dot{q} > 17 \ kW/m^2$), Chiriac and Sandru [30] tests were conducted at very high mass velocities (G> 200 kg/m^2s), Zamfirescu and Chiriac [19] tests were performed only at vertical position. Other works are not suitable for the present study as they only report average heat transfer coefficients (Boyman et al. [25]) or were achieved in ammonia evaporators containing unknown amounts of oil (Van male and Cosijn [29]). This latter aspect is of great importance as the mineral oil used in traditional systems may form undesirable oil layers on the heat exchanger surfaces reducing the unit heat transfer capacity. However, despite the scarcity of experimental works conducted at overfeed conditions, some relevant data at appropriate conditions were found in the open literature. The sources of the selected data and their detailed characteristics are presented in Table 3.2.

	D (mm)	G (kg/m^2s)	$\dot{q}$ (W/m^2)	T_{sat} (C)	measurements
Chaddock and Buzzard [21]	13.39	16	12600	-34.4	7
	13.39	32	12600	-26	28
	13.39	65	12600	-21.8	27
	13.39	65	6300	-26.4	11
Zurcher et al. [16, 23]	14	10	7130	4	10
	14	10	8740	4	9
	14	20	5400	4	29
	14	30	9360	4	24
	14	40	8140	4	34
	14	45	11100	4	18
	14	50	12200	4	40
Kelly et al. [22]	10.9	9	2700	-10	1
	10.9	27	2700	-10	2
	10.9	47	2700	-10	3
	10.9	61	2700	-10	3
	10.9	27	860	5	5
	10.9	27	2700	5	7
	10.9	27	5430	5	3
	10.9	27	2700	-20	6
Shah [20]	26.2	40.7	2312	-14.9	8
	26.2	58	2520	-22.2	11
	26.2	57.2	2346	-22.9	11
	26.2	62.3	2298	-4.3	12
	26.2	38.6	2298	-4.7	8
	26.2	39.9	2326	-5	8
	26.2	35.3	2368	-25.2	7
	26.2	50.2	1635	-14	13

Table 3.2: Operational conditions of the experimental tests carried out with ammonia at liquid overfeed conditions.

Shah experimental data

Shah [20] published a huge analyzable data set and recommended to use it as a starting point for the study of ammonia evaporators containing oil. Among the data set, 78 experimental measurements were found to be suitable for the scope of this study. The experiments were performed using an electrically heated single-tube evaporator of 26.2 mm inner diameter tube, with heat fluxes ranging from 1635 to 2520 W/m^2, mass velocities from 35.3 to 62.3 kg/m^2s, and saturation temperatures from -25.2 to -4.3 $^{\circ}C$. The data reduction process was based on the heat transfer coefficient definition:

$$\alpha_{tp} = \frac{\dot{q}}{T_w - T_{sat}} \tag{3.1}$$

The inner tube wall temperature (T_w) was obtained from direct measurements by means of thermocouples, while the fluid saturation temperature (T_{sat}) was deduced from measurements of the inner fluid saturation pressure and simple interpolation methods. The heat flux ($\dot{q}$) was directly determined as it was generated from electricity. Two aspects of this work are worth to be mentioned: i) significant scatter was reported in the tube wall temperature measurements, and ii) the amount of oil in circulation was unknown because - apart from a standard oil separator - no specific devices for controlling the oil content were installed in the facility. However, although having large uncertainties, the data from Shah [20] are very valuable as the tests were clearly conducted at overfeed conditions.

Kelly et al. experimental data

Kelly et al. [22] presented a study of pure ammonia evaporation in both smooth and microfin tubes. The experimental facility consisted in a double-tube heat exchanger with 10.9 mm inner tube diameter and R-134a flowing through the annulus. The tests that have been considered suitable for this study were carried out at the following operational conditions: heat fluxes from 860 to 5430 W/m^2, mass velocities from 9 to 61 kg/m^2s, and saturation temperatures from -20 to 5 $^{\circ}C$. The so-called "sectional-average heat transfer coefficients" reported by Kelly et al. [22] were obtained from the fluid properties measured at the inlet and outlet positions of the test section, and considering a nominal inner fluid vapor weight fraction for the whole test section. The latter value was determined from the inlet and outlet measurements but its change across the test section could be extremely large (e.g. 60% when a low mass flux and a high heat flux were applied). The sectional-average heat transfer coefficient calculations were based on the following equation:

$$\dot{Q} = U_o A_o \Delta T_{lm} \tag{3.2}$$

Where A_o is the tube external surface, $\dot{Q}$ is the total heat transfer (obtained from an energy balance on the annular fluid), and ΔT_{lm} is the log-mean temperature difference. The overall heat transfer coefficient (U_o) was calculated from Equation 3.2 and expressed as a sum of thermal resistances:

$$\frac{1}{U_o A_o} = \frac{1}{\alpha_o A_o} + \frac{1}{\alpha_i A_i} + \frac{ln(r_o/r_i)}{2\pi\lambda_w L} \tag{3.3}$$

Where α_o is the external heat transfer coefficient (obtained from empirical correlations). The heat transfer coefficient of the inner fluid (α_i) was deduced from Equation 3.3 considering negligible tube thermal resistance. Kelly et al. [22] data are of extreme importance as they include precise overfeed conditions. They are useful for observing the general behavior of the ammonia heat transfer coefficient at different test condition parameters. However, the uncertainties of measurements - due to the high vapor weight fraction changes through the test sections and to the difficulty of measuring low temperature differences - are significant.

Chaddock and Buzzard experimental data

Chaddock and Buzzard [21] reported experimental results for ammonia with different oil content. The experimental tests were carried out in an electrically-heated single-tube evaporator of 13.39 mm inner diameter. The data from this author found to be appropriate for the present study is defined with the following operational parameter ranges: mass velocities from 16 to 65 kg/m^2s, saturation temperatures from -34.4 to -21.8 ^oC and heat fluxes from 6300 to 12600 W/m^2. The data reduction procedure was based on the heat transfer coefficient definition (similar to the procedure done by Shah [20]). No high experimental uncertainty was reported by Chaddock and Buzzard [21] but the heat fluxes applied in the experimental tests were higher than 5 kW/m^2.

Zurcher et al. experimental data

Zurcher et al. [16, 23] published some suitable data for the ammonia in-tube evaporation. The experimental facility consisted of a double-tube heat exchanger with water flowing through the annulus. The inner tube diameter was 14 mm, and the measurements selected for the present study were within the following ranges: heat fluxes from 5400 to 12200 W/m^2, mass velocities from 10 to 50 kg/m^2s, and saturation temperature of 4 ^oC. They reported a mean uncertainty of $\pm5\%$ which is significantly lower than the uncertainty values reported by Kelly et al. [22] for the sectional-average heat transfer measurements. The experimental values were determined based on the heat transfer coefficient definition (Equation 3.2) where the inner

tube wall temperature was obtained from direct measurements, while the fluid saturation temperature was deduced from direct measurements of the saturation pressure. The heat flux was calculated at an specific position of the test section by means of a Lagrange polynomial method for predicting the water enthalpy distribution along the annular duct. The data presented by Zurcher et al. [16, 23] has low uncertainty but the heat fluxes applied to the experimental tests were higher than 5.4 kW/m^2.

Summary of the selected data

In summary, 345 experimental heat transfer coefficient data have been selected from the four works of Table 3.2. Data with heat fluxes up to 13 kW/m^2 were included in order to assemble a reasonably large data set. The data reported by Shah [20] and Kelly et al. [22], although having large uncertainties, are valuable as the experimental tests were clearly carried out at liquid overfeed conditions. The other two data groups, Chaddock and Buzzard [21] and Zurcher et al. [16, 23], do not report high experimental uncertainties, but were carried out at heat fluxes higher than those expected for typical overfeed conditions.

3.2.2 Comparative analysis between the selected experimental data

Figure 3.1 shows all the experimental heat transfer coefficients of the selected tests detailed in Table 3.2. The conditions of the test by Zurcher et al. [16] obtained at $\dot{q}$=5400 W/m^2 are very similar to those of the test by Kelly et al. [22] carried out at $\dot{q}$=5430 W/m^2. However, the experimental heat transfer coefficients obtained by Kelly et al. are three to four times larger, as depicted in Figure 3.2.

These two tests do not have the same parameter values. The test by Kelly et al. [22] was carried out with a slightly larger mass velocity compared to that of Zurcher et al. [16], G=27 vs. G=20 kg/m^2s, respectively. This may not explain the huge difference found in the experimental heat transfer coefficients, as at such low flow rates the convective contribution to heat transfer has little influence. The saturation temperatures are almost equal. Furthermore, the distribution of measurements along the studied vapor weight fraction range is not an explanation, as both tests include points along the range shown in Figure 3.2. Although only three measurements were reported by Kelly et al. [22] for this specific case, small variations through the vapor weight fraction range are observed, while the data of Zurcher et al. [16] present a smooth and constant decreasing heat transfer coefficient with increasing vapor weight fraction.

Additional aspects should be considered for the data comparison between these two authors: i) the different procedures for the experimental data reduction, and ii) the significant data experimental uncertainty reported by Kelly et al. [22]. In fact,
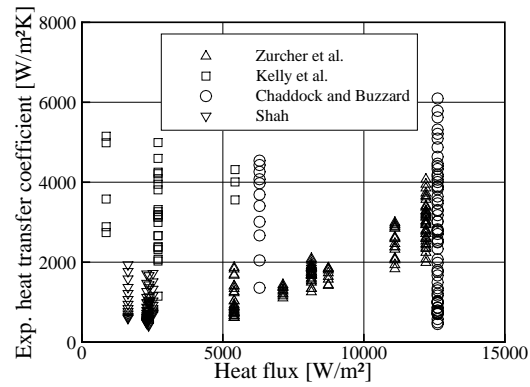
Figure 3.1: Experimental heat transfer coefficients plotted against heat fluxes.

Kelly et al. [22] reported high vapor weight fraction changes across sectional-average test sections - up to 60% - for the tests carried out at relatively low mass fluxes and relatively high heat fluxes such as that presented in Figure 3.2.
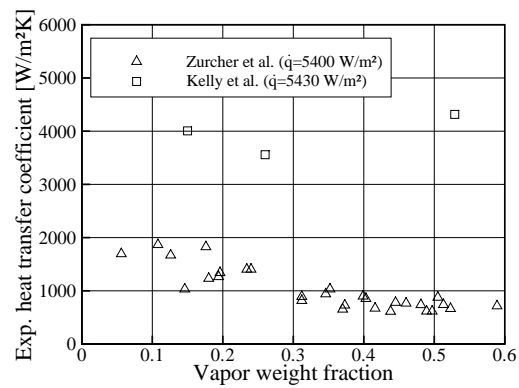

Figure 3.2: Experimental heat transfer coefficients plotted against vapor weight fraction.

Another important aspect in explaining the large difference found in the experi-

mental heat transfer coefficients is the fluid flow pattern types of the tests. On one side, Kelly et al. [22] reported that the predominant flow pattern observed in all the tests was stratified-wavy with some periodic large waves passing through the tube. These waves have an important influence in heat transfer as they are constantly wetting the upper part of the inner tube. On the other side, Zurcher et al. [16] reported the same type of flow regime for their specific test plotted in Figure 3.2. Thus, the frequency and amplitude of the large waves may have a significant influence in the uncertainty and measurement of heat transfer coefficients in both works.

3.3 Heat transfer coefficient correlations for two-phase flow boiling

Usually, the experimental database used in the development of a new heat transfer correlation indicates the suitable parameter ranges and refrigerants for its confident application. The characteristics of the original databases used in three of the most common in-tube boiling correlations are detailed in Table 3.3 (Gungor and Winterton [11], Kandlikar [32] and Kattan et al. [13–15]). As shown, almost all the correlations databases contain a broad range of diameters, heat fluxes, vapor weight fractions and mass velocities. However, a lack of ammonia experimental information is observed (ammonia is not included in any of the three databases presented).

In the present section, the main aspects of the correlations for predicting the flow boiling heat transfer coefficient are presented together with a comparison against the experimental data selected from the technical literature at liquid overfeed conditions (Table 3.2).

3.3.1 Types of flow boiling correlations

Two different phenomena are observed during in-tube evaporation heat transfer: nucleate and convective boiling. Both types may coexist and contribute to the total heat transfer in similar or different proportions. Thus, correlations may be classified depending on the model used to relate these heat transfer modes: the enhancement model, the superposition model, or the asymptotic model. Alternatively, other two-phase correlations use a flow pattern map to predict the vapor and liquid distribution around the tube perimeter. In this case, the heat transfer contribution of the liquid phase (which may include nucleate and convective boiling phenomena), and the contribution of the vapor phase are related in order to calculate the global heat transfer coefficient. Those are the map-oriented correlations.

	Refri.	D (mm)	G (kg/m²s)	$\dot{q}$ (kW/m²)	x_g (%)	Pos.*
Gungor and	Water	2.9-32	59-8179	4.7-2280	0-69.9	V/H
Winterton	R-12	14-20.5	91-4850	1.1-200	1.7-99.3	V/H
[11]	R-22	11.7,18.6	113-1699	1.9-34.6	20.3-67.6	H
	R-11	14-25	12.4-726	0.3-70.1	9-98	H
	R-113	15.7	205-1246	2.9-56.7	0.1-70.2	V
	R-114	19.9	157-4757	8.7-81.6	2.5-88.8	V
	Et.glycol	20.4	206-1030	136-576	0-26.9	V
Kandlikar	Water	5-32	67-8179	4.7-2280	0.1-69.9	V/H
[32]	R-11	6-25	13-4579	0.9-93	0.2-95	H
	R-12	6.7-20.5	104-4850	0.3-111	1.7-98.7	V/H
	R-13B1	9	353-1220	10-51.3	1-60	H
	R-22	10.2-20	80-867	2-70.6	0.2-67.6	V/H
	R-113	8.1	165-1523	6.7-51.1	0.1-71	V
	R-114	20	157-1313	0.8-82.1	1.7-71	V
	R-152	9	140-713	4.7-89.9	1-86	H
	Neon	4,6	77-131	0.4-49	12-95	H
	Nitrogen	14	40-450	0.3-40	10-95	H
Kattan et al.	R-134a	10.9,12	100-500	0.4-36.5	4-100	H
[13–15]	R-123	12	101-300	3.7-24.6	7-98	H
	R-402A	12	102-318	4.4-28.5	1.7-90	H
	R-404A	12	102-320	3.4-30.5	1.6-92.1	H
	R-502	12	100-300	4.3-27.7	1.8-98.6	H

* Test tube position: V, vertical; H, horizontal.

Table 3.3: Detail of the experimental in-tube saturated boiling data used to develop three of the most common heat transfer coefficient correlations.

Enhancement model

The graphical method developed by Shah [8], known as the CHART correlation, is suitable for a large number of fluids and flow parameter ranges. Although ammonia was not included among the fluids used to develop this correlation, it was denoted that the prediction of the heat transfer coefficient for pure ammonia was reliable [26]. Later, Shah [9] presented its graphical correlation (CHART) as a set of equations in order to make its implementation easier. More than 800 data points from 18 independent sources were tested. The result was an expression of the enhancement model type where the two-phase heat transfer coefficient (α_{tp}) is equal to the liquid convective boiling heat transfer coefficient (α_{cb}) multiplied by a two-phase enhancement factor (E):

$$\alpha_{tp} = E\alpha_{cb} \tag{3.4}$$

The enhancement factor depends on the flow boiling regimes defined by Shah (the convective boiling regime, the bubble suppression regime and the pure nucleate regime). It is calculated from three dimensionless parameters: the convective number

(Co), the boiling number (Bo), and the liquid Froude number (Fr_l). The liquid convective heat transfer coefficient of Equation 3.4 is obtained from the Dittus-Boelter equation:

$$\alpha_{cb} = 0.023 Re_l^{0.8} Pr_l^{0.4} \frac{\lambda_l}{D} \tag{3.5}$$

Where only the liquid phase is considered for the calculation of both the Reynolds and Prandtl numbers.

Superposition model

The superposition model was first presented by Chen [33] and consists in adding the convective and nucleate boiling heat transfer coefficients:

$$\alpha_{tp} = \alpha_{cb} + \alpha_{nb} \tag{3.6}$$

Gungor and Winterton [10] proposed to calculate the nucleate boiling contribution with the pool boiling equation of Cooper [34] multiplied by a suppression factor (S), and similarly, the convective contribution with the Dittus-Boelter equation multiplied by an enhancement factor (E). The correlation was developed from many fluids data including water, R-11, R-12, R-22, R-113, R-114, and ethylene glycol in both horizontal and vertical positions (data through annular ducts were also included). Pure ammonia was not considered. In a subsequent article, Gungor and Winterton [11] suppressed the nucleate boiling contribution term and replaced it by a simpler expression. The modified correlation was compared against other correlations and the authors realized that, apart from their own expression, only the correlation of Shah [9] gave reasonable results under most of the studied conditions.

Hybrid model

The correlation of Kandlikar [32] for horizontal and vertical in-tube evaporation is also based on the additive mechanism, but with a different approach - somewhere between the enhancement model and the superposition model -. In this case, no nucleate boiling heat transfer coefficient is calculated but a sum of the convective and boiling terms is considered:

$$\alpha_{tp} = (C + N)\alpha_{cb} \tag{3.7}$$

Here α_{cb} is also calculated from the Dittus-Boelter expression and the terms C and N are used to characterise the convective and nucleate boiling contributions, respectively. The correlation of Kandlikar contains two equations of this type, which are used to differentiate two regions at saturated boiling conditions: nucleate boiling dominant (NBD) and convective boiling dominant (CBD):

$$(\alpha_{tp})_{NBD} = \left(0.6683 Co^{-0.2} f_2(Fr_l)\right) \alpha_{cb} + \left(1058.0 Bo^{0.7} F_{fl}\right) \alpha_{cb} \qquad (3.8)$$

$$(\alpha_{tp})_{CBD} = \left(1.1360 Co^{-0.9} f_2(Fr_l)\right) \alpha_{cb} + \left(667.5 Bo^{0.7} F_{fl}\right) \alpha_{cb} \qquad (3.9)$$

In both regions, nucleate and convective heat transfer phenomena occur at the same time, but one being dominant. The transition limit between both regions was originally set at $Co = 0.65$. However, in order to avoid any discontinuity problem, Kandlikar suggested to use the intersection of both expressions as follows:

$$\alpha_{tp} = max \left[(\alpha_{tp})_{NBD}, (\alpha_{tp})_{CBD} \right] \qquad (3.10)$$

This correlation was first calculated for water, but its applicability can be extended to other fluids by means of the fluid dependent parameter F_{fl}. This parameter is found in the nucleate term of each region equation, and its value is equal to unity for water but varies depending on the refrigerant. The correlation was tested against more than 5000 data points, for fluids including water, R-11, R-12, R-13B1, R-22, R-113, R-114, R-152, nitrogen and neon in both vertical and horizontal positions. No ammonia data were compared, consequently no F_{fl} factor for this fluid was proposed by Kandlikar.

The use of the fluid parameter (F_{fl}) is similar to that of the pool boiling correction factor (F_{pb}) which is obtained by comparing the pool boiling data of a particular fluid with the Forster and Zuber pool boiling correlation - the multiplication factor giving best agreement with data is the corresponding F_{pb} for that fluid -. Thus, in order to find the fluid dependent factor of Kandlikar correlation two recommendations were made [12]: use reliable experimental data for flow boiling of that fluid and employ simple curve fitting techniques or, if no flow boiling data is available, use the pool boiling factor, F_{pb}. In fact both parameters, F_{fl} and F_{pb}, should have similar values for each particular fluid, and can be used in the Kandlikar correlation for boiling in both horizontal and vertical tubes. Furthermore, this fluid parameter must be a value between 0.5 and 5 [32]. In the present work the procedure used to find the fluid parameter for ammonia consisted in finding the lower mean prediction error (MPE) for all the database points n at different fluid parameter values as shown in Equation 2.57.

In this calculation all the experimental data detailed in Table 3.2 - except the data presented by Shah - were compared to the Kandlikar correlation, and the lower mean prediction error was found at $F_{fl} \approx 0.0$. The resulting fluid parameter value is beyond the range stated by Kandlikar. According to the correlation, a null F_{fl} value suggests that no nucleate boiling contribution is present. This is physically wrong because, as Zurcher et al. [23] comment on low mass velocity tests, at such conditions convective heat transfer plays only a partial influence while nucleate boiling plays a significant role. In fact, the unexpected value of the fluid parameter was obtained because data is overestimated by the correlation of Kandlikar. The heat transfer coefficient resulting

from the maximum value between the CBD and the NBD expressions (Equation 3.10) was larger than most of the experimental data points. Figure 3.3 displays a particular case where the overestimation of ammonia data and the fluid dependent parameter influence is shown.
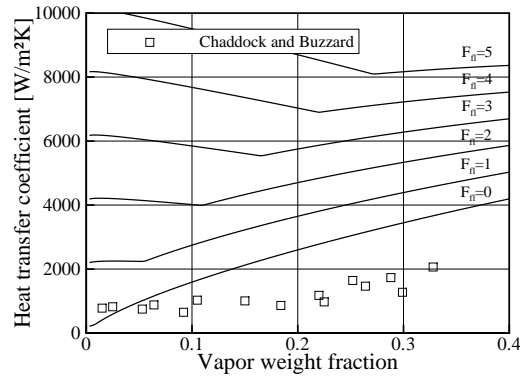

Figure 3.3: Kandlikar correlation prediction compared to Chaddock and Buzzard data [21] ($\dot{q} = 12.6\ kW/m^2$ and $G = 32\ kg/m^2 s$). Influence of the fluid parameter.

Thus, from the ammonia data predictions, it is deduced that the numerical coefficients used in Equations 3.8 and 3.9 are probably inappropriate for ammonia at those specific parameter ranges - the actual coefficients were proposed by Kandlikar [32] based on a huge vertical boiling water data set -. From the selected data, it was not possible to determine new optimal coefficients for Equations 3.8 and 3.9, nor find an appropriate value for the convective number (Co) that defines the transition limit between the two regions (nucleate and convective boiling dominant). It is concluded that the correlation of Kandlikar is not suitable for ammonia at overfeed conditions.

Asymptotic model

This model adds nucleate and convective heat transfer coefficients as follows:

$$\alpha_{tp} = (\alpha_{nb}^n + \alpha_{cb}^n)^{1/n} \qquad (3.11)$$

If n is equal to unity, the model becomes a superposition model, but if n increases significantly, the contribution of the smaller term will become irrelevant. Many au-

thors have adopted this expression in their correlations and obtained good agreement with data (e.g. Liu and Winterton [35] and Steiner and Taborek [36]).

Map oriented correlations

During in-tube saturated boiling the inner perimeter can be fully or partially wetted depending on the flow pattern type. The heat transfer coefficient correlation suggested by Kattan et al. [15] evaluates both contributions: the heat transfer occurring through the wet part of the tube (where the refrigerant liquid phase is in contact with the tube), and the heat transfer occurring through the dry part (where the refrigerant gas phase is in contact with the tube). The total flow heat transfer coefficient (α_{tp}) is obtained by adding the wet and dry coefficients (α_{wet} and α_g, respectively) according to the wet and dry parts of the tube inner perimeter:

$$\alpha_{tp} = \left(1 - \frac{\theta_{dry}}{2\pi}\right)\alpha_{wet} + \left(\frac{\theta_{dry}}{2\pi}\right)\alpha_g \quad (3.12)$$
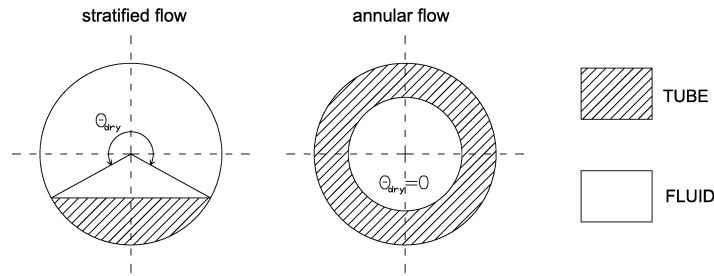
Figure 3.4: Geometrical configuration of stratified and annular two-phase flow patterns.

The angle θ_{dry} indicates the angular portion of the tube inner perimeter which is in contact with the gas phase. The value of α_g is directly calculated with the Dittus-Boelter correlation applied to the vapor phase, while α_{wet} is determined by means of the asymptotic model proposed by Steiner and Taborek [36] (Equation 3.11 using $n = 3$). In this case α_{nb} is calculated with the Cooper nucleate pool boiling heat transfer coefficient correlation [34], and α_{cb} is obtained from the liquid film thickness (δ) instead of the tube diameter:

$$\alpha_{nb} = 55 p_r^{0.12}(-log_{10}p_r)^{-0.55}M^{-0.5}\dot{q}^{0.67} \quad (3.13)$$

$$\alpha_{cb} = 0.0133 Re_\delta^{0.8} Pr_l^{0.4} \frac{\lambda_l}{\delta} \tag{3.14}$$

$$\delta = \frac{\pi D (1 - \epsilon_g)}{2(2\pi - \theta_{dry})} \tag{3.15}$$

This is a flow pattern dependent correlation. The angle θ_{dry} of Equation 3.12 is calculated depending on the flow pattern type. Therefore, the flow pattern type must be determined before applying the correlation itself. For this purpose Kattan et al. [13] developed a flow pattern map based on a previous work presented by Steiner and Taborek [36]. The new map includes five different patterns: stratified flow (S), stratified-wavy flow (SW), intermittent flow (I), annular flow (A) and mist flow (M). Each flow pattern type has a particular geometric model that represents the phases configuration in the tube cross section (see Figure 3.4). The map format, plotted as the mass velocity vs. the vapor weight fraction, allows easy data interpretation (e.g. the maps shown in Figure 3.5 for ammonia and R-134a).
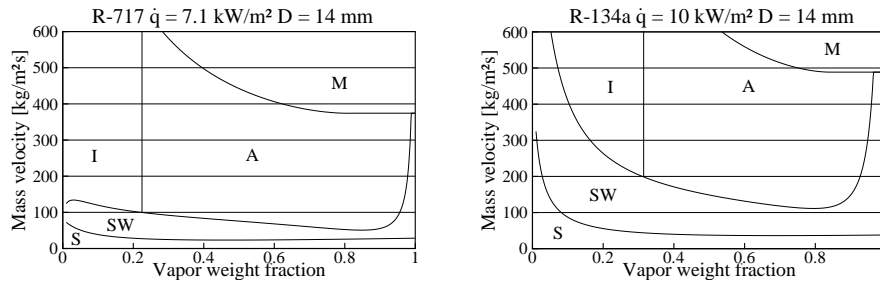
Figure 3.5: Illustrative two-phase flow pattern maps [18].

The original correlation [13–15] was tested against different refrigerants, such as R-134a, R-502, R-123, R-404A or R-402A, and a wide variety of parameter ranges. In order to extend and simplify its applicability and accuracy, several modifications of the map, as well as simplifications of the general resolution process, were carried out [16–18]. Furthermore, the correlation experimental database was enlarged in subsequent articles where new refrigerants data were included (e.g. ammonia [16]). Two main versions of the Kattan et al. correlation were reported: Thome [18] and Wojtan et al. [37, 38]. The first version employs maps like those plotted in Figure 3.5, while the second version contains, among other differences, a new subdivision of the stratified-wavy region and a modification of the dry angle calculation. These new subdividing zones, slug and slug/stratified-wavy, include some changes in the stratified region limit. However, only tests for R-22 and R-410A were reported for this latter version.

3.3.2   Correlations vs. experimental data

In the current section, the performance of several heat transfer coefficient correlations at overfeed conditions is compared. Five different correlations [9, 11, 18, 32, 38] are considered and compared directly against the selected data from four experimental databases [16, 20–23]. The thermodynamic properties of ammonia were taken from NIST refrigerant database [2].

Figure 3.6 shows the predictions obtained with the correlations of Gungor and Winterton [11] and Thome [18]. The diagonal line across the graphics represents the zone of complete agreement between numerical and experimental data, and allows to appreciate the data scatter. The heat transfer coefficient resulting from each correlation is plotted separately against different pairs of data sources: the data of Chaddock and Buzzard [21] and Zurcher et al. [16, 23] which correspond to data taken at higher heat fluxes, and the data of Shah [20] and Kelly et al. [22] which correspond to data taken at typical conditions of overfeed air-coolers.

As Figure 3.6 shows, the correlations of Gungor and Winterton and Thome have large mean prediction errors when predicting the two experimental data sets taken at low heat fluxes, 229% and 134%, respectively. On one side, the data of Shah are highly overpredicted by these correlations. In this case the experimental heat transfer coefficients are below 2000 W/m^2K, while the numerical predictions reach values over 6000 W/m^2K. This general overprediction occurs because the amount of oil circulating in the tests was large enough to significantly reduce the heat transfer coefficient. Thus, the experimental data set of Shah is not appropriate for this study. On the other side, a completely different behavior is observed in the predictions of the Kelly et al. [22] data. In this case, data are mostly underpredicted except for the few experimental tests at high mass velocities (from 47 to 61 kg/m^2s) where data tend to be overpredicted. This general underprediction of the Kelly et al. [22] data may be partly due to the high experimental uncertainties reported by Kelly et al. [22], and/or to the absence of ammonia data at low heat fluxes used in the development of these two correlations.

The experimental data sets carried out at higher heat fluxes (Chaddock and Buzzard [21] and Zurcher et al. [16, 23]) are predicted more accurately as shown in Figure 3.6 as both correlations have appropriate diagonal trends. However, the mean prediction error of the Gungor and Winterton correlation [11] is greater than that of Thome [18], 73% vs. 22%, respectively. The latter correlation has a higher accuracy, partly because it was developed using the ammonia database of Zurcher et al. [16]. This map-oriented correlation has a good adaptability to different parameter ranges and refrigerants because it includes more phenomenological aspects.

The data prediction scatter for the other three correlations studied, Shah [9], Kandlikar [32] and Wojtan et al. [38], is shown in Figure 3.7.

Table 3.4 presents the mean prediction errors of the selected correlations against
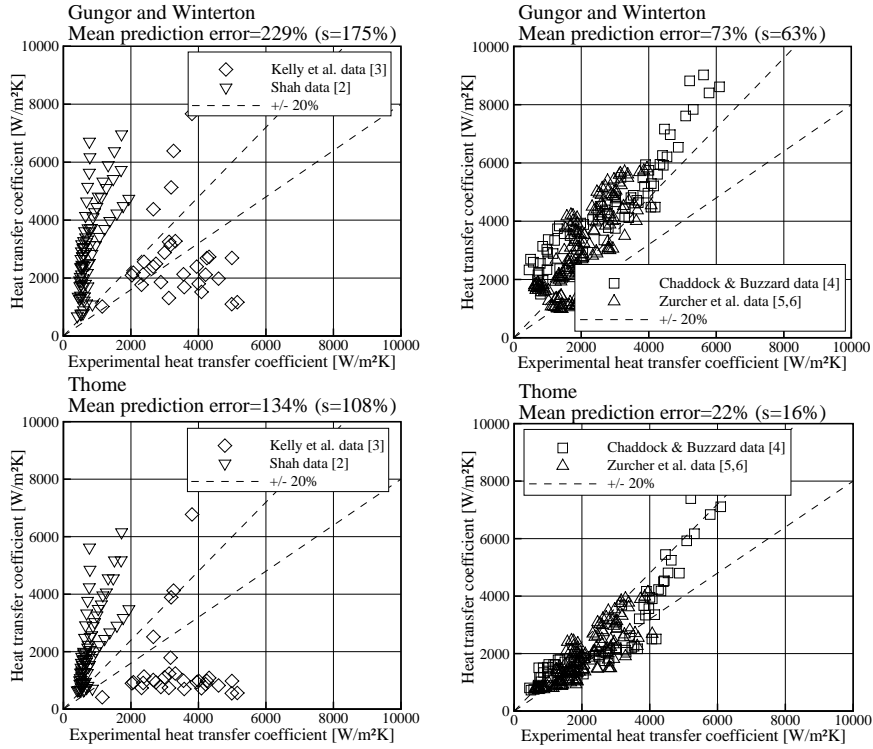
Figure 3.6: Comparison of the Thome [18] and Gungor and Winterton [11] correlations against experimental data.

the whole selected experimental data (the data of Shah [20] are not included because the excessive amount of circulating oil). The best global mean prediction error (27%) has been obtained with the correlation of Thome [18] while less accurate predictions (36%) have been observed with the correlation of Wojtan et al. [38] (as it has been developed using only two refrigerants, R-22 and R-410A). The other correlations, Shah, Gungor and Winterton and Kandlikar, show even less accurate predictions for all data, 86%, 69% and 54%, respectively. However, as regards only the data of Kelly et al., the lower mean prediction error has been obtained with the Gungor and Winterton correlation (38%). Thus, the Kelly et al. [22] data are not accurately predicted by any of the correlations studied in this paper.

Figure 3.7: Comparison of the Wojtan et al. [37, 38], Shah [9] and Kandlikar [32] correlations against experimental data.
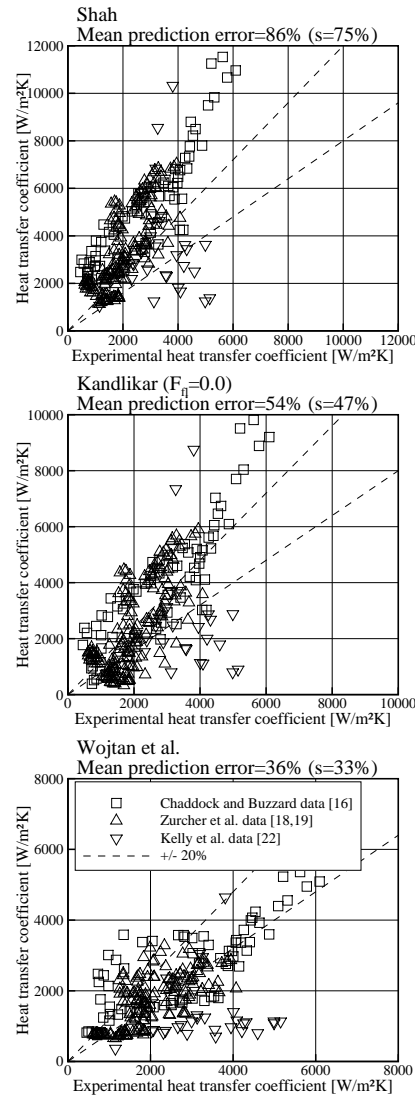
	Zurcher et al.		Chaddock & Buzzard		Kelly et al.		All data	
	$MPE(\%)$	$s(\%)$	$MPE(\%)$	$s(\%)$	$MPE(\%)$	$s(\%)$	$MPE(\%)$	$s(\%)$
Shah [9]	75	59	125	98	48	42	86	75
Gungor & Winterton [11]	62	43	97	90	38	30	69	61
Kandlikar [32]	52	37	63	66	45	34	54	47
Thome [18]	20	13	26	20	65	20	27	21
Wojtan et al. [37, 38]	28	18	43	52	57	25	36	33

Table 3.4: Mean prediction errors and standard deviations of each correlation prediction for different data sets.

3.4   Concluding remarks

The aim of this chapter was to examine the experimental data and the available correlations for ammonia evaporation inside tubes at liquid overfeed evaporation conditions.

It has been noticed that not much experimental data were available in the open literature. In spite of this limitation, some useful data could be found to pursue the objective of this study - (Kelly et al. [22], Chaddock and Buzzard [21] and Zurcher et al. [16, 23]). Among them, the Kelly et al. [22] data set exhibited large uncertainty values, but is probably the most representative for overfeed conditions. The selected experimental data sets show significant discrepancies between each other at similar test conditions.

The performance of various two-phase heat transfer coefficient correlations for ammonia evaporation inside tubes at liquid overfeed working conditions has been studied. The selected data have been compared against some of the well-known correlations which were mainly developed considering other refrigerants different than ammonia. From this comparison, none of the available correlations show complete agreement when predicting the experimental data. The earlier correlations, i.e. as Shah [9] and Gungor and Winterton [11], exhibit considerable disagreement with the data. The Kandlikar correlation has been found unsuitable for being used with ammonia at the stated conditions. Better results were found with the Thome [18] and Wojtan et al. [37, 38] correlations. In fact, the correlation of Thome shows a generally reasonable predictive capability, except for the Kelly et al. [22] data.

Based on the present study, it is suggested that further experimental works should be carried out in order to enlarge the present ammonia database at overfeed conditions. The experiments should be focused on low mass velocities, from 10 to

150 kg/m^2, low heat fluxes, from 1 to 8 kW/m^2, and low vapor weight fractions, lower than 0.6. This will require a significant effort as these specific parameter ranges are difficult to establish and measure accurately. The new data will be essential to clarify the current data sets discrepancies and to develop/modify the heat transfer coefficient correlations (preferably be of the map-oriented type) in order to have reliable predictions.

Finally, it is worth to mention that additional experimental measurements have been carried out by the EPFL (Ecole Polytechnique Fédérale de Lausanne) as part of the EFROST European proyect. The data, which included mass velocities from 50 to 70 kg/m^2s and heat fluxes between 8 and 30 kW/m^2, has led to some modifications of the Wojtan et al. [37, 38] correlation in order to improve its prediction accuracy.

Nomenclature

A	surface area, m^2
Bo	boiling number, $(Bo = \frac{\dot{q}}{Gh_{lg}})$
C	convective contribution factor
Co	convective number, $(Co = (\frac{1-x_g}{x_g})^{0.8}(\frac{\rho_g}{\rho_l})^{0.5})$
D	tube diameter, m
E	two-phase enhancement factor
F_{fl}	fluid parameter of Kandlikar correlation
F_{pb}	pool boiling factor
Fr_l	Froude number with all flow as liquid, $(Fr_l = \frac{G^2}{\rho_l^2 g D})$
f_2	function of the correlation of Kandlikar
G	mass velocity, $kg \cdot m^{-2} \cdot s^{-1}$
g	acceleration due to gravity, $m \cdot s^{-2}$
L	tube length, m
M	molecular weight, $kg \cdot kmol^{-1}$
MPE	mean prediction error, %
N	nucleate contribution factor
n	number of database points
Pr	Prandtl number, $(Pr = \frac{C_p \mu}{\lambda})$
p_r	reduced pressure
$\dot{Q}$	heat transfer, W
$\dot{q}$	heat flux, $W \cdot m^{-2}$
Re_l	Reynolds number of liquid phase, $(Re_l = \frac{G(1-x_g)D}{\mu_l})$
Re_δ	Reynolds number of liquid phase based on film thickness, $(Re_\delta = \frac{4G\delta(1-x_g)}{\mu_l(1-\epsilon_g)})$
r	tube radius, m
s	standard deviation

T	temperature, K
U_o	overall heat transfer coefficient, $W \cdot m^{-2} \cdot K^{-1}$
x_g	vapor weight fraction

Greek symbols

α	heat transfer coefficient, $W \cdot m^{-2} \cdot K^{-1}$
ΔT_{lm}	log-mean temperature difference
δ	film thickness, m
ϵ_g	gas void fraction
θ_{dry}	dry angle of tube perimeter, rad
λ	thermal conductivity, $W \cdot m^{-1} \cdot K^{-1}$
μ	dynamic viscosity, $kg \cdot m^{-1} \cdot s^{-1}$
ρ	density, $kg \cdot m^{-3}$

Subscripts

$calc$	calculated
cb	convective boiling
exp	experimental
i	inner
l	liquid
nb	nucleate boiling
o	overall, outer
sat	saturation
tp	two-phase flow
g	gas, vapor
w	wall
wet	wet part of tube

References

[1] *Ammonia data book*. International Institute of Ammonia Refrigeration, Washington DC, 1992.

[2] REFPROP v 7.0 NIST. *Thermodynamic properties of refrigerants and refrigerant mixtures database, Standard Reference Data Program*. USA, 2002.

[3] ASHRAE. *Handbook of Fundamentals.* S.I. Ed., ASHRAE Inc., Atlanta, GA, 2005.

[4] A. Pearson. Refrigeration with ammonia. *International Journal of Refrigeration*, 31(4):545–551, 2008.

[5] G. Lorentzen. Ammonia: an excellent alternative. *International Journal of Refrigeration*, 11(4):248–252, 1988.

[6] *Ammonia as a refrigerant.* International Institute of Refrigeration, Paris, France, 1999.

[7] F. Pearson. Ammonia refrigeration. Yesterday, today and for ever. In *Proceedings of the IIR Ammonia Refrigerating Systems, Renewal and Improvement Conference*, 2005.

[8] M. M. Shah. A new correlation for heat transfer during boiling flow through pipes. *ASHRAE Transactions*, 82(2):66–86, 1976.

[9] M. M. Shah. Chart correlation for saturated boiling heat transfer: equations and further study. *ASHRAE Transactions*, 88(1):185–196, 1982.

[10] K. E. Gungor and R. H. S. Winterton. A general correlation for flow boiling in tubes and annuli. *International Journal of Heat and Mass Transfer*, 29(3):351–358, 1986.

[11] K. E. Gungor and R. H. S. Winterton. Simplified general correlation for saturated flow boiling and comparisons of correlations with data. *Chemical Engineering Research and Design*, 65(2):148–156, 1987.

[12] S. G. Kandlikar. An improved correlation for predicting two-phase flow boiling heat transfer coefficient in horizontal and vertical tubes. In *Proceedings of the ASME/AIChE National Heat Transfer Conference*, volume HTD 27, 1983.

[13] N. Kattan, J. R. Thome, and D. Favrat. Flow boiling in horizontal tubes: part 1 - development of a diabatic two-phase flow pattern map. *Journal of Heat Transfer*, 120(1):140–146, 1998.

[14] N. Kattan, J. R. Thome, and D. Favrat. Flow boiling in horizontal tubes: part 2 - new heat transfer data for five refrigerants. *Journal of Heat Transfer*, 120(1):148–155, 1998.

[15] N. Kattan, J. R. Thome, and D. Favrat. Flow boiling in horizontal tubes: part 3 - development of a new heat transfer model based on flow pattern. *Journal of Heat Transfer*, 120(1):156–165, 1998.

[16] O. Zurcher, J. R. Thome, and D. Favrat. Evaporation of ammonia in a smooth horizontal tube: heat transfer measurements and predictions. *Journal of Heat Transfer*, 121(1):89–101, 1999.

[17] J. R. Thome and J. Hajal. Two-phase flow pattern map for evaporation in horizontal tubes: latest version. *Heat Transfer Engineering*, 24(6):3–10, 2003.

[18] J. R. Thome. Update on advances in flow pattern based two-phase heat transfer models. *Exp. Thermal and Fluid Science*, 29(3):341–349, 2005.

[19] C. Zamfirescu and F. Chiriac. Heat transfer measurements on ammonia forced convection boiling in vertical tubes. *Exp. Thermal and Fluid Science*, 25(7):529–534, 2002.

[20] M. M. Shah. Heat transfer, pressure drop, visual observation, test data for ammonia evaporating inside pipes. *ASHRAE Transactions*, 84(1):38–59, 1978.

[21] J. Chaddock and G. Buzzard. Film coefficients for in-tube evaporation of ammonia and R-502 with and without small percentages of mineral oil. *ASHRAE Transactions*, 92(1A):22–40, 1986.

[22] J. E. Kelly, S. J. Eckels, and D. F. Fenton. An experimental investigation of in-tube evaporation of pure ammonia in a smooth and a microfin tube, part I - heat transfer (RP-866). *HVAC and Research*, 8(3):239–256, 2002.

[23] O. Zurcher, D. Favrat, and J. R. Thome. Evaporation of refrigerants in a horizontal tube: an improved flow pattern dependent heat transfer model compared to ammonia data. *Journal of Heat Transfer*, 45(2):303–317, 2002.

[24] S. Kabelac and H. J. Buhr. Flow boiling of ammonia in a plain and a low finned horizontal tube. *International Journal of Refrigeration*, 24(1):41–50, 2001.

[25] T. Boyman, P. Aecherli, and A. Steiner. Flow boiling of ammonia in smooth horizontal tubes in the presence of immiscible oil. In *Proceedings of the International Refrigeration and Air Conditioning Conference*, 2004.

[26] J. E. Kelly, S. J. Eckels, D. F. Fenton, and Q. S. Lies. Survey of in-tube evaporation of ammonia heat transfer and pressure drop investigations. *ASHRAE Transactions*, 105(1):110–123, 1999.

[27] M. M. Ohadi, S. S. Li, R. Radermacher, and S. Dessiatoun. Critical review of available correlations for two-phase flow heat transfer of ammonia. *International Journal of Refrigeration*, 19(4):272–284, 1996.

[28] D. J. Cotter and J. F. Missenden. In search of heat transfer in ammonia air coolers. In *Proceedings of the 6th IIR Gustav Lorentzen Natural Working Fluids Conference*, 2004.

[29] J. Van Male and E.A. Cosijn. Cooler output as a function of the recirculation number of the refrigerant. In *Proceedings of the 12th International Congress of Refrigeration*, 1967.

[30] F. Chiriac and E. Sandru. Heat transfer for the vaporization of ammonia during flow through horizontal pipe systems under conditions of low vapor concentration. *International Chemical Engineering*, 18(4):692–699, 1978.

[31] R. Colin and A. Malek. Ammonia boiling in long tubes: heat transfer and charge loss in vertical and horizontal tubes. NASA Technical Translation 20313, National Aeronautics and Space Administration, 1988.

[32] S. G. Kandlikar. A general correlation for saturated two-phase flow boiling heat transfer inside horizontal and vertical tubes. *Journal of Heat Transfer*, 112(1):219–228, 1990.

[33] J. C. Chen. A correlation for boiling heat transfer to saturated fluids in vertical flow. *Ind. and Eng. Chem. Process Design and Development*, 5(3):322–339, 1966.

[34] M. G. Cooper. Saturation nucleate pool boiling - a simple correlation. *Institution of Chemical Engineers Symposium Series*, 86:785–793, 1984.

[35] Z. Liu and R. H. S. Winterton. A general correlation for saturated and subcooled flow boiling in tubes and annuli, based on a nucleate pool boiling equation. *International Journal of Heat and Mass Transfer*, 34(11):2759–2766, 1991.

[36] D. Steiner and J. Taborek. Flow boiling heat transfer in vertical tubes correlated by an asymptotic model. *Heat Transfer Engineering*, 13(2):43–69, 1992.

[37] L. Wojtan, T. Ursenbacher, and J.R. Thome. Investigation of flow boiling in horizontal tubes: part I - a new diabatic two-phase flow pattern map. *International Journal of Heat and Mass Transfer*, 48(14):2955–2969, 2005.

[38] L. Wojtan, T. Ursenbacher, and J.R. Thome. Investigation of flow boiling in horizontal tubes: part II - development of a new heat transfer model for stratified-wavy, dryout and mist flow regimes. *International Journal of Heat and Mass Transfer*, 48(14):2970–2985, 2005.

Chapter 4

Numerical Simulation of Capillary Tubes. Application to Domestic Refrigeration with R-600a

ABSTRACT

In the present chapter the implementation and validation of a numerical procedure to simulate the thermal and fluid-dynamic phenomena inside capillary tubes is carried out. The algorithm allows the prediction of both critical and non-critical flow conditions.

The fluid flow behavior is predicted with a quasi-homogeneous two-phase flow model where the governing equations (continuity, momentum, energy and entropy) are integrated over the discretized fluid flow domain and solved by means of a numerical implicit step-by-step scheme. The numerical model considers four different transitional regions: subcooled liquid region, metastable liquid region, metastable two-phase region and equilibrium two-phase region. The thermal behavior of the capillary tube solid parts is predicted from the energy equation which is integrated over the discretized solid domain. Its resolution is achieved with a Gauss-Seidel or a TDMA scheme. The capillary tube fluid and solid parts are coupled and solved iteratively in a segregated manner.

In this chapter, the general characteristics of capillary tubes are briefly described together with their application on domestic refrigeration. The numerical model is described and its most significant aspects are detailed. The simulation results are compared against different experimental data sets including adiabatic and non-adiabatic conditions. Finally, an extensive parametric study on capillary tubes used in household refrigerators working with R-600a (isobutane) is carried out.

4.1   Introduction

The present concern in the environment preservation is bringing new challenges to the design of refrigeration systems. The research community efforts are focused on improving the energy efficiency of refrigerating units (in order to reduce the power consumption) and on replacing the harmful artificial working fluids to environmentally friendly refrigerants.

The natural refrigerant R-600a (isobutane) is considered a substitute for the synthetic refrigerants used in domestic refrigerators. It has zero ozone depletion potential (ODP) and insignificant global warming potential (GWP). This refrigerant has been widely used in the past until 1940 when the newly developed artificial refrigerants were rapidly introduced in the market. However, nowadays isobutane is again widely used in domestic refrigerators and freezers, especially in Europe. It has good energy efficiency but special care has to be taken with its flammability. Its particular thermodynamic characteristics imply new and/or adapted system designs.
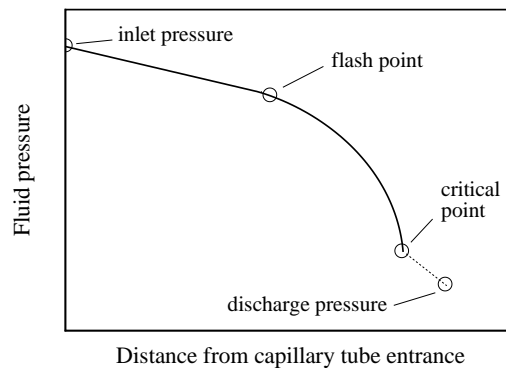

Figure 4.1: Pressure distribution along a capillary tube.

Single-stage vapor compression refrigerating systems are commonly used in small capacity applications like domestic refrigerators. They are basically made up of four elements: a compressor, a condenser, an expansion device and an evaporator. Among all the expansion devices available, the capillary tube is widely used in household refrigerators. It consists in a fixed length tube, with a relatively small diameter (about 1 mm), placed between the outlet of the condenser and the inlet of the evaporator.

Inside the capillary tube the refrigerant pressure is drastically reduced and its state changes from liquid to a liquid-vapor mixture due to the flashing phenomenon. The flow of refrigerant is metered from the high pressure side to the low pressure

side of the refrigerating system according to load demand. The capillary tube does not operate efficiently over a wide range of conditions compared to a thermostatic expansion valve. However, it is reliable, less expensive and performs nearly well. It also allows low compressor starting torque as pressures equalize when the system is off. The appropriate design of this device is crucial for the global refrigerating system performance.

The flow rate of the refrigerant through a capillary tube increases as the discharge pressure decreases but only up to a critical value, below which the flow does not change (choked flow). Capillary tubes normally work under such critical conditions. The typical pressure evolution profile of the evaporating flow through capillary tubes is depicted in Figure 4.1. Three main regions are distinguished. Firstly, the single-phase region which lies between the capillary tube inlet and saturation pressures (down to the flash point). Secondly, the two-phase region where the refrigerant pressure rapidly drops. And finally, a shock wave located at the outlet of the capillary tube if critical conditions are met (i.e. the capillary tube discharge pressure is lower than the critical discharge pressure). For more information about capillary tubes see [1].
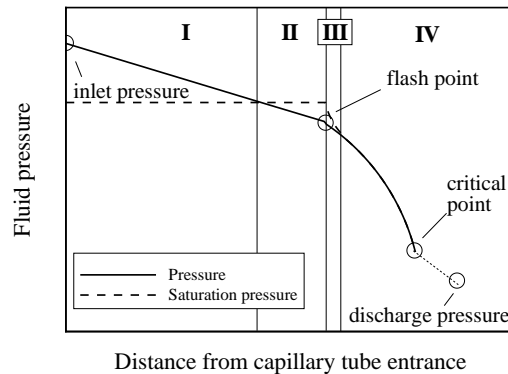

Figure 4.2: Phenomena occurring along a capillary tube: I) subcooled liquid single-phase, II) metastable liquid single-phase, III) metastable liquid-vapor two-phase, and IV) thermodynamic equilibrium liquid-vapor two-phase.

During the last decades capillary tubes have been experimentally and numerically studied by different authors as shown in the extensive review presented by Khan et al. [2]. In several works (e.g. [3, 4]) it has been observed that the actual location of the flash point is not at the saturation condition but somewhere downstream from it. Consequently metastable equilibrium occurs between the liquid and the liquid-

vapor flows. This phenomenon is represented in two regions: a metastable liquid phase region (pure liquid between the saturation pressure and the flash point) and a metastable liquid-vapor two-phase region (between the flash point and the liquid-vapor thermodynamic equilibrium). The metastable condition is detailed in Figure 4.2 where both the fluid pressure and the saturation pressure profiles along the capillary tube are plotted (the saturation pressure is the pressure calculated from the fluid temperature).

In this chapter the numerical model to simulate capillary tubes reported by Escanes et al. [5] and upgraded by García-Valladares [6, 7] has been implemented. The numerical model is described and its most significant aspects are detailed. The simulation results are compared against different experimental data sets including adiabatic and non-adiabatic conditions. The chapter ends with an extensive parametric study on capillary tubes working with R-600a and considering household refrigerating systems.

4.2   Numerical model

In this section the capillary tube numerical model is detailed. The model is based on the two-phase flow model presented in Chapter 2 but including important modifications that allow to simulate the particular phenomena present in capillary tubes. The following aspects are described: i) the flow mathematical formulation; ii) the two-phase flow model details and discretization; iii) the empirical correlations used; iv) the different regions studied during the expansion process; and v) the capillary tube numerical resolution procedure.

4.2.1   Two-phase flow mathematical formulation

The formulation of the two-phase flow inside tubes is based on the governing equations (continuity, momentum, and energy) which are described in Section 2.2. However, for the capillary tube simulation, special attention should be paid to the entropy generation equation:

$$\frac{\partial}{\partial t} \int_v s\rho dV + \int_s s\rho \vec{v} \cdot \vec{n} dS + \int_s \frac{\vec{q} \cdot \vec{n}}{T} dS = \int_v \dot{s}_{gen} dV \qquad (4.1)$$

This equation is accomplished along the whole capillary tube at non-critical conditions, but it is not anymore valid when critical conditions are reached (from the critical point as shown in Figure 4.1).

4.2.2 Numerical simulation of the in-tube two-phase flow and the solid elements

The numerical simulation model of the thermal and fluid-dynamic behavior of two-phase flow inside tubes is obtained from the integration of the fluid governing equations along the flow domain, which is split into a number of finite control volumes as is shown in Figure 2.1. Considering a steady-state quasi-homogeneous fully-implicit one-dimensional model, the discretized governing equations (continuity, momentum, energy and entropy generation) show the following form:

$$\dot{m}_i - \dot{m}_{i-1} = 0 \tag{4.2}$$

$$\dot{m}_i v_i - \dot{m}_{i-1} v_{i-1} = (p_{i-1} - p_i)S - \bar{\tau}_i \pi D \Delta z_i - \bar{\rho}_i g sin(\theta) S \Delta z_i \tag{4.3}$$

$$\dot{m}_i(h_i + e_{c,i} + e_{p,i}) - \dot{m}_{i-1}(h_{i-1} + e_{c,i-1} + e_{p,i-1}) = \bar{\dot{q}}_i \pi D \Delta z_i \tag{4.4}$$

$$-\dot{m}_{i-1}s_{i-1} + \dot{m}_i s_i - \frac{\bar{\dot{q}}}{T_{wall}}\pi D \Delta z_i = \dot{s}_{gen,i} \tag{4.5}$$

This formulation requires the use of empirical correlations to evaluate the void fraction, the shear stress and the heat transfer coefficient. The most important details of this model are presented in Chapter 2. The resolution is carried out on the basis of a step-by-step numerical scheme where the governing equations are rearranged and solved for the control volume downstream node. Thus, from the inlet flow conditions (i.e. $\dot{m}_1, p_1, h_1$) each control volume outlet state is calculated sequentially. The tube wall temperature map acts as the boundary condition for the whole internal flow.

The energy balance over the solid part of the tube is also considered. The tube is discretized in a way, that for each fluid control volume, there is a corresponding tube temperature (see Figure 2.1). The balance takes into account the conduction heat transfer along the tube itself together with the heat transferred to/from the external environment and the heat exchanged with the internal fluid. The discretized energy equation applied at each solid control volume is expressed as follows:

$$-\lambda_{i_-}\frac{T_i - T_{i-1}}{z_i - z_{i-1}}S + \lambda_{i_+}\frac{T_{i+1} - T_i}{z_{i+1} - z_i}S + \bar{\dot{q}}_{ext,i}\pi D_{ext}\Delta z_i - \bar{\dot{q}}_i \pi D \Delta z_i = 0 \tag{4.6}$$

The process of solving in a segregated way the inner fluid, the solid tube and the external condition (if necessary), is carried out iteratively until a converged solution is obtained. The solution is given when all the variables (mass flow rate, pressure, enthalpy, tube temperatures and external variables) agree with the convergence criteria $(|(\phi^* - \phi)/\phi| \le \xi)$.

4.2.3   Empirical coefficients

Empirical correlations to calculate the friction factor, the heat transfer coefficient and the two-phase flow gas void fraction are needed for the numerical model closure. In the following paragraphs a brief description of the correlations used in the capillary tube model is given.

Friction factor and shear stress

For single-phase flow the friction factor is calculated from the correlation of Churchill [8] which depends on the Reynolds number and the tube roughness. For two-phase flow, the shear stress (τ_{tp}) is predicted from the single-phase shear stress and a two-phase flow multiplier ($\tau_{tp} = \tau\phi^2$). The two-phase flow multiplier is calculated by means of the expression proposed by Friedel [9].

Heat transfer coefficient

The heat transfer coefficient for in-tube single-phase flow is calculated with the correlation proposed by Gnielinski [10] which was tested for a wide range of experimental conditions (the correlation of McAdams [11] is used for annular ducts). The use of two-phase flow heat transfer correlations has not been considered because heat transfer at two-phase flow conditions does not appear in any case studied throughout this chapter.

Void fraction

The void fraction is usually calculated from the slip ratio approach (see Equation 2.54). It consists in assuming that the liquid and vapor phases are separated into two streams that flow through the tube with different velocities, v_g and v_l, the ratio of which is given by the split ratio (v_g/v_l). In the present chapter all of the results have been obtained from this approach and the split ratio has been estimated with the expression reported by Premoli et al. [12].

4.2.4   Metastable region

The state of the refrigerant flow through the capillary tube changes from single- to two-phase flow. However, two additional metastable states are observed during the transitional zone: metastable liquid and metastable two-phase. In order to consider these two additional regions the approach proposed by García-Valladares [13] has been implemented. The main aspects of the four regions (single-phase, metastable liquid, metastable two-phase, and two-phase in thermodynamic equilibrium) are plotted in

Figure 4.2 and detailed in the following paragraphs.

Single-phase

This region corresponds to the subcooled liquid region and is defined by $p \geq p_{sat}$ and $x_g = 0$. The heat transfer coefficient and the friction factor are predicted from the appropriate correlations for single-phase flow (see Section 4.2.3). The fluid pressure, enthalpy and temperature are obtained from the discretized equations presented in Section 4.2.2.

Metastable liquid

This region begins when the pressure drops down to the saturated condition and ends at the onset of vaporization ($p_{sat} > p \geq p_v$ and $x_g = 0$). The pressure of vaporization (p_v) is estimated with the correlation proposed by Chen et al. [14]:

$$\frac{(p_{sat} - p_v)\sqrt{KT_{sat}}}{\sigma^{3/2}} = 0.679 \left(\frac{\rho_l}{\rho_l - \rho_g}\right) Re^{0.914} \left(\frac{\Delta T_{sc}}{T_{cr}}\right)^{-0.208} \left(\frac{D}{D'}\right)^{-3.18} \tag{4.7}$$

Where D' is a reference length given by $D' = 10^4 \sqrt{KT_{sat}/\sigma}$. In this region the properties are calculated from the liquid saturation conditions but at the actual fluid pressure. The fluid temperature is calculated from the following equation:

$$dh = c_p dT + \left(\frac{\partial h}{\partial p}\right)_T dp \tag{4.8}$$

The friction factor and the heat transfer coefficient are evaluated with correlations for single-phase flow.

Metastable two-phase

This region is defined when $p_v > p$, $0 < x_g \leq x_{g,equi}$ and $0 \leq y \leq 1$. Both the heat transfer coefficient and the friction factor are estimated from two-phase flow correlations. Feburie et al. [15] defined the variable y as the mass ratio of total saturated phase to total phase ($y = (m_l + m_g)/(m_g + m_l + m_m)$) where the subscript m corresponds to the superheated liquid. The parameter y is calculated from the following correlation:

$$\frac{dy}{dz} = 0.02 \frac{P}{S}(1 - y)\left(\frac{p_{sat} - p}{p_{cr} - p_{sat}}\right)^{0.25} \tag{4.9}$$

The mean enthalpy is obtained from the discretized equations of Section 4.2.2. The gas weight fraction is deduced from the following equation:

$$h = (1 - y)h_m + (y - x_g)h_l + x_g h_g \qquad (4.10)$$

Thus, the average temperature for this region is obtained from both the gas weight fraction and the temperature at thermodynamic equilibrium, $x_{g,equi}$ and T_{equi}, respectively:

$$T = T_{equi} - \left(\frac{x_g - x_{g,equi}}{x_{g,equi}} \right)(T_m - T_{equi}) \qquad (4.11)$$

Two-phase in thermodynamic equilibrium

This region is defined when $p_v > p$ and $x_{g,equi} < x_g < 1$. Both the heat transfer coefficient and the friction factor are calculated from appropriate correlations for two-phase flow.

4.2.5   Capillary tube numerical resolution

The algorithm to simulate the capillary tube by means of the two-phase flow model is carried out in two steps clearly defined: i) calculate the capillary tube critical limit (e.g. critical conditions), and ii) determine if the capillary tube is working at critical or non-critical conditions in order to perform the corresponding numerical simulation. For the analysis presented herein the boundary conditions considered are the fluid inlet and discharge pressures, p_{in}^{bc} and p_{out}^{bc}, respectively.
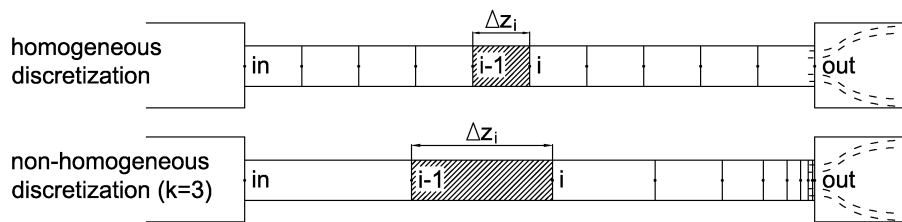

Figure 4.3: Capillary tube discretization.

Critical conditions

The mass flow rate inside a capillary tube increases as the evaporating temperature decreases (lower discharge pressure) but only up to a critical limit from which the mass flow rate remains constant. This critical limit is used to determine if the capillary tube is working at critical or non-critical conditions (the critical condition occurs when the entropy generation equation is not anymore accomplished, $\dot{s}_{gen,i} < 0$, see Equation 4.5). In the two-phase flow numerical model the critical limit is reached when the entropy generation equation is accomplished along the whole tube except at the capillary tube outlet position (the downstream face of the last control volume). It can be alternatively calculated when dp/dz approaches to infinity at the capillary tube end. The latter criterion can also be expressed by means of the following equation:

$$\frac{dz}{dp} \leq \xi \tag{4.12}$$

The critical condition is defined from the critical limit values, namely the critical mass flow rate and the critical outlet pressure, $\dot{m}_{cr}$ and p_{cr}, respectively. The algorithm scheme to calculate the critical limit is depicted in Figure 4.4 (step 1). In order to appropriately apply the condition of Equation 4.12 it is convenient to use a non-uniform grid for the fluid domain discretization due to the high pressure gradients produced at the end of the capillary tube. Thus, according to the nomenclature of Figure 4.3 the mesh is generated from the following expression:

$$\Delta z_i = \frac{L}{tanh(k)} * \left(tanh\left(\frac{k(i-1)}{n} \right) - tanh\left(\frac{k(i-2)}{n} \right) \right) \tag{4.13}$$

Where n is the number of control volumes and k is the concentration factor (for all the cases simulated in this work $k = 3$). The consequence of using this mesh is that the control volume size decreases progressively between the inlet and the outlet fluid domain cross sections. The control volume degree of shrinkage depends on the concentration factor and on its relative distance to the domain inlet cross section.

Critical and non-critical flow resolution

The flow is critical when the critical pressure is higher than the actual discharge pressure ($p_{cr} > p_{out}^{bc}$) and non-critical in the opposite case ($p_{cr} \leq p_{out}^{bc}$). If the flow is non-critical new iterations are carried out in order to find the refrigerant thermal and fluid-dynamic behavior (the corresponding mass flow rate is obtained when the discharge pressure is equal to the calculated capillary tube outlet pressure). However, if the flow is critical, an additional control volume is considered at the capillary tube outlet end. The inlet section of this control volume corresponds to the capillary
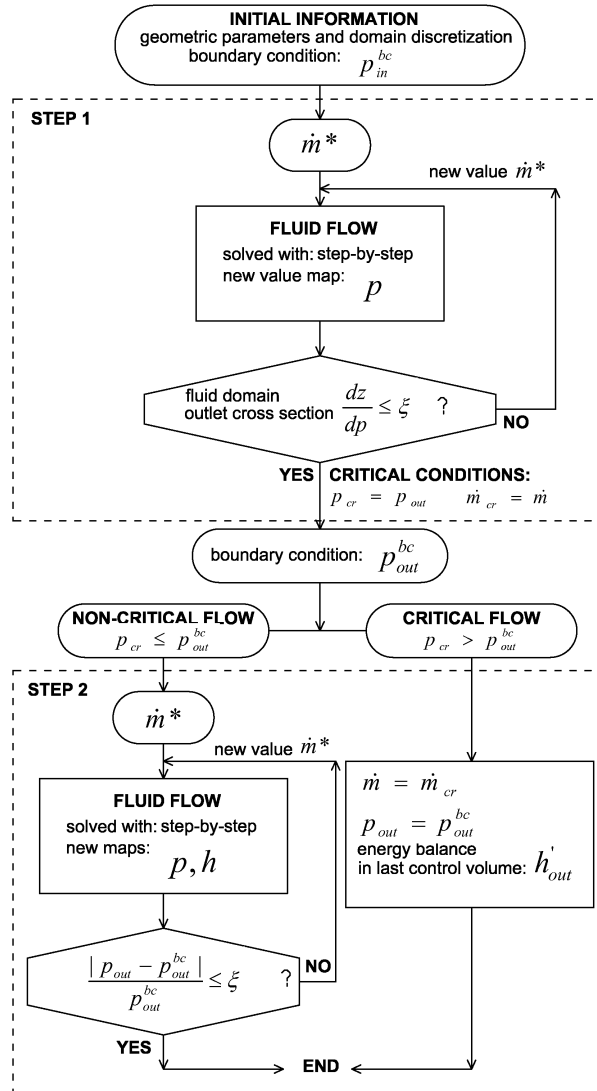
Figure 4.4: Capillary tube resolution scheme for critical and non-critical conditions.

tube inner diameter while the outlet section corresponds to the discharge tube inner diameter. The energy equation is applied at this control volume (considering constant pressure and neglecting both the heat transfer and the transient terms) in order to calculate the new capillary tube outlet enthalpy (h'_{out}):

$$h'_{out} = h_{out} - \frac{\left(\frac{\dot{m}_{cr}}{\rho'_{out} S_{dis}}\right)^2}{2} + \frac{\left(\frac{\dot{m}_{cr}}{\rho_{out} S_{out}}\right)^2}{2} \tag{4.14}$$

The previous equation is solved iteratively because the density (ρ'_{out}) depends on the outlet state (p^{bc}_{out} and h'_{out}). The algorithm scheme to simulate the capillary tube at critical or non-critical conditions is depicted in Figure 4.4 (step 2).

4.3 Experimental vs. numerical results

The predictions of the implemented numerical model are compared against experimental data found in the open literature for both adiabatic and non-adiabatic conditions. The effects due to the metastable phenomenon are also considered. In all the cases good agreement has been obtained therefore the model validation has been successful.

4.3.1 Adiabatic capillary tube

The pressure evolution inside capillary tubes has been experimentally studied by many authors. In this section the results obtained from the works done by Li et al. [16] and Mikol et al. [3] are compared against the predictions obtained with the capillary tube model. The description of the selected experimental cases is presented in Table 4.1. The measurements were reported for R-12 and R-22 and include different geometric and operational conditions.

case	source	fluid	L_{cap} (m)	D (mm)	$\dot{m}$ (kg/h)	p_{in} (bar)	p_{out} (bar)	T_{in} (°C)	ϵ (m)
a	Li et al. [16]	R-12	1.5	0.66	4.07	9.67	3.33	31.4	1.5e-6
b	Li et al. [16]	R-12	1.5	0.66	3.04	7.17	3.25	23.4	1.5e-6
c	Li et al. [16]	R-12	1.5	1.17	15.66	8.85	2.45	30.0	1.5e-6
d	Li et al. [16]	R-12	1.5	1.17	12.25	8.40	2.73	33.8	1.5e-6
e	Mikol et al. [3]	R-12	1.83	1.41	21.23	8.58	3.72	32.8	5.4e-7
f	Mikol et al. [3]	R-22	1.83	1.41	30.70	16.41	4.00	40.7	5.4e-7

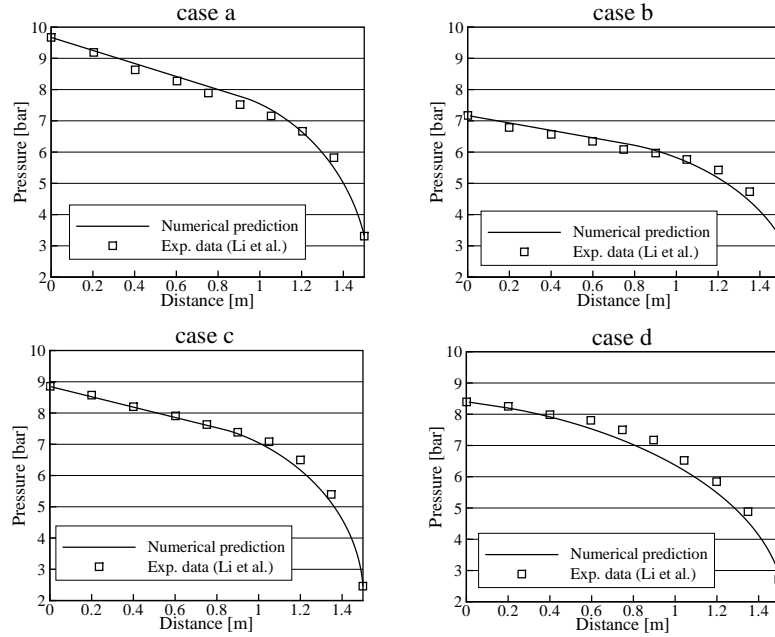**Table 4.1:** Experimental cases of adiabatic capillary tubes.

Figure 4.5: Comparison of Li et al. [16] experimental data vs. the present numerical model.
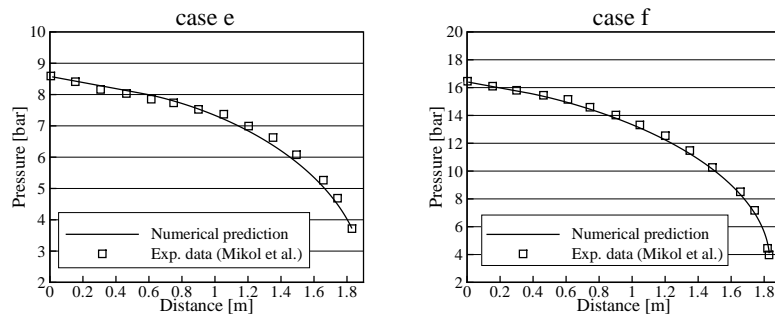

Figure 4.6: Comparison of Mikol et al. [3] experimental data vs. the present numerical model.

The numerical simulations have been carried out considering adiabatic conditions and using the empirical correlations mentioned in Section 4.2.3. The results are shown in Figures 4.5 and 4.6 where the experimental pressure measurements along the capillary tubes are compared against the numerical pressure profile. In all the cases the pressure behavior is as expected: a linear pressure decrease before the starting of vaporization (single-phase flow) followed by a steeper pressure decrease (two-phase flow). It is observed that the pressure trends are correctly predicted by the numerical model.

The numerical predictions are accurate enough as the mean prediction error (Equation 2.57) between the pressure measurements and the predictions is 2.0% and the corresponding standard deviation is lower than 2.0%. Furthermore, the experimental mass flow rate reported for each case has also been accurately predicted with a mean prediction error and standard deviation of 2.9% and 1.95%, respectively. The scatter between experimental and numerical data is plotted in Figure 4.7.
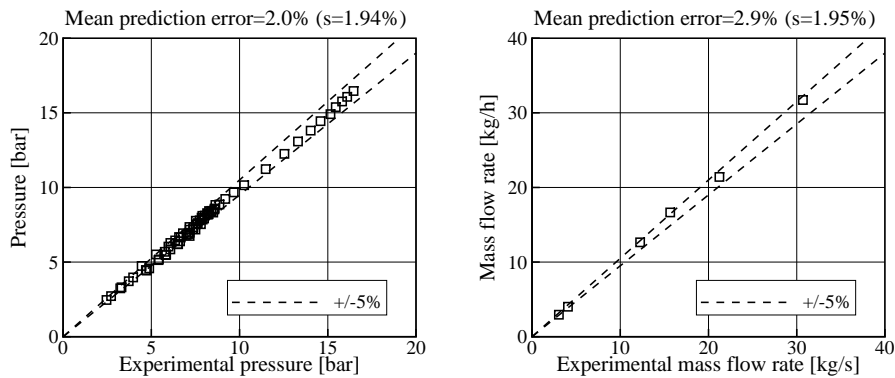

Figure 4.7: Error scatter between numerical and experimental results for adiabatic capillary tubes: pressure (left) and mass flow rate (right).

Metastable phenomenon

The metastable effect is studied in Figures 4.8 and 4.9 which correspond to cases *a* and *b* of Table 4.1, respectively. The experimental measurements of the fluid pressure are plotted along with the saturation pressure (deduced from the fluid temperature measurements) and compared against the numerical predictions. It is observed that the model accurately predicts both pressure profiles. In the same Figures, the refrigerant temperature profile is numerically predicted considering two different situations (with and without taking into account the metastable phenomenon).
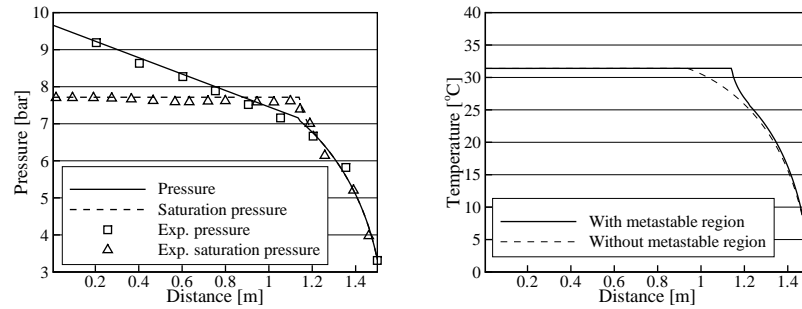
Figure 4.8: Numerical results vs. experimental data from Li et al. [16] (case a).
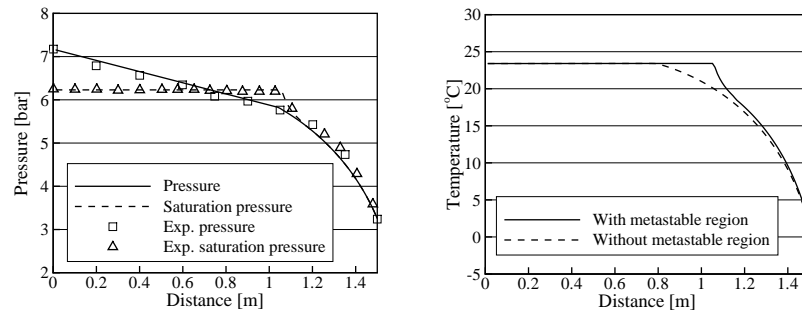

Figure 4.9: Numerical results vs. experimental data from Li et al. [16] (case b).

The metastable effects are clearly noticed. Firstly, the pressure linear decrease is extended beyond the saturation condition (e.i. beyond the point where the fluid and the saturation pressures meet for the first time). The global flow resistance through the capillary tube is reduced when the metastable region is taken into account due to the later beginning of the two-phase condition (the pressure loss gradient is higher at two-phase condition). Secondly, the refrigerant temperature profile changes significantly if the metastable region is taken into account or not. In fact, the actual fluid temperature (when the metastable region is considered) is higher than the temperature at thermodynamic equilibrium at the metastable region.

4.3.2 Non-adiabatic capillary tube

In some refrigerating systems the capillary tube usually forms a counter flow heat exchanger with the compressor suction line. Such configuration prevents liquid phase entering into the compressor. It also allows to increase the system mass flow rate and to reduce the refrigerant gas weight fraction at the evaporator inlet (higher evaporator capacity) with only a slight increase in the compressor power consumption. The global system thermodynamic efficiency is improved when the cooling capacity increase exceeds the compressor power increase.
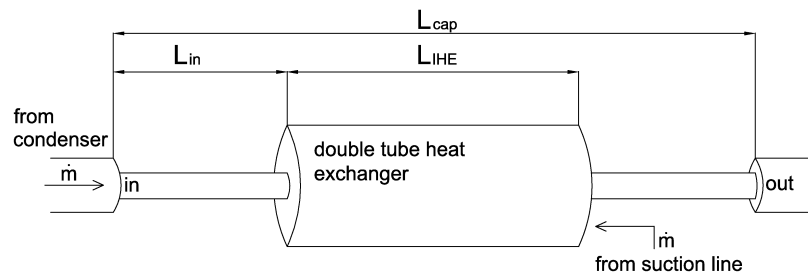

Figure 4.10: Diagram of capillary tube with double tube heat exchanger.

Melo et al. [17] reported a complete experimental data set on capillary tubes working with R-600a. The test section included a double tube counter flow heat exchanger as shown in Figure 4.10. The experimental data consist in 30 runs obtained for different geometric and operational conditions (see Table 4.2).

The numerical model has been adapted to adequately reproduce the experimental data reported by Melo et al. [17]. Three concatenated tube portions have been considered to simulate the whole capillary tube system: an adiabatic inlet duct, a double tube counter flow heat exchanger with insulation, and an adiabatic outlet duct. The empirical correlations used for the simulations are reported in Section 4.2.3.

Basically, two parameters have been predicted (the annular fluid flow outlet temperature and the refrigerant mass flow rate) and compared against the experimental data. The results are presented in Figure 4.11 where the prediction scatter is shown. The numerical model has an acceptable accuracy as the refrigerant mass flow rate and the annular fluid flow outlet temperature have mean prediction errors lower than 6% and 11%, and standard deviations of 4.8% and 8.5%, respectively. The discrepancies are more significant for the temperature as it highly depends on the annular heat transfer correlation selected.

Geometrical parameters	
Length of the first tube section (L_{in})	0.2/0.6 m
Length of the heat exchanger (L_{IHE})	1.0/2.2 m
Tube total length (L_{cap})	3.0/4.0 m
Capillary tube inner (outlet) diameter	0.553(1.801)/0.766(1.950) mm
Annular tube inner (outlet) diameter	6.30(7.94)/7.86(9.84) mm
Operational parameters	
Capillary tube inlet pressure	5.01 to 6.53 bar
Capillary tube outlet pressure	0.58 to 0.90 bar
Subcooling degree	5 to 10.2 ^oC
Annular flow inlet temperature	-20.7 to -11.9 ^oC

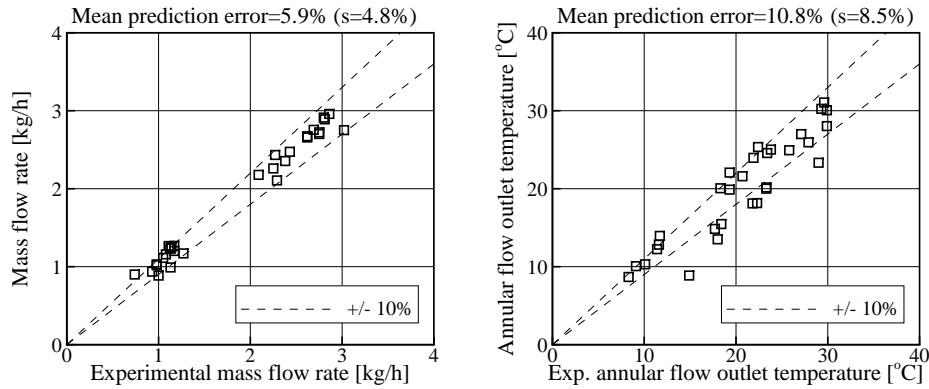**Table 4.2:** Experimental data conditions (Melo et al. [17]).

Figure 4.11: Error scatter between numerical and experimental results for non-adiabatic capillary tubes: mass flow rate (left) and annular flow outlet temperature (right).

4.4 Parametric study on capillary tubes

In this section a parametric study on non-adiabatic capillary tubes working with R-600a is carried out. The results have been achieved by means of the numerical model presented in this chapter and considering capillary tube geometric and operational conditions similar to those found in common household refrigerators.

The capillary tube configuration is that of Figure 4.10 which includes a double

tube heat exchanger. The influence of several parameters (double tube heat exchanger length, capillary tube length, capillary tube inner diameter, annular duct inner diameter, tube roughness, subcooling degree, superheating degree and discharge pressure) on both the refrigerant mass flow rate and the annular flow outlet temperature has been studied (in a vapor compression refrigerating cycle the annular flow outlet temperature corresponds to the compressor inlet temperature). The simulated ranges and the reference case conditions are presented in Table 4.3.

Geometric parameters	
Capillary tube inlet length (L_{in})	**0.0** m
Heat exchanger length (L_{IHE})	0.0 to 2.0 (**1.0**) m
Capillary tube length (L_{cap})	1.25 to 3.25 (**2.5**) m
System inner diameter	**45** mm
Capillary tube inner diameter	7 to 9 (**8**) mm
Capillary tube outlet diameter	**2** mm
Annular duct inner diameter	52 to 76 (**64**) mm
Tube roughness (10^{-7})	1 to 65 (**15**) m
Operational conditions	
Refrigerant	**isobutane**
Subcooling degree	5 to 9 (**7**) ^{o}C
Superheating degree	3 to 7 (**5**) ^{o}C
Condensing temperature	**40** ^{o}C
Evaporation temperature	-27 to -19 (**-23**) ^{o}C

Table 4.3: Capillary tube parametric study: geometric and operational parameters (reference conditions in bold).

For these studies, the capillary tube numerical model considers two concatenated regions: a double tube counter flow heat exchanger with insulation, and an adiabatic outlet tube. The empirical correlations are taken from Section 4.2.3. The boundary conditions considered are the inlet and discharge pressures. Moreover, the annular fluid mass flow rate must be equal to that of the capillary tube (in order to simulate a refrigerating cycle). The latter condition needs additional iterations of the whole capillary tube.

Figure 4.12 shows the detailed profiles of the fluid temperature and pressure along the capillary tube for the reference case. According to the flow direction, three different trends are distinguished in the inner fluid temperature profile: i) the refrigerant temperature decreases due to the heat transferred to the annular fluid; ii) the temperature change is imperceptible due to single-phase adiabatic conditions; and iii) two-phase conditions are attained and the subsequent abrupt pression decrease causes the steep temperature decrease. In regards to the pressure profile two different
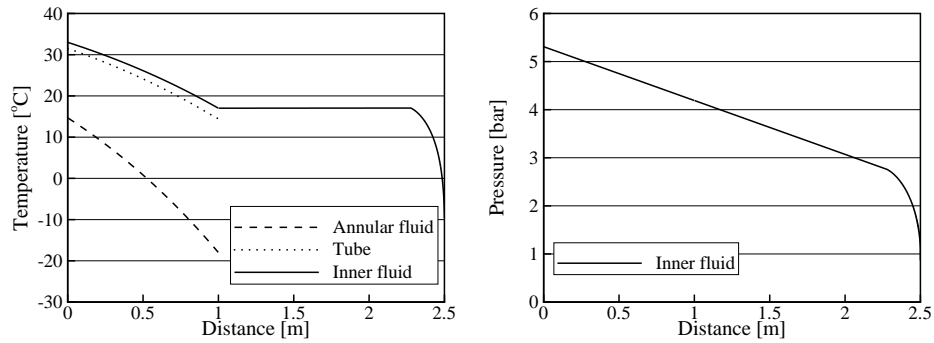
Figure 4.12: Refrigerant temperature and pressure profiles for the reference case.

trends are clearly differentiated: i) linear decrease (single-phase flow); and ii) abrupt decrease (two-phase flow). It is noticed that the two-phase region is reached near the capillary tube end (i.e. at about 2.28 m from the entrance).

Figure 4.13: Influence of the double tube heat exchanger length: (a) refrigerant mass flow rate, (b) compressor inlet temperature and (c) refrigerating cycle parameters.

The influence of the double tube heat exchanger length is shown in Figure 4.13 (a and b) where two parameters are studied (the mass flow rate and the annular fluid outlet temperature). The refrigerant mass flow rate increases as the heat exchanger length increases because the beginning of the two-phase flow (where the pressure starts to fall abruptly) occurs later as the refrigerant cools down, and consequently

the global pressure drop through the capillary tube is reduced. It is observed that both the mass flow rate and the annular fluid outlet temperature have asymptotic behaviors. This is mainly due to the double tube counter flow heat exchanger nature (the heat transfer has an asymptotic trend as the length is increased).

The influence of the double tube heat exchanger length on a theoretical refrigerating cycle is also studied in Figure 4.13 (c) where three parameters are plotted: i) the cooling capacity of the system (calculated from the mass flow rate and the evaporator enthalpy change); ii) the compressor work (calculated from a theoretical expression $w_s = RT_{comp}\frac{\gamma}{\gamma-1}(\Pi^{(\gamma-1)/\gamma} - 1)$); and iii) the system coefficient of performance which is deduced from the cooling capacity and compression work. In this case the cooling capacity increases (due to the higher mass flow rate and the lower evaporator inlet gas weight fraction) as well as the compressor work (due to the higher mass flow rate and the lower inlet fluid density). The cooling capacity increases more rapidly than the compressor work then the COP also increases. All the parameters present an asymptotic behavior as they are closely related to the mass flow rate profile.
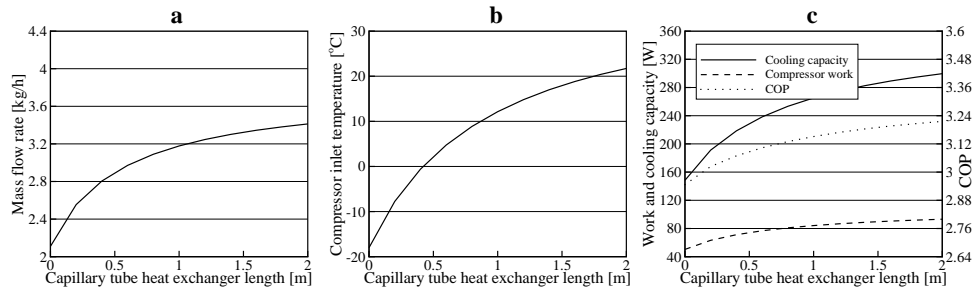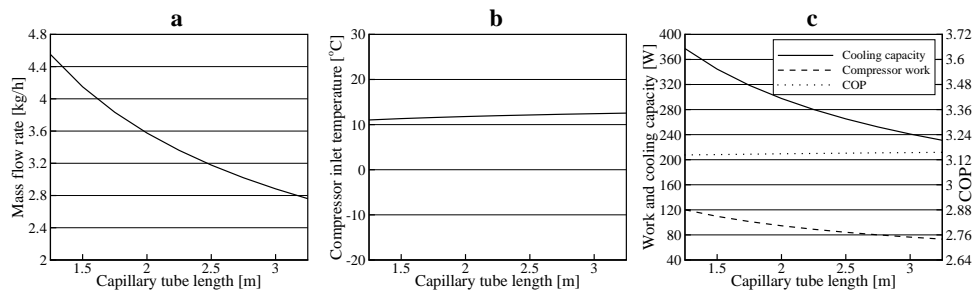

Figure 4.14: Influence of capillary tube length: (a) refrigerant mass flow rate, (b) compressor inlet temperature and (c) refrigerating cycle parameters.

Figure 4.14 shows the influence of the capillary tube total length. The mass flow rate rapidly decreases as the capillary tube length increases due to the increment of the pressure drop through it. The annular outlet temperature slightly increases due to the mass flow rate decrease. As regards the cycle parameters a remarkable decrease of the cooling capacity is observed together with a decrease of the compressor work. However, the effect of the capillary tube length in the cycle coefficient of performance is almost imperceptible.

The influence of the capillary tube diameter is studied in Figure 4.15. It is observed that higher mass flow rates are obtained for larger diameters due to the friction effect reduction. Thus, the annular fluid outlet temperature decreases. As regards the cycle parameters a remarkable increase of the cooling capacity is observed together with an
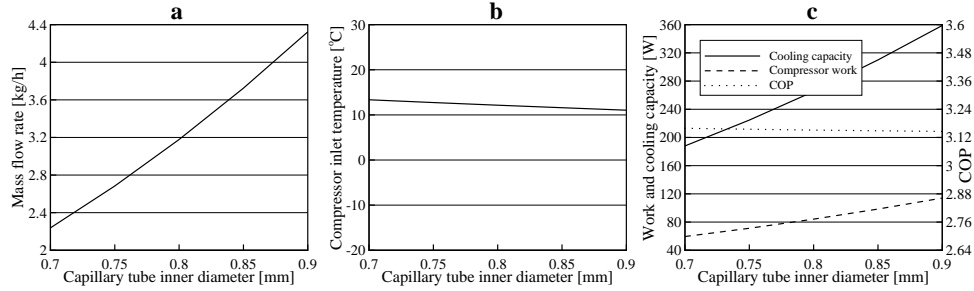
Figure 4.15: Influence of capillary tube diameter: (a) refrigerant mass flow rate, (b) compressor inlet temperature and (c) refrigerating cycle parameters.

increase of the compressor work. However, the effect of the capillary tube diameter in the cycle coefficient of performance is almost imperceptible.

Figure 4.16: Influence of the suction line tube diameter: (a) refrigerant mass flow rate, (b) compressor inlet temperature and (c) refrigerating cycle parameters.

The suction line inner diameter influence is studied in Figure 4.16. In this case a gentle decrease of the mass flow rate is observed as the concentric tube diameter increases. The annular cross section increases so that the annular mass velocity decreases and consequently the heat transfer coefficient is deteriorated. Thus, less heat is lost by the refrigerant that flows through the capillary tube and the global pressure drop increases (mass flow rate decreases). All the refrigerating system parameters decrease following the mass flow rate trends. However, the cooling capacity decreases more rapidly than the compressor work because the evaporator inlet gas weight fraction increases while the compressor inlet temperature decreases.

The tube roughness effect on the capillary tube behavior is analysed in Figure 4.17. The pressure drop through the capillary tube increases as the roughness increases so that the mass flow rate decreases. The annular flow outlet temperature does not present significant changes. Both the cooling capacity and the compressor work decrease but the cycle performance remains constant. A similar effect is seen for the capillary tube length influence (see Figure 4.14).
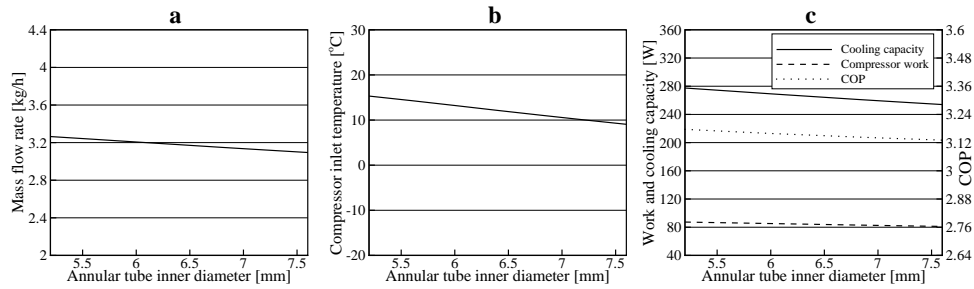

Figure 4.17: Influence of the capillary tube roughness: (a) refrigerant mass flow rate, (b) compressor inlet temperature and (c) refrigerating cycle parameters.

Figure 4.18: Influence of the superheating degree: (a) refrigerant mass flow rate, (b) compressor inlet temperature and (c) refrigerating cycle parameters.

Figure 4.18 shows the superheating degree effect. It is noticed that for the studied range the effect of the superheating degree is practically insignificant. The annular tube outlet temperature increases as the superheating degree increases (lower annular tube inlet temperature). In fact, the heat transferred through the double tube heat

exchanger slightly decreases so that the system mass flow rate also decreases. The refrigerating system parameters present insignificant variations.

The influence of the subcooling degree is shown in Figure 4.19. The effects on both the mass flow rate and annular outlet temperature are similar to those seen for the superheating degree but in the opposite direction (higher mass flow rate and lower annular tube outlet temperature). However, the cycle performance is improved as the cooling capacity increases more rapidly than the power consumption (due to the lower evaporator inlet gas weight fraction and the lower compressor inlet temperature).
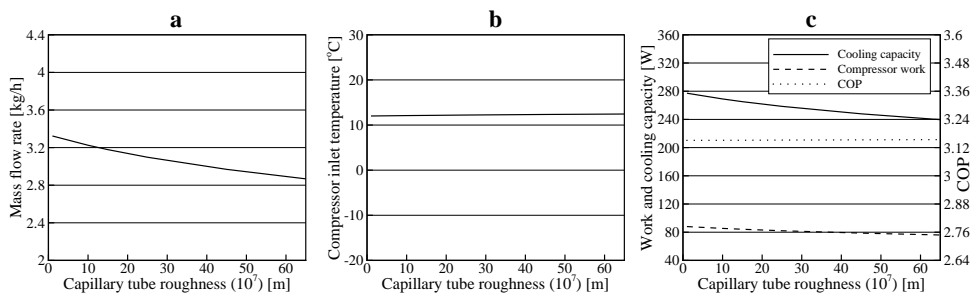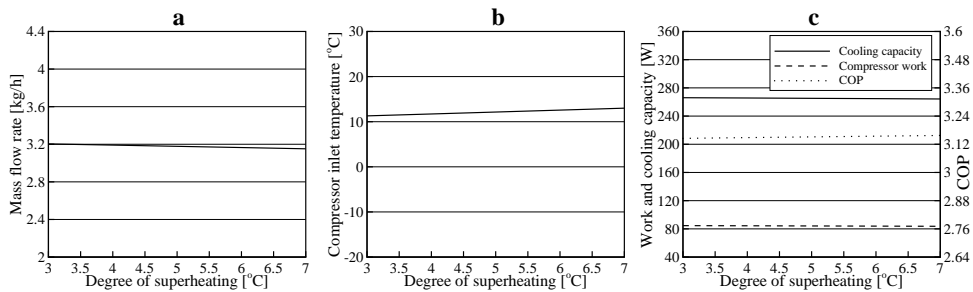

Figure 4.19: Influence of the subcooling degree: (a) refrigerant mass flow rate, (b) compressor inlet temperature and (c) refrigerating cycle parameters.

Figure 4.20: Influence of the evaporation temperature: (a) refrigerant mass flow rate, (b) compressor inlet temperature and (c) refrigerating cycle parameters.

Figure 4.20 shows the results for different evaporation temperatures. The global pressure drop decreases as the saturation temperature increases due to the two-phase

flow region shortening. This situation leads to lower mass flow rates and higher annular tube outlet temperatures. It is noticed that the cycle coefficient of performance increases because the compressor work decreases more rapidly than the cooling capacity (higher compressor suction line temperature but same degree of superheating).

Finally the influence of the condensation pressure is analysed in Figure 4.21. In this case the cycle coefficient of performance deteriorates as the condensation pressure rises up. The cooling capacity increases less than the compression work (lower evaporator inlet gas weight fraction).
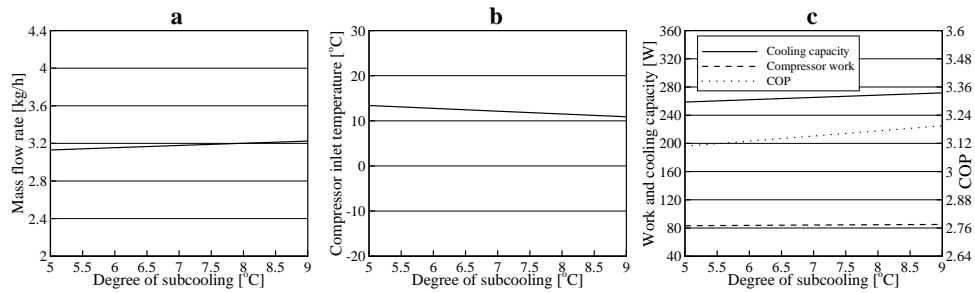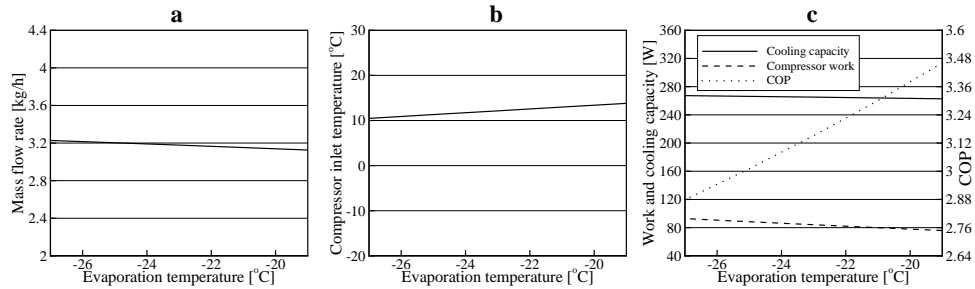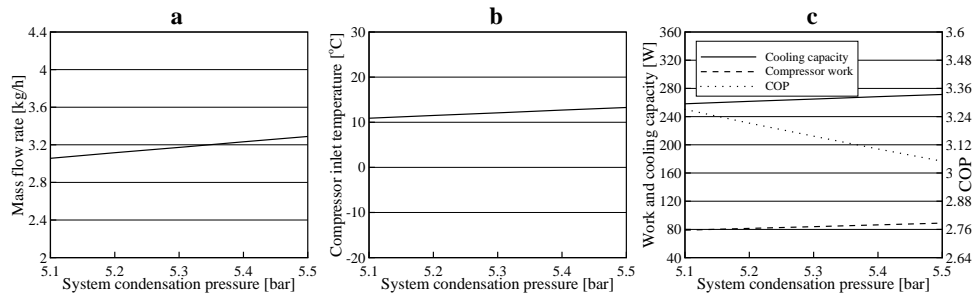

Figure 4.21: Influence of the condensation pressure: (a) refrigerant mass flow rate, (b) compressor inlet temperature and (c) refrigerating cycle parameters.

4.5   Conclusions

The capillary tube model has been detailed and appropriately implemented. The numerical results have been compared against adiabatic and non-adiabatic experimental cases found in the open literature. The effect of the metastable region has also been studied and validated with experimental data. In all the cases very good agreement has been obtained (maximum mean prediction error of about 10%).

The model capabilities have been shown by means of a parametric study carried out considering capillary tubes working with R-600a at typical household refrigerator conditions. The influence of different geometric parameters has been studied (roughness, diameter, length, etc.) as well as the influence of various operational parameters (subcooling and superheating degree, evaporation and condensation temperature, etc.) in order to analyse the capillary tube behavior and its theoretical influence over the whole refrigerating cycle.

Considering the conditions stated for this analysis some general conclusions are drawn from the numerical results: i) the mass flow rate increases as the resistance

to flow decreases inside the capillary tube (later set of the two-phase flow condition, shorter tube length, bigger diameter and smaller roughness); ii) the refrigerant temperature at the compressor suction line increases with the heat exchanger length (the other geometrical and operational variables show insignificant influence); and iii) both the system cooling capacity and compressor work trends are highly related to the mass flow rate profile. The COP increases as the heat exchanger length increases.

Nomenclature

c_p	specific heat capacity, $J \cdot kg^{-1} \cdot K^{-1}$
D	tube diameter, m
e	specific energy, $J \cdot kg^{-1}$
G	mass velocity, $kg \cdot m^{-2} \cdot s^{-1}$
g	acceleration due to gravity, $m \cdot s^{-2}$
K	Boltzmann's constant, $J \cdot K^{-1} \cdot mol^{-1}$
k	concentration factor
h	specific enthalpy, $J \cdot kg^{-1}$
L	tube length, m
MPE	mean prediction error, %
$\dot{m}$	mass flow rate, $kg \cdot s^{-1}$
n	number of control volumes
P	perimeter, m
Pr_l	Prandtl number of liquid phase, $(Pr_l = \frac{c_{p,l}\mu_l}{\lambda_l})$
p	pressure, Pa
$\dot{q}$	heat flux, $W \cdot m^{-2}$
R	gas constant, $J \cdot K^{-1} \cdot kg^{-1}$
Re_l	Reynolds number of liquid phase, $(Re_l = \frac{G(1-x_g)D}{\mu_l})$
Re	Reynolds number, $\frac{GD}{\mu}$
S	surface, cross section, m^2
s	standard deviation (dimensionless), specific entropy, $J \cdot kg^{-1} \cdot K^{-1}$
$\dot{s}_{gen}$	generation of entropy, $J \cdot K^{-1} \cdot m^{-3} \cdot s^{-1}$
T	temperature, K
t	time, s
V	volume, m^3
v	velocity, $m \cdot s^{-1}$
w	specific work, $J \cdot kg^{-1}$
x_g	gas weight fraction
z	axial position, m

Greek symbols

α	heat transfer coefficient, $W \cdot m^{-2} \cdot K^{-1}$
γ	isentropic index, $(\gamma = \frac{c_p}{c_v})$
ΔT_{sc}	degree of subcooling, K
Δz	axial step, m
ϵ	absolute roughness, m
ϵ_g	gas void fraction
ξ	accuracy
θ	inclination angle, rad
λ	thermal conductivity, $W \cdot m^{-1} \cdot K^{-1}$
μ	dynamic viscosity, $kg \cdot m^{-1} \cdot s^{-1}$
Π	compression ratio, $(\Pi = \frac{p_{out}}{p_{in}})$
ρ	density, $kg \cdot m^{-3}$
σ	surface tension, $N \cdot m^{-1}$
τ	shear stress, Pa
ϕ	discretized variable, correction expression
ϕ^2	two-phase frictional multiplier

Subscripts

c	kinetic
cap	capillary tube
cb	convective boiling
cr	critical
$comp$	compressor inlet
dis	discharge
$equi$	thermodynamic equilibrium
ext	external
g	gas phase
i	grid position
in	inlet
l	liquid phase
m	superheated liquid
nb	nucleate boiling
out	outlet
p	potential
s	surface, isentropic
sat	saturation
tp	two-phase

v	vaporization, volume
$wall$	wall (solid part in contact with liquid)

Superscripts

bc	boundary condition

References

[1] ASHRAE. *Refrigeration Handbook S.I. Edition*. ASHRAE Inc., Atlanta, GA, 1998.

[2] M. K. Khan, R. Kumar, and P. K. Sahoo. Flow characteristics of refrigerants flowing through capillary tubes - A review. *Applied Thermal Engineering*, 29(8-9):1426–1439, 2009.

[3] E. P. Mikol. Adiabatic single and two-phase flow in small bore tubes. *ASHRAE Journal*, 5:75–86, 1963.

[4] R. Y. Li, S. Lin, Z. Y. Chen, and Z. H. Chen. Metastable flow of R-12 through capillary tubes. *International Journal of Refrigeration*, 13(3):181–186, 1990.

[5] F. Escanes, C. D. Pérez-Segarra, and A. Oliva. Numerical simulation of capillary tube expansion devices. *International Journal of Refrigeration*, 18(2):113–122, 1995.

[6] O. García-Valladares, C. D. Pérez-Segarra, and A. Oliva. Numerical simulation of capillary-tube expansion devices behaviour with pure and mixed refrigerants considering metastable region. Part I: Mathematical formulation and numerical model. *Applied Thermal Engineering*, 22(2):173–182, 2002.

[7] O. García-Valladares, C. D. Pérez-Segarra, and A. Oliva. Numerical simulation of capillary-tube expansion devices behaviour with pure and mixed refrigerants considering metastable region. Part II: Experimental validation and parametric studies. *Applied Thermal Engineering*, 22(4):379–391, 2002.

[8] S. W. Churchill. Frictional equation spans all fluid flow regimes. *Chemical Engineering*, 84(24):91–92, 1977.

[9] L. Friedel. Improved friction pressure drop correlation for horizontal and vertical two-phase pipe flow. In *Proceedings of the European Two-Phase Flow Group Meeting*, 1979.

[10] V. Gnielinski. New equations for heat and mass transfer in turbulent pipe and channel flow. *International Chemical Engineering*, 16(2):359–368, 1976.

[11] W. H. McAdams. *Heat Transmission*. 3rd ed., McGraw-Hill, New York, 1954.

[12] A. Premoli, D. Francesco, and A. Prima. An empirical correlation for evaluating two-phase mixture density under adiabatic conditions. In *Proceedings of the European Two-Phase Flow Group Meeting*, 1970.

[13] O. García-Valladares. Numerical simulation of non-adiabatic capillary tubes considering metastable region. Part i: Mathematical formulation and numerical model. *International Journal of Refrigeration*, 30(4):642–653, 2007.

[14] Z. H. Chen, R. Y. Li, S. Lin, and Z. Y. Chen. A correlation for metastable flow of refrigerant 12 through capillary tubes. *ASHRAE Transactions*, 96(1):550–554, 1990.

[15] V. Feburie, M. Goit, S. Granger, and J. M. Seynhaeve. A model for choked flow through cracks with inlet subcooling. *International Journal of Multiphase Flow*, 19(4):541–562, 1993.

[16] R. Y. Li, S. Lin, and Z. H. Chen. Numerical modelling of thermodynamic non-equilibrium flow of refrigerant through capillary tubes. *ASHRAE Transactions*, 96(1):542–549, 1990.

[17] C. Melo, L. A. Torquato, and R. Horn. Non-adiabatic capillary tube flow with isobutane. *Applied Thermal Engineering*, 22(14):1661–1672, 2002.

Chapter 5

Two-phase Flow Distribution in Heat Exchangers

ABSTRACT

This chapter is devoted to the development of a numerical simulation model that predicts the two-phase flow distribution in systems with multiple branching tubes (e.g. heat exchanger manifold systems). The simulated system is geometrically represented as a set of tubes connected together by means of junctions. On one side, the in-tube evaporation/condensation phenomena are simulated by means of a one-dimensional two-phase flow model, and on the other side, the splitting/converging flow phenomena occurring at junctions are predicted with appropriate junction models obtained from the technical literature. The global flow distribution is calculated using a semi-implicit pressure based model (SIMPLE-like algorithm) where the continuity and momentum equations of the whole domain are solved and linked with both the in-tube two-phase flow model and the junction models.

In the following sections, the flow distribution model is described and its most significant aspects are detailed. Furthermore, the model is validated against experimental and numerical data found in the open literature. The numerical predictions are compared against an adiabatic single-phase flow manifold system working with water and a two-phase flow upwardly oriented manifold system working with carbon dioxide. In addition to this, parametric studies are presented for two-phase flow manifold systems considering different geometric and operational conditions. Concluding remarks about the possibilities that this kind of model offers are presented in the last section. The main contents of this chapter are published in the *International Journal of Thermal Sciences*.

5.1   Introduction

In many heat exchangers, such as those used in refrigerating systems, the inner fluid is distributed in several tubes in order to realize high cycle COP and to reduce the heat exchanger size (Watanabe et al. [1]). The flow distribution is usually achieved by means of manifold/header systems. A typical arrangement includes a dividing manifold, a set of parallel tubes where the heat transfer process takes place, and a combining manifold where the whole flow is regrouped again. In general, a heat exchanger performs better when the mass flow rate is uniformly distributed through the intermediate tubes. However, an uneven distribution may occur and the heat exchanger thermal and hydraulic performance may deteriorate. This maldistribution situation is particularly unfavourable for two-phase flows due to the possible uneven phase split at each junction of the dividing manifold.

For instance, in an evaporator with unequal flow distribution the heat transfer varies from tube to tube depending on both the tube flow conditions (e.g. mass flow rate, inlet gas weight fraction) and the external heat load. This situation may lead to the undesirable presence of the dry-out phenomena - or an earlier set than the expected - in some tubes. Consequently, the heat transferred by these tubes will steeply decrease as well as the global heat exchanger performance. A uniform liquid distribution is also recommended for better heat transfer performance in condensers. Thus, the prediction of the flow distribution in a manifold is a crucial aspect to consider for the heat exchanger design optimization.

During the last decades, a significant amount of experimental and numerical research works have been focused on studying the flow distribution in manifold/header systems. Different works dealing with single-phase fluids have shown that the flow distribution depends mainly on the pressure drop related to both the friction through tubes/manifolds and the flow split at junctions [2–4]. However, when two-phase flows are considered the flow distribution prediction becomes a harder task. The phase split phenomena are very complex and depend not only on geometric parameters (size, shape, position and orientation of both the manifold and the tubes), but also on the flow conditions (mass velocity, gas weight fraction and flow pattern) and on the heat load applied to each tube (Mueller and Chiou [5]). Research efforts have been done for a wide variety of fluids, operating conditions, heat exchanger types and geometries. The most relevant experimental studies and numerical attempts carried out on this topic are summarised in both Hwang et al. [6] and Marchitto et al. [7]. In fact, no general two-phase flow distribution prediction model has been proposed yet.

The aim of the work presented in this chapter is the development of a numerical model to predict the flow distribution in systems with branching conduits. The basic idea of the model is to represent the studied domain as a set of tubes connected by means of junctions. Both the fluid-dynamic and the heat transfer phenomena occurring inside the tubes and manifolds are solved with the two-phase flow in-tube

one-dimensional model detailed in Chapter 2. The pressure change in all junctions and the phase split at dividing junctions are solved using appropriate junction models found in the open literature [8–11]. The global resolution procedure consists on solving the mass and momentum equations applied to the whole system and to relate them with both the fluid and the junction models in order to predict the thermal behavior and the flow distribution of the studied domain.

In the following section of the present chapter the model is described in detail. In the third section, the model is validated against experimental and numerical data from other authors. Two main experimental cases are considered: a single-phase flow manifold system working with water and a two-phase flow manifold system working with carbon dioxide. The former represents a solar collector and the latter consists of an upwardly oriented automotive air conditioner evaporator. In the fourth section two numerical studies are presented in order to show the model capabilities. On one side, an extensive parametric study is carried out on a manifold system working with R-134a in order to show the model flexibility, and on the other side, a two-phase flow evaporator is studied at two different orientations (horizontal manifold with horizontal tubes and horizontal manifold with upwardly oriented tubes). Finally, concluding remarks are given.

5.2 Numerical model

The global numerical resolution process is based on the coupling of three different numerical models related to: i) the phase split and the pressure drop occurring at junctions; ii) the thermal and fluid-dynamic behavior of the two-phase flow through both tubes and manifolds themselves; and iii) the global momentum and continuity conservation equations coupled over the whole manifold system. Both the domain discretization and the main details of the resolution process are described in this section.

5.2.1 Domain discretization

The domain is discretized at two different levels. The higher level represents the whole heat exchanger which is discretized by means of nodes (placed at branch ends) and branches (tubes/channels between two adjacent nodes) as shown in Figure 5.1. The working fluid state is defined at each node by means of two properties, the pressure and the enthalpy, while its mass flow rate is defined at each branch. These values are calculated with the resolution procedures presented in Sections 5.2.4 and 5.2.5.

The lower level represents the manifold system branches (e.g. manifold sections placed between two adjacent junctions as well as tubes placed between manifolds). They are discretized in concatenated control volumes which represent different types
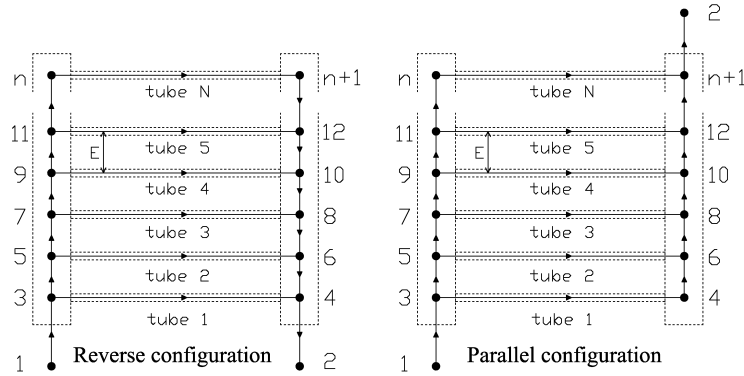
Figure 5.1: Manifold system discretization for two different configurations.

of elements, such as: dividing junctions, combining junctions, tubes, etc. The flow pressure and enthalpy variation between the upstream and downstream positions of an element (or control volume) depends on the element specific characteristics.
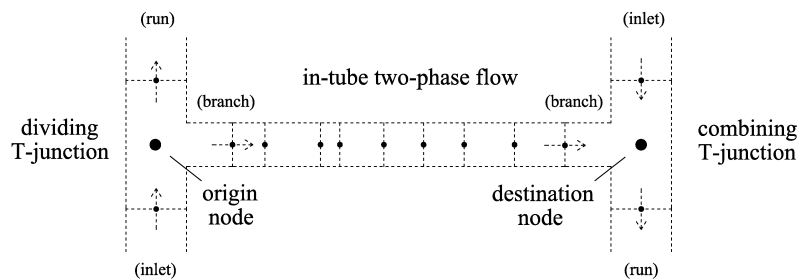
Figure 5.2: Typical branch elements of a tube placed between a dividing and a combining manifolds; T-junctions characterisation in brackets.

The diagram depicted in Figure 5.2 shows the typical branch elements found on a heat exchanger tube placed between the dividing and the combining manifolds. In this particular case, the behavior of the first element is characterised from an appropriate dividing T-junction model (see Section 5.2.2), the second element is simulated by means of a two-phase flow numerical model (see Section 5.2.3), and the last element

is characterised from a convenient converging T-junction model (see Section 5.2.2). The pressure variation through the whole branch is obtained from the integration of its elements along the whole fluid path (see Section 5.2.4).

Each branch is defined from an origin to a destination node which do not necessarily agree with the flow direction. These nodes represent T-junctions and they are equivalent to the nodes depicted in Figure 5.1. Both the fluid state (enthalpy and pressure) and its mass flow rate are defined for the three nodes placed at the junction ends (branch, run and inlet). The working fluid state of the branch origin/destination node correspond to the T-junction inlet or run node depending on the flow direction.

5.2.2 T-junction models

Appropriate junction models are needed in order to predict the pressure change (in dividing and combining T-junctions) and the phase split (in two-phase flow dividing junctions) of a whole heat exchanger manifold system. However, the reliable use of these models - specially for the phase split prediction - is limited to their experimental ranges and conditions. It should be also considered that some effects that occur in manifold systems (e.g. backward flow, influence of adjacent junctions) are not taken into account by the models. In this section the specific T-junction models used in this work for both single- and two-phase flows are briefly described.

Single-phase pressure change evaluation

The single-phase fluid pressure change through converging and diverging T-junctions is predicted with the expressions reported by Idelchik [12]. In that work a wide variety of operational conditions and geometric configurations were taken into account.
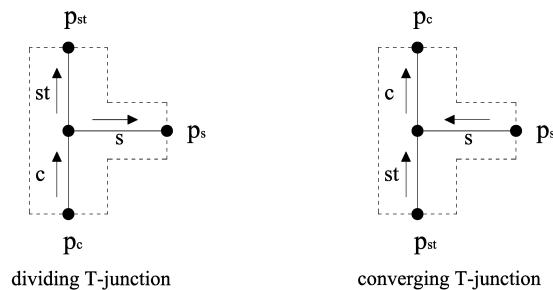

Figure 5.3: Characterisation of single-phase flow dividing and converging T-junctions (Idelchik [12]).

According to the nomenclature of Idelchik (Figure 5.3) the pressure variation throughout the main pipe of a diverging/converging junction is expressed by means of a flow resistance coefficient (ξ_{st}) as follows:

$$p_{st} - p_c = \rho \frac{v_{st}^2}{2} \left(\xi_{st} - 1 + \left(\frac{v_c}{v_{st}} \right)^2 \right) \tag{5.1}$$

And the prediction of the pressure variation through the lateral branch of a diverging/converging junction is calculated by means of the flow resistance coefficient (ξ_s) as follows:

$$p_s - p_c = \rho \frac{v_s^2}{2} \left(\xi_s - 1 + \left(\frac{v_c}{v_s} \right)^2 \right) \tag{5.2}$$

The flow resistance coefficients depend on the Reynolds number, on the T-junction cross-sectional areas (S_{st}, S_c and S_s) and on the volumetric flow rates. They include all the sources of pressure loss occurring at junctions (sudden expansions, flow turning, turbulent mixing, friction through passages, etc.) and are calculated with additional expressions and empirical values also reported by Idelchik [12].

Two-phase flow pressure change evaluation

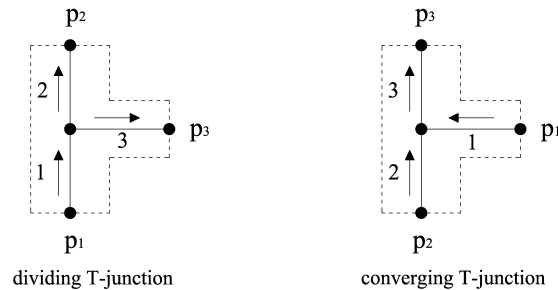**Figure 5.4:** Characterisation of two-phase flow dividing and converging T-junctions.

The usual two-phase flow T-junction characterisation is shown in Figure 5.4. In the dividing junction the indexes 1, 2 and 3 represent the inlet, the run, and the branch positions, respectively. In the converging T-junction, the indexes 1, 2 and 3 represent the branch, the inlet, and the run positions, respectively.

Dividing T-junctions

For the prediction of the two-phase flow pressure change through dividing T-junctions several models have been presented in the literature. Buell et al. [13] published a complete summary of the available models. The model implemented in this work is based on the two-phase Bernoulli equation (Tae and Cho [11]), where according to the nomenclature of Figure 5.4 (left), the pressure variation through the main channel is described as a reversible pressure change (momentum change due to the decrease of the flow rate):

$$p_2 - p_1 = (\Delta p_{1-2})_{rev} \tag{5.3}$$

$$(\Delta p_{1-2})_{rev} = \frac{1}{2} \left\{ G_1^2 \left(\frac{x_{g1}^2}{\epsilon_{g1}\rho_g} + \frac{(1 - x_{g1})^2}{(1 - \epsilon_{g1})\rho_l} \right) - G_2^2 \left(\frac{x_{g2}^2}{\epsilon_{g2}\rho_g} + \frac{(1 - x_{g2})^2}{(1 - \epsilon_{g2})\rho_l} \right) \right\} \tag{5.4}$$

While the pressure change through the branch tube is calculated from two terms: the reversible pressure change and an irreversible pressure variation due to both the change of the flow direction and the orifice effect at the entrance of the branch tube. The corresponding equations are:

$$p_3 - p_1 = (\Delta p_{1-3})_{rev} + (\Delta p_{1-3})_{irr} \tag{5.5}$$

$$(\Delta p_{1-3})_{rev} = \frac{1}{2} \left\{ G_1^2 \left(\frac{x_{g1}^2}{\epsilon_{g1}\rho_g} + \frac{(1 - x_{g1})^2}{(1 - \epsilon_{g1})\rho_l} \right) - G_3^2 \left(\frac{x_{g3}^2}{\epsilon_{g3}\rho_g} + \frac{(1 - x_{g3})^2}{(1 - \epsilon_{g3})\rho_l} \right) \right\} \tag{5.6}$$

$$(\Delta p_{1-3})_{irr} = \frac{K_{1-3}}{2} \frac{G_1^2 (1 - x_{g1})^2}{\rho_l} \left(1 + \frac{C_{1-3}}{X} + \frac{1}{X^2} \right) \tag{5.7}$$

$$K_{1-3} = 0.95(1 - F_l)^2 + 0.8F_l(1 - F_l) + 1.3F_l^2 \tag{5.8}$$

$$C_{1-3} = \left[1 + 0.75 \left(\frac{\rho_l - \rho_g}{\rho_l} \right)^{0.5} \right] \left[\left(\frac{\rho_l}{\rho_g} \right)^{0.5} \left(\frac{\rho_g}{\rho_l} \right)^{0.5} \right] \tag{5.9}$$

Where the single-phase friction loss coefficient (K_{1-3}) is calculated with the expression of Gardel [14] (Equation 5.8) and the parameter C_{1-3} is calculated from the equation proposed by Chisholm and Sutherland [15] for two-phase flows in T-type junctions (Equation 5.9).

Combining/converging T-junctions

The research done for the present chapter shows that only three semi-empirical models have been reported in the open literature to predict the pressure change through two-phase flow combining T-junctions. These models were derived from existing dividing T-junction models and were presented in Schmidt and Loth [16]. The three models contain some common parameters that were determined by Schmidt and Loth based on physical/methodological assumptions and visual observations. Several expressions/values were proposed to estimate the shared parameters. It was shown that the best agreement between each model and some experimental measurements for R-12 was achieved with the same set of expressions/values for the common parameters.

The model used in this work is the the so-called "contraction coefficient model" which considers that both incoming flows are contracted as they come together (flows 1 and 2 of Figure 5.4 right). The model main idea is to divide each flow path into two regions: before their maximal contraction and after it. The first region is assumed to be non-dissipative and it is calculated by means of an energy equation. The second region is considered dissipative and it is calculated by means of a momentum balance. The pressure change equations of both flow paths are defined as follows:

$$p_1 - p_3 = \frac{\rho_1 v_1^2}{2} \left(\frac{1}{k_{c,13}^2} - F_{<\rho v^3>1} \right) + \rho_3 v_3^2 - \frac{\rho_1 v_1^2}{k_{c,13}} - \frac{\rho_2 v_2^2}{k_{c,23}} + \Delta p_{ad} \qquad (5.10)$$

$$p_2 - p_3 = \frac{\rho_2 v_2^2}{2} \left(\frac{1}{k_{c,23}^2} - 1 \right) + \rho_3 v_3^2 - \frac{\rho_1 v_1^2}{k_{c,13}} - \frac{\rho_2 v_2^2}{k_{c,23}} + \Delta p_{ad} \qquad (5.11)$$

The average density at the i position of the T-junction is ρ_i while the corresponding average velocity is v_i. The term $F_{<\rho v^3>1}$ is the streamline correction coefficient, Δp_{ad} is the additional pressure change and $k_{c,ij}$ is the contraction coefficient. These are the shared parameters mentioned before which are evaluated according to some assumptions by means of empirical correlations/values provided by Schmidt and Loth [16].

Two-phase flow phase split

In addition to the pressure change calculation, the phase split has to be predicted in dividing T-junctions (see Figure 5.4, left). This problem represents a great challenge for researchers because of its complexity and the large number of variables involved. The flow separation is strongly affected by the gas and the liquid flow rates, the mass extraction rate ($\dot{m}_3/\dot{m}_1$), the flow pattern upstream of the junction, the fluid physical properties and both the junction geometry and orientation. In the present section,

two models obtained from the technical literature are briefly described. Both predict the branch gas weight fraction (x_{g3}) from the dividing T-junction incoming conditions ($\dot{m}_1$, x_{g1}, and flow pattern) and the branch mass flow rate ($\dot{m}_3$).

Horizontal T-junction with upwardly oriented branch

The correlation presented by Seeger et al. [8] is used to predict the phase split in T-junctions with an horizontal main tube and a vertical upward oriented branch. This correlation is purely empirical and consists on a very simple relation between the incoming flow conditions and the branch outcoming mass flow rate:

$$x_{g3} = x_{g1} \left(\frac{\dot{m}_3}{\dot{m}_1} \right)^{-0.8} \tag{5.12}$$

The correlation was based on experiments where the flow parameters were varied over a wide range in order to consider different inlet flow patterns. All the measurements were carried out in a 50 mm inner diameter T-junction and for mass extraction rates above 0.15 ($\dot{m}_3/\dot{m}_1 \geq 0.15$). The influence of the inlet conditions was found to be relatively small. However, the proposed expression (Equation 5.12) is not valid for low mass extraction rate values because liquid carryover does not occur in this condition ($x_{g3} = 1$). In fact, the maximum branch mass velocity with pure gas phase flow is estimated from an additional relation proposed also by Seeger et al. [8]:

$$G_{3,max} = 0.23A(gD_1\rho_g(\rho_l - \rho_g))^{0.5} \tag{5.13}$$

Where the value of A is obtained according to the flow pattern at the T-junction inlet position (0.5 for dispersed bubble regime and 1.0 for all other regimes).

Horizontal T-junction with horizontally oriented branch

For T-junctions with incoming annular or stratified flow patterns, with both the main tube and the branch placed horizontally, the phenomenological semi-empirical model of Hwang et al. [9] is used. The model is based on the dividing streamline concept: the gas or liquid flow located in the area at the right side of its corresponding dividing streamline is diverted into the branch tube (see Figure 5.5).

A force balance, assuming that the centrifugal and interfacial drag forces are dominant, is applied between the dividing streamlines of gas and liquid. For separated two-phase flow patterns, such as stratified or annular, the interfacial drag force is relatively small and the model of Hwang et al. [9] simplifies to a balance between the centrifugal forces:
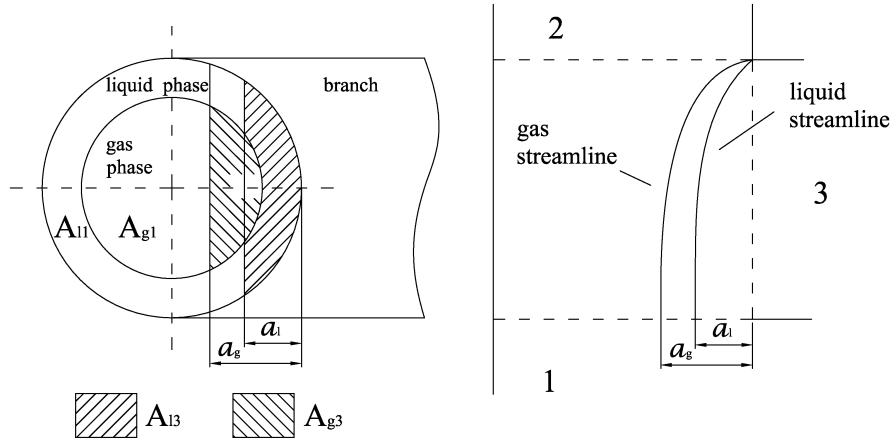
Figure 5.5: Gas and liquid dividing streamlines of a dividing T-junction with upstream annular flow pattern.

$$\frac{\rho_g v_g^2}{R_g} = \frac{\rho_l v_l^2}{R_l} \tag{5.14}$$

The shape of each streamline must be known in order to find its radius of curvature (R). Based on an approximated equation that describes a streamline, Hwang et al. [9] presented an expression to predict the radius value. Consequently, the radii relation was assumed to satisfy the following expression:

$$\frac{R_g}{R_l} = \frac{\left(\frac{a_l}{D_1}\right)^{n_l}}{\left(\frac{a_g}{D_1}\right)^{n_g}} \tag{5.15}$$

Where a_l and a_g are the positions of the liquid and gas streamlines respectively (see Figure 5.5). The exponent n_k was determined from the Hwang et al. [9] data, and to estimate it the following empirical correlation was recommended:

$$n_k = 5 + 20^{\left(-53\frac{a_k}{D_1}\right)} \tag{5.16}$$

The subscript k represents either the gas phase (g) or the liquid phase (l). The final force balance expression is deduced from Equations 5.14 and 5.15:

$$\frac{\left(\frac{a_l}{D_1}\right)^{n_l}}{\left(\frac{a_g}{D_1}\right)^{n_g}} = \frac{\rho_g v_g^2}{\rho_l v_l^2} \tag{5.17}$$

In addition to this, the gas and liquid extraction rates are also expressed in terms of the gas and liquid area ratios of Figure 5.5:

$$\begin{aligned}
F_g &= \frac{\dot{m}_{g3}}{\dot{m}_{g1}} = \frac{A_{g3}}{A_{g1}} \\
F_l &= \frac{\dot{m}_{l3}}{\dot{m}_{l1}} = \frac{A_{l3}}{A_{l1}}
\end{aligned} \tag{5.18}$$

The areas A_{g3} and A_{l3} are geometrically related to the values of a_g and a_l respectively. The specific relations for the annular and stratified flow patterns are detailed in Appendix A.

The flow pattern map reported by Thome [17] is used in the numerical model presented herein in order to determine the flow pattern of the T-junction incoming flow. This map was developed for fluids through horizontal tubes.
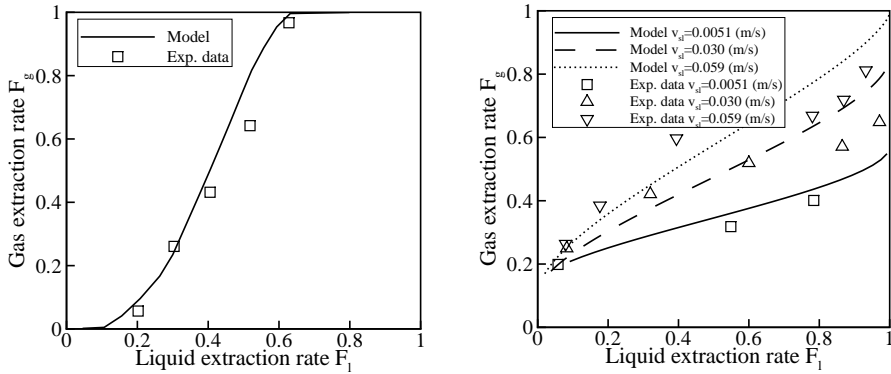

Figure 5.6: Hwang et al. model [9] compared against horizontal oriented T-junctions experimental data of Tae and Cho [11] (annular flow, left) and Marti and Shoham [10] (stratified flow, right).

Illustrative results are shown in Figure 5.6 where the dividing T-junction model of Hwang et al. [9] is compared against both annular and stratified flow experimental

data. On one hand, the annular flow regime experimental data have been taken from Tae and Cho [11] (Figure 5.6, left). The test was carried out with R-22 in a horizontally oriented T-junction (main tube and branch) and for annular flow regime. The test conditions were: inner diameter 8.12 mm, inlet mass velocity 300 kg/m^2s, and inlet weight fraction 0.3. In fact, this result was already reported by Tae and Cho [11] where some modifications to the model of Hwang et al. [9] were proposed. On the other hand, the stratified flow regime experimental data have been taken from Marti and Shoham [10] (Figure 5.6, right). In this case the fluid consisted of an air and water mixture. The test conditions were: gas superficial velocity 6.1 m/s, inner diameter 51 mm, inlet pressure 295 kPa and liquid superficial velocities ranging from 0.0051 to 0.059 m/s. It is observed that the general trends of the experimental profiles are well predicted with the model. The effect that occurs in the experimental cases of Marti and Shoham when the liquid superficial velocity increases (higher slope in the F_l vs F_g profile) is also noticed in the model results.

x_{g1}	$\dot{m}_3/\dot{m}_{g1}$	x_{g2}	x_{g3}
0.100	0.7	0.0000	0.143(0.143)
0.100	0.5	0.0000	0.200(0.200)
0.100	0.3	0.0012	0.329(0.333)
0.250	0.7	0.0060	0.350(0.357)
0.250	0.5	0.0080	0.488(0.500)
0.250	0.3	0.0110	0.799(0.833)
0.500	0.7	0.0130	0.695(0.714)
0.500	0.3	0.0250	1.580(1.666)

Table 5.1: Exp. results of Saba and Lahey Jr. [18] (results obtained with the Hwang et al. model [9] in brackets).

Additional predictions of the Hwang et al. model have been compared against experimental data for stratified air/water flows reported by Saba and Lahey [18]. The test conditions were: horizontal main tube and branch, inlet water pressure 41370 Pa, inlet water temperature 298.15 K (14900 J/kg), T-junction diameter 0.0381 m, inlet mass velocity 1355 kg/m^2s, inlet weight fractions 0.10, 0.25 and 0.50 and mass extraction rates 0.3, 0.5 and 0.7. The results are shown in table 5.1. The agreement between the model and the experimental data is very good. According to Equation 2.57 the mean prediction error is 2.2%.

5.2.3 Numerical simulation of in-tube two-phase flow and the solid elements

The numerical simulation model of the thermal and fluid-dynamic behavior of two-phase flow inside tubes is obtained from the integration of the fluid governing equa-

tions along the flow domain, which is split into a number of finite control volumes as is shown in Figure 2.1. Considering a steady-state quasi-homogeneous fully-implicit one-dimensional model, the discretized governing equations (continuity, momentum and energy) show the following form:

$$\dot{m}_i - \dot{m}_{i-1} = 0 \tag{5.19}$$

$$\dot{m}_i v_i - \dot{m}_{i-1} v_{i-1} = (p_{i-1} - p_i)S - \bar{\tau}_i \pi D \Delta z_i - \bar{\rho}_i g sin(\theta) S \Delta z_i \tag{5.20}$$

$$\dot{m}_i(h_i + e_{c,i} + e_{p,i}) - \dot{m}_{i-1}(h_{i-1} + e_{c,i-1} + e_{p,i-1}) = \bar{\dot{q}}_i \pi D \Delta z_i \tag{5.21}$$

This formulation requires the use of empirical correlations to evaluate the void fraction, the shear stress and the heat transfer coefficient. The most important details of this model have been presented in Chapter 2. The resolution is carried out on the basis of a SIMPLE-like algorithm or a step-by-step numerical scheme. In the latter case, the governing equations are rearranged and solved for the control volume downstream node. Thus, from the inlet flow conditions (i.e. $\dot{m}_1, p_1, h_1$) each control volume outlet state is calculated sequentially. The tube wall temperature map acts as the boundary condition for the whole internal flow.

The energy balance over the solid part of the tube is also considered. The tube is discretized in a way, that for each fluid control volume, there is a corresponding tube temperature (see Figure 2.1). The balance takes into account the conduction heat transfer along the tube itself together with the heat transferred to/from the external environment and the heat exchanged with the internal fluid. The discretized energy equation applied at each solid control volume is expressed as follows:

$$-\lambda_{i_-} \frac{T_i - T_{i-1}}{z_i - z_{i-1}} S + \lambda_{i_+} \frac{T_{i+1} - T_i}{z_{i+1} - z_i} S + \bar{\dot{q}}_{ext,i} \pi D_{ext} \Delta z_i - \bar{\dot{q}}_i \pi D \Delta z_i = 0 \tag{5.22}$$

The process of solving in a segregated way the inner fluid, the solid tube and the external condition (if necessary), is carried out iteratively until a converged solution is obtained. The solution is given when all the variables (mass flow rate, pressure, enthalpy, tube temperatures and external variables) agree with the convergence criteria $(|(\phi^* - \phi)/\phi| \le \xi)$.

5.2.4 Numerical simulation of flow distribution in assembled tubes

The global flow distribution through a whole manifold system is calculated by means of a flexible model that couples the T-junctions models with the in-tube two-phase

flow model. The solution is obtained iteratively by solving two different steps as follows:

• The first step consists on defining the pressure behavior of branches. As shown in Figure 5.2, each branch is composed of different elements such as T-junctions and tubes (each element may be split in two or several control volumes). The branch is solved, element by element, from its current mass flow rate and the working fluid conditions at its upstream node. The pressure change through each control volume is expressed by means of the following expression:

$$(p_o S_o - p_d S_d)_i = A_{1,i}|\dot{m}|\dot{m} + A_{2,i}\dot{m}^2 + B_i\dot{m} + C_i \qquad (5.23)$$

Where A_1, A_2, B and C represent coefficients to be determined, and the subindexes o (origin) and d (destination) indicate the branch ends which do not necessarily agree with the flow direction. For a T-junction control volume, these coefficients are obtained by rearranging the momentum equation of the corresponding T-junction model (see Section 5.2.2). For the in-tube flow control volumes, the coefficients are obtained by rearranging the momentum equation of the two-phase flow model (Equation 5.20). Thus, the pressure coefficients of all the branch control volumes are sequentially added and the branch global momentum equation is defined as follows:

$$p_o S_o - p_d S_d = \left(\sum A_{1,i}\right)|\dot{m}|\dot{m} + \left(\sum A_{2,i}\right)\dot{m}^2 + \left(\sum B_i\right)\dot{m} + \sum C_i \qquad (5.24)$$

• The second step consists on solving the whole flow distribution (mass flow values of branches and pressure values at nodes). To predict the flow distribution, a one-dimensional adaptation of the SIMPLE method has been implemented (Patankar [19]). In this sense, an expression for the mass flow at each branch is deduced from Equation 5.24:

$$\dot{m} = \frac{p_o S_o - p_d S_d - \sum C_i}{\left(\sum A_{1,i}\right)|\dot{m}| + \left(\sum A_{2,i}\right)\dot{m} + \sum B_i} = d_{od}(p_o S_o - p_d S_d - \sum C_i) \qquad (5.25)$$

The algorithm starts with a guessed pressure field (p^*). The mass flow predicted by the momentum equation ($\dot{m}^*$) should be modified by a correction mass flow ($\dot{m}'$) in order to determine an updated mass flow ($\dot{m}$) that accomplishes the continuity equation. Based in the linear momentum expression (Equation 5.25) the correction mass flow is evaluated from the correction pressures (p') as follows:

$$\dot{m}' = d_{od}(p_o' S_o - p_d' S_d) \qquad (5.26)$$

Considering the relation between flows ($\dot{m} = \dot{m}^* + \dot{m}'$) together with Equation 5.26, the mass conservation equation applied at each node of the discretized manifold system ($\sum \dot{m} = 0$) takes the following form:

$$\sum_{i=node\ as\ o} d_{od,i}(p'_{node}S_{o,i} - p'_{d,i}S_{d,i}) - \sum_{i=node\ as\ d} d_{od,i}(p'_{o,i}S_{o,i} - p'_{node}S_{d,i}) = \sum \dot{m}^*$$
(5.27)

The set of mass conservation equations is solved and new values of p' are obtained. From both the predicted and correction values, new pressure values are determined ($p = p^* + p'$). The convergence is reached iteratively. More information about the resolution procedure is detailed in Oliet [20].

The boundary conditions needed for the resolution can be applied at any node of the manifold system mesh. For a manifold system it will be enough to define the mass flow or the pressure at the inlet/outlet nodes (nodes 1 and 2 of Figure 5.1).

5.2.5 Energy balance at nodes

The enthalpy value at each node (Figure 5.1) is obtained from an energy balance considering all the incoming and outcoming flows:

$$\sum \dot{m}h = 0$$
(5.28)

The thermal behavior along branches (between their origin and their destination nodes) is calculated with the two-phase flow model presented in Section 5.2.3. The heat transfer in junctions is neglected. The inlet conditions needed to feed the two-phase flow model are obtained from the branch upstream node conditions (or the upstream T-junction outlet conditions).

5.2.6 Global resolution algorithm

The steady state solution of a flow distribution inside a heat exchanger with parallel tubes is obtained iteratively as follows:

1. The temperature map of all the tubes (solid part) is guessed or defined. Furthermore, both the working fluid state at nodes and the mass flow in branches are guessed or defined.
2. The nodes representing T-junctions are solved and their information (local pressure drop coefficients $A_{1,i}$, $A_{2,i}$, B_i and C_i) is transferred to the corresponding branch element.
3. The elements of each branch are solved sequentially in the flow direction. Each element is calculated from the outlet condition of the previous element, hence, the

first branch element is calculated from the branch upstream manifold system node conditions. On one hand, the pressure drop coefficients of each element are added and a momentum equation for each branch is obtained (Equation 5.24). On the other, the enthalpy at the end of each branch is obtained after solving the in-tube two-phase flow model.

4. The whole net is solved on the basis of each branch pressure characterisation (Equation 5.25) in order to obtain both an updated mass flow distribution and new pressure values at nodes. The enthalpies at the manifold system nodes are calculated from the energy conservation equation.

5. The values of nodes and branches of the previous iteration are compared against the current ones. If the convergence criteria are not met then the algorithm must restart with the latest conditions (step 2).

6. The solid elements (tubes) are calculated from Equation 5.22 considering both the new internal fluid flow maps and the updated heat exchanger external conditions (natural convection, forced convection, etc.).

7. The temperature maps of tubes are compared against the maps of the previous iteration and if the convergence criteria are not met then the algorithm must restart with the latest temperature map (step 2).

5.3   Numerical vs. experimental results

In this section, the present flow distribution model is compared against experimental data and numerical results for single- and two-phase flow manifold systems reported in the technical literature. The junction models used in this work are of the T-type and for round cross section configurations. Therefore, the cross-sectional areas of both the manifolds and the parallel tubes of the selected experimental cases are circular and the global geometric configuration is similar to that presented in Figure 5.1. In the cases simulated with the present model, the influence of the recirculation phenomena inside manifolds must be low, as well as the flow alterations transmitted between consecutive junctions, in order to appropriately represent the manifold system by means of junctions and tubes. This restriction is also applicable to all the empirical information found for T-junctions. For this reason, the numerical model presented herein is suitable for systems with a relatively large distance between two adjacent junctions (E, tube pitch).

5.3.1 Single-phase flow through an adiabatic horizontal manifold system

Wang and Yu [3] proposed a numerical model and reported experimental results for manifold systems working with single-phase water flow. The work was focused on studying the flow uniformity inside solar collectors and collector arrays. The experimental measurements were done in a manifold system of the reverse type as shown in Figure 5.1 (left). The geometric and operational conditions are presented in Table 5.2.

Geometric parameters	
Configuration	reverse
Manifolds orientation	horizontal
Tubes orientation	horizontal
Dividing manifold diameter	13 mm
Combining manifold diameter	13 mm
Parallel tubes diameter, D_t	6.5 mm
Number of parallel tubes, N	10
Length of parallel tubes, L_t	1.12 m
Tube pitch, E	0.03 m
Operational parameters	
External condition	adiabatic
Fluid	water
Flow type	single-phase flow
Inlet volumetric flow rate[a]	6.4 l/min

^{a} Information obtained from Jones and Lior [4].

Table 5.2: Manifold system conditions of Wang and Yu [3] experimental test.

In Figure 5.7, the experimental measurements of Wang and Yu [3] are compared against the numerical predictions of the present model. The dimensionless reference pressure ($\bar{p}_{ref}$) of the dividing manifold is calculated from its inlet pressure (node 1 in Figure 5.1) while for the combining manifold this value is calculated from its outlet pressure (node 2). In both cases $\bar{p}_{ref}$ is calculated with the manifold system inlet velocity (node 1). The manifold length is denoted as L_m, and z_m is the manifold position where the fluid dimensionless pressure $\bar{p}$ is measured and calculated. The dividing and combining T-junction models used in the simulation have been taken from Idelchik [12], while the heat transfer and the friction factor coefficients used in the two-phase flow model have been estimated with the correlations of Gnielinski [21] and Churchill [22], respectively.

The agreement shown in Figure 5.7 is notably good (the differences between all the experimental data and their corresponding prediction values are lower than 8%), considering that standard junction information has been used for the simulation. The numerical results allow to analyze the pressure evolution in both manifolds. It
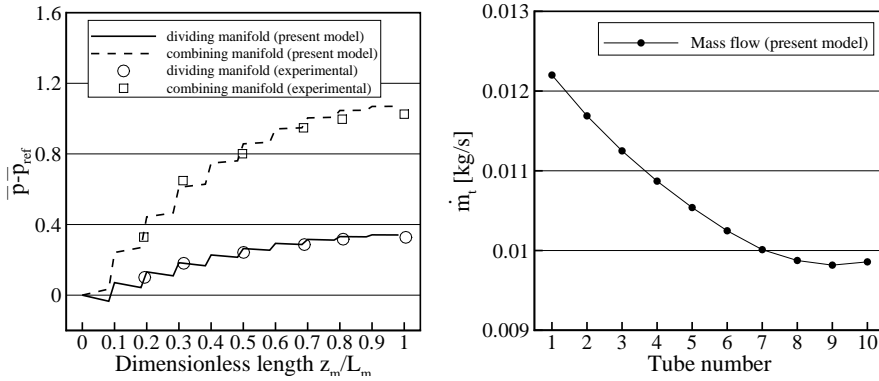
Figure 5.7: Numerical predictions vs. Wang and Yu [3] experimental data.

is interesting to observe how the main flow gains pressure throughout the dividing manifold. This phenomenon occurs because the pressure gains due to the sudden expansions of the main flow - when part of it is deviated through a parallel tube - are higher than the pressure losses due to friction along the manifold itself. Wang and Yu [3] stated that this behavior is characteristic of the pressure regain type manifold systems. However, on the combining manifold, according to the main flow direction, the T-junction effect observed is opposite. In this case the pressure losses due to friction along the manifold are added to the pressure losses due to the main flow contractions - when incoming flows from the parallel tubes are added to the main flow -.

An additional comparison was carried out between the present model and the numerical model of Wang and Yu [3]. In this case, the comparison is focused on a parametric study of the tube pitch (E) for two different manifold system configurations: reverse (Figure 5.8) and parallel (Figure 5.9). The conditions of the compared numerical cases are shown in Table 5.3.

Their numerical study reports different trends of the pressure evolution through the distribution manifold: the pressure increases for small intervals between tubes (the pressure gain due to the junction effect is higher than the pressure loss due to the friction along the manifold), while it decreases for larger intervals (the friction pressure loss along the manifold becomes higher than the pressure gain due to the junction effect). In both manifold system configurations, the distance between parallel tubes has a little influence in the pressure profile of the combining manifolds. Thus, as it is shown in both Figures, the mass flow distribution is significantly related to the distribution manifold pressure profile. According to the simulations, the most uniform
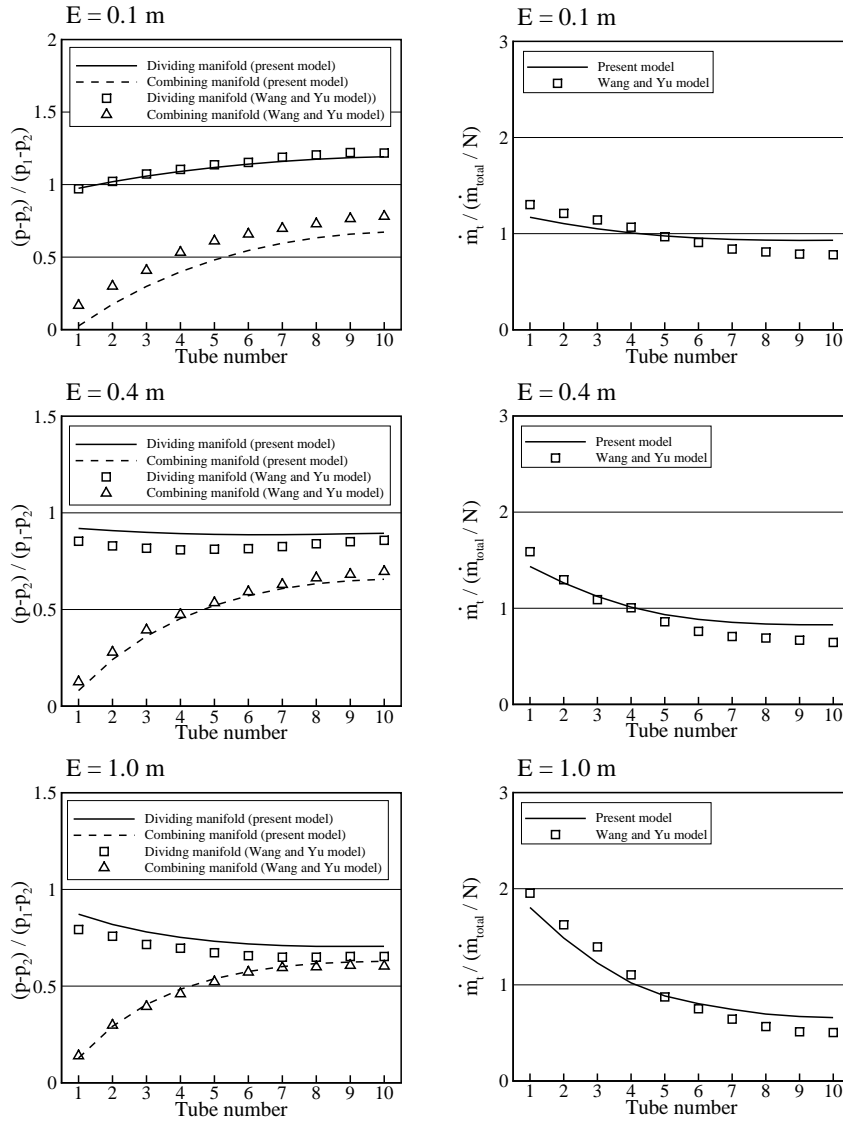
Figure 5.8: Present numerical model vs. Wang and Yu [3] model (reverse configuration). The manifold system inlet and outlet pressures are denoted as p_1 and p_2 respectively.
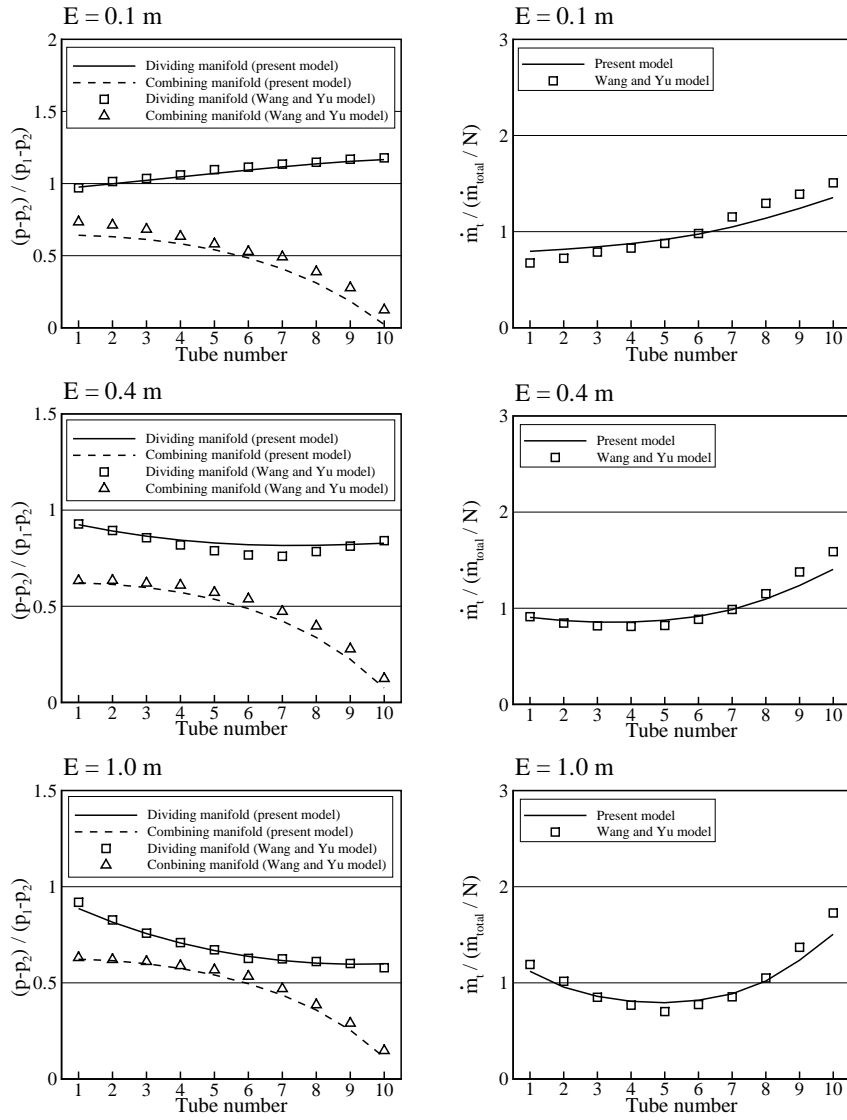
Figure 5.9: Present numerical model vs. Wang and Yu [3] model (parallel configuration). The manifold system inlet and outlet pressures are denoted as p_1 and p_2 respectively.

Geometrical parameters	
Configuration	parallel/reverse
Manifolds orientation	horizontal
Tubes orientation	horizontal
Dividing manifold diameter	25 mm
Combining manifold diameter	25 mm
Parallel tubes diameter, D_t	12.5 mm
Number of parallel tubes, N	10
Length of parallel tubes, L_t	3 m
Tube pitch, E	0.1/0.4/1.0 m
Operational parameters	
External condition	adiabatic
Fluid	water
Flow type	single-phase flow
Inlet mass flow rate, $\dot{m}$	1000 kg/h

Table 5.3: Manifold system conditions of Wang and Yu [3] numerical cases.

mass flow distribution has been obtained for both the reverse configuration and the smaller pitch (E = 0.1 m). A good agreement between the tendencies predicted with the present model and the model of Wang and Yu [3] is observed.

5.3.2 Two-phase flow through a non-adiabatic horizontal manifold system with upwardly oriented vertical channels

The experimental measurements of the manifold considered in this study have been taken from Sivert [23] where typical car air conditioning operating conditions and geometries were used. Sivert [23] presented a large number of experimental tests considering different refrigerants and a wide range of operational conditions.

The experimental facility was designed to simulate a car air conditioning evaporator of approximately 5 kW of capacity. The manifold was placed horizontally while the tubes were vertically upward oriented. The refrigerant used was carbon dioxide. In the experimental facility each parallel tube was heated by means of hot water flowing in counter-flow direction through a concentric annular tube. The validation study carried out in this section is based on the experimental conditions detailed in Table 5.4. The flow distribution predictions of the present model are compared against Sivert [23] experimental data in Figures 5.10, 5.11, 5.12 and 5.13.

In the numerical model, the manifolds are simulated as tubes with an insulation layer while the parallel tubes are simulated as double pipe counter flow heat exchangers. In the latter case, the secondary fluid and the external tube solid parts have been simulated based on the same numerical model presented in Section 5.2.3. For dividing T-junctions, the phase separation model of Seeger et al. [8] and the pressure model of Tae and Cho [11] have been used. For combining T-junctions, the pressure models

Geometric parameters	
Configuration	reverse
Manifolds orientation	horizontal
Tubes orientation	vertical upward
Dividing manifold diameter	16 mm
Parallel tubes diameter, D_t	4 mm
Parallel tubes annular tube diameter	8 mm
Number of parallel tubes, N	10
Length of parallel tubes, L_t	0.9 m
Tube pitch, E	0.021 m
Operational parameters	
External condition	non-adiabatic
Fluid	carbon dioxide
Flow type	two-phase flow
Manifold system inlet gas weight fraction, x_g	0.14/(0.28)/0.43/0.54
Inlet saturation temperature	18.7 $^\circ$C
Inlet counter-flow water temperature, T_{water}	30/(40)/50 $^\circ$C
Inlet counter-flow water mass flow rate	0.017 kg/s
Inlet mass flow rate, $\dot{m}$	0.033 kg/s

Table 5.4: Manifold system conditions of Sivert [23] experimental tests (reference case conditions in brackets).

Idelchik [12] and Schmidt and Loth [16] have been selected. The empirical correlations used in the two-phase flow model are listed as follows: i) in the case of single-phase flow, the same correlations as for the single-phase manifold system studied in the previous section are used (for both the carbon dioxide flowing through tubes and the water flowing through the annular tubes); ii) for two-phase flow, the correlations of Friedel [24] and Gungor and Winterton [25] are used to predict the friction factor and the heat transfer coefficient, respectively; and iii) the void fraction is calculated with the correlation of Premoli et al. [26]. The flow regime along the distribution manifold is predicted with the flow pattern map of Thome [17]. According to the map, the flow pattern predicted along the dividing manifold for all the simulated cases is of the stratified/stratified-wavy type.

Figure 5.10 shows both the inlet liquid and gas mass flow ratios of the parallel tubes at different distribution manifold inlet gas weight fractions. The evolution of the gas and liquid mass flow ratio profiles is very similar between the numerical predictions (Figure 5.10, left) and the experimental measurements (Figure 5.10, right). Due to the higher moment of inertia of the liquid phase and the vertical upward orientation of the tubes, the gas and the liquid phases are preferably deviated through the first and the last tubes, respectively. If the gas mass flow ratio profiles were depicted in the same area with the corresponding liquid mass flow ratio profiles, it could be noticed that for each test there is a tube in the manifold system from which the liquid mass flow ratio is greater than the gas mass flow ratio in all the subsequent tubes. This
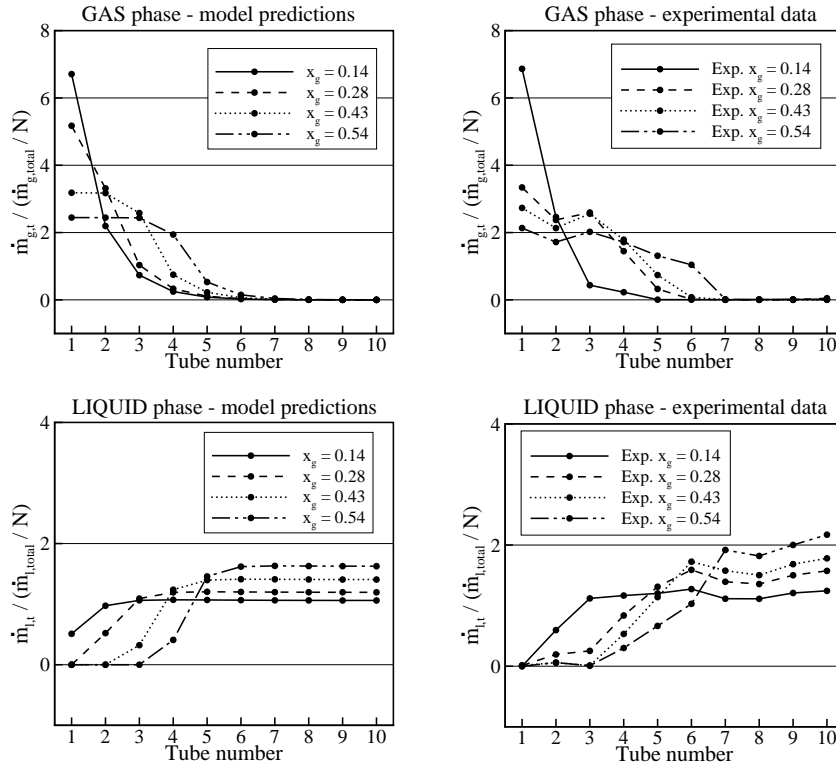
Figure 5.10: Phase distribution for different manifold system inlet gas weight fractions ($T_{water} = 40°C$). Model predictions (left) and experimental data from Sivert [23] (right).

tube position moves towards the manifold end as the manifold system inlet gas weight fraction increases. This behavior is observed in the model predictions as well as the experimental data.

In Figure 5.11 the heat exchanged by each tube at different distribution manifold inlet gas weight fractions is depicted. In this case, although the mean prediction error (Equation 2.57) of all the experimental points is significant (30%), the general trends of the experimental data are reasonably well predicted. The liquid mass flow ratio profile is closely related to the profile of the heat exchanged in tubes due to the heat transfer characteristics of the liquid phase (much higher heat transfer coefficient than the gas phase). Poor heat transfer is observed in tubes with low liquid mass flow
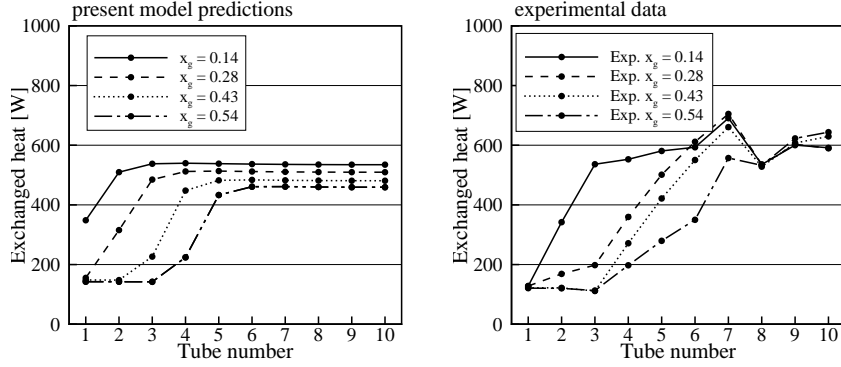
Figure 5.11: Heat exchanged for different manifold system inlet gas weight fractions ($T_{water} = 40°$C). Model predictions (left) and experimental data from Sivert [23] (right).

ratio. In fact, the liquid phase observed in tubes 1 to 4 is negligible for the case of $x_g = 0.54$ where most of the heat exchanged by the whole system is done by tubes 6 to 10. The less accurate prediction occurs for the case of $x_g = 0.28$ because its phase distribution was also less accurately predicted.
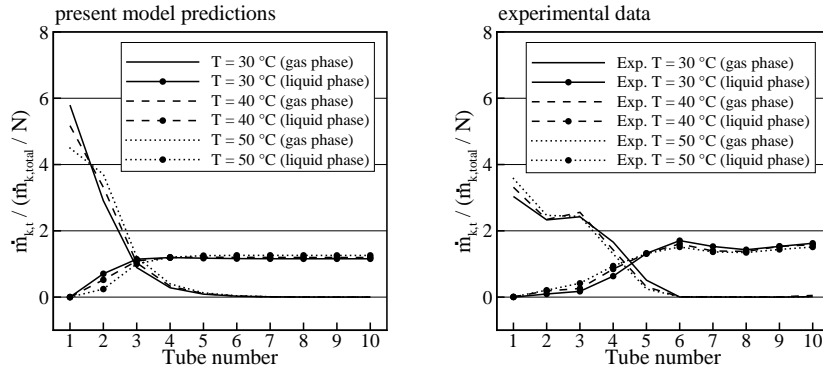

Figure 5.12: Phase distribution for different counter-flow water inlet temperatures ($x_g = 0.28$). Model predictions (left) and experimental data from Sivert [23] (right).

Figure 5.12 shows the influence of the double pipe secondary fluid inlet tempera-

ture in the phase distribution. In the model predictions as well as the experimental data, the mass flow ratio profiles are not affected when the heat load applied to tubes changes.
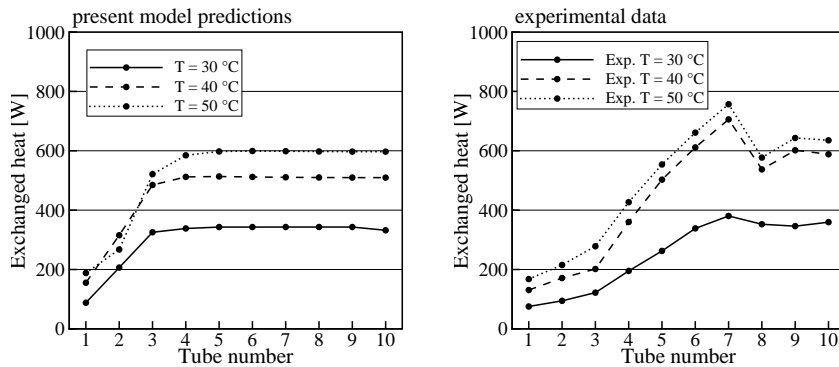

Figure 5.13: Heat exchanged for different counter-flow water inlet temperatures ($x_g = 0.28$). Model predictions (left) and experimental data from Sivert [23] (right).

Figure 5.13 shows the profile of the heat exchanged by the parallel tubes considering different heat loads. The mean prediction error is significant (32%) but the general trends of the experimental data of Sivert [23] are well predicted. The predicted heat profile slope between tubes number 1 and 4 is rather steep compared to the experimental cases where the corresponding slope goes between tubes number 3 to 6. This discrepancy is closely related to the differences between the numerical and the experimental liquid mass flow ratio profiles of Figure 5.12.

The mean prediction error of the simulated cases is significant due to the high level of empiricism used by the model and the limiting conditions of the correlations. However, a qualitative agreement between the obtained numerical predictions and the experimental data has been observed. The general trends of the simulated cases (mass flow distribution, exchanged heat profile, etc.) has been well predicted by both the T-junction models and the fluid flow model. Thus, both models were successfully coupled in the global flow distribution algorithm.

5.4 Parametric studies on two-phase flow manifolds

In order to show the possibilities of the two-phase flow numerical distribution model two parametric studies have been carried out. Firstly, an extensive parametric study on a manifold system working with R134a and secondly, the two-phase flow evaporator

validated in Section 5.3.2 is studied at two different orientations (horizontal manifold with horizontal tubes and horizontal manifold with upwardly oriented tubes).

5.4.1 Two-phase flow distribution in a non-adiabatic manifold system working with R-134a

The numerical parametric study has been carried out for a manifold system working with R-134a (see Figure 5.1). Different geometric conditions (e.g. number of parallel tubes, manifold diameters) and operational conditions (e.g. inlet mass velocity, inlet gas weight fraction) have been studied as shown in Table 5.5. The numerical results are reported in Figures 5.14 to 5.22 where the manifold pressure profiles, the manifold system mass flow distribution and the inlet gas weight fraction of each parallel tube are plotted.

Geometric parameters	
Configuration	**reverse**/parallel
Manifolds orientation	horizontal
Tubes orientation	horizontal
Dividing manifold diameter	12 mm
Combining manifold diameter	**12**/15/18 mm
Parallel tubes diameter, D_t	8/**11** mm
Number of parallel tubes, N	4/5/**6**
Length of parallel tubes, L_t	1/**2**/3 m
Tube pitch, E	0.2 m
Operational parameters	
External condition	non-adiabatic
Fluid	R-134a
Flow type	two-phase flow
Manifold inlet gas weight fraction, x_g	**0.4**/0.5/0.6
Manifold inlet saturation temperature	5 $^\circ$C
Inlet mass velocity, G	300/500/**750** kg/m^2s
Heat flux on parallel tubes, $\dot{q}$	10000 W/m^2

Table 5.5: Manifold conditions for the numerical parametric study of a non-adiabatic manifold system working with R-134a (reference conditions in bold).

In order to highlight the importance of the dividing T-junctions effect on the manifold system, two different numerical cases have been compared in Figure 5.14. The first case includes the dividing T-junction correlations to predict both the pressure change and phase split, while the second case does not include any T-junction correlation. The results are completely different. In fact, important effects such as the pressure increase along the dividing manifold due to the sudden flow expansion at each junction (see the dividing manifold pressure profiles) and the uneven phase split at each dividing junction (see the inlet gas weight fractions of parallel tubes) are
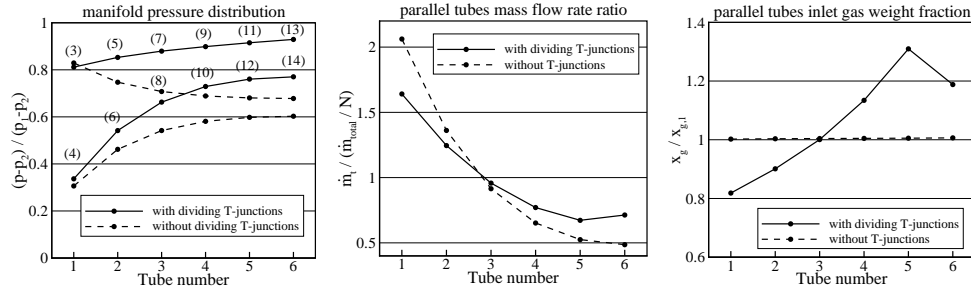
Figure 5.14: Numerical predictions with and without the dividing T-junction correlations (manifold node positions in brackets).

not simulated/predicted when the correlations are not considered. The lack of these effects leads to a clearly unacceptable prediction.
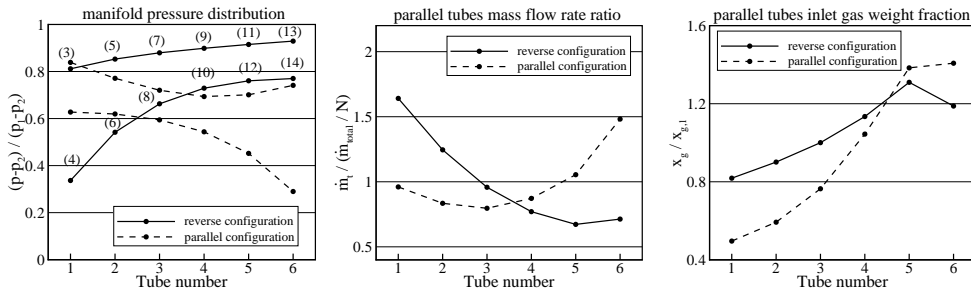

Figure 5.15: Numerical predictions for parallel and reverse configurations (manifold node positions in brackets).

In Figure 5.15 the reverse and the parallel configurations are compared. As expected, the combining manifold pressure profile of the parallel configuration is opposite to that of the reverse configuration due to the flow direction. However, the pressure along the whole dividing manifold of the reverse configuration raises but the pressure through the dividing manifold of the parallel configuration decreases and then raises. In the latter case, the pressure gain due to the main flow sudden expansion is lower at the first junctions of the dividing manifold because less mass flow is deviated through the first tubes. In both configurations the parallel tubes inlet gas weight fraction is lower at the first tubes (this phenomenon is more noticeable in the parallel configuration).
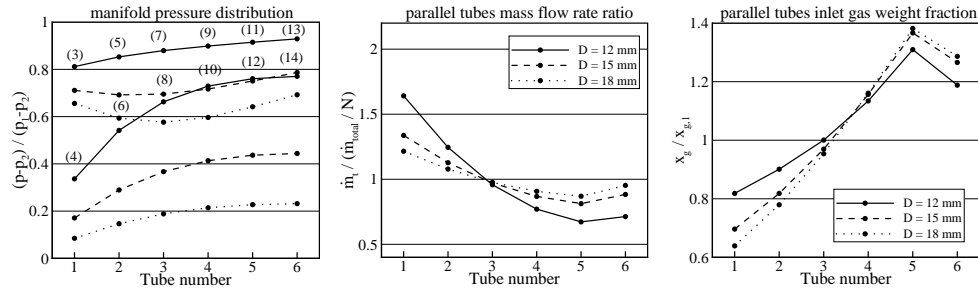
Figure 5.16: Numerical predictions for different combining manifold diameters (manifold node positions in brackets).

The effect of the combining manifold diameter is observed in Figure 5.16. It is noticed that as the combining manifold diameter increases its pressure profile is flattenned because the friction losses through it are less accentuated. Thus, the mass flow distribution in the parallel tubes becomes more uniform. The pressure profile of the dividing manifold also changes significantly: it increases along the whole dividing manifold for small combining manifold diameters (12 *mm*) while it decreases along the first three nodes and then increases through the last nodes for larger combining manifold diameters (15 and 18 *mm*). In the latter cases, the dividing manifold pressure decrease at the first two dividing T-junctions occurs because the main flow pressure raise due to the sudden expansion at the first two dividing T-junctions is not large enough to exceed the pressure losses through the dividing manifold itself (the mass deviated through the first two parallel tubes is relatively small).
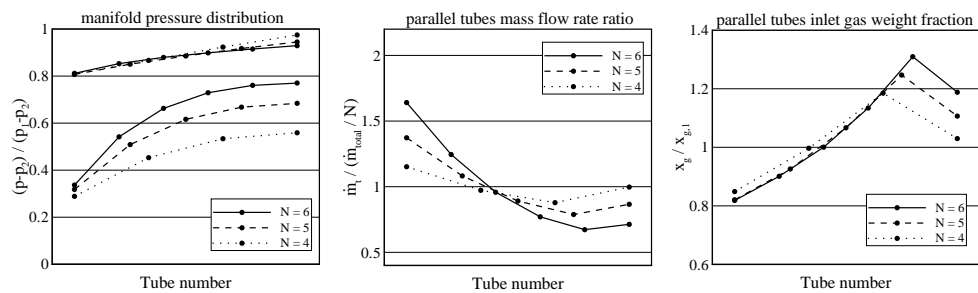
Figure 5.17: Numerical predictions for different number of parallel tubes.

The influence of the number of parallel tubes in the studied manifold system

is shown in Figure 5.17 (the total mass flow rate has been kept constant). The same general trends of the pressure distribution along the dividing and the combining manifolds are observed for all the cases (N = 4, 5 and 6). The pressure loss along the combining manifold is lower when less tubes are considered because its length is proportionally reduced.
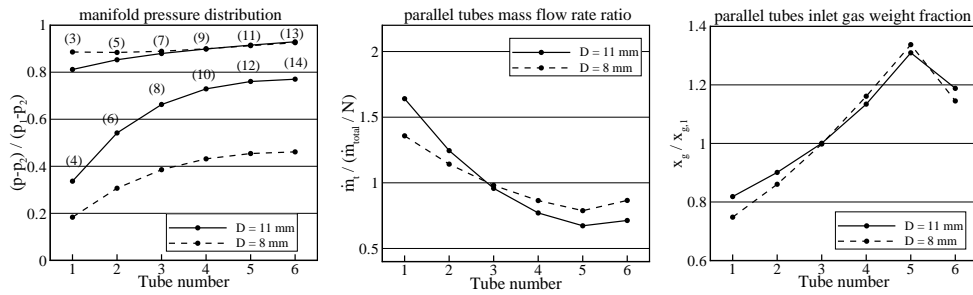

Figure 5.18: Numerical predictions for different parallel tubes diameters (manifold node positions in brackets).

Figure 5.18 shows the influence of the parallel tubes diameter. The global pressure leap between the dividing and combining manifolds is greater for the case with smaller parallel tube diameter (8 *mm*) than for the case with larger parallel tube diameter (11 *mm*) because the friction losses that the flow must overcome are comparatively lower. When the pressure loss through the parallel tubes increases, the influence of the dividing and the combining manifold pressure profiles becomes less notorious and the mass flow is more uniformly distributed.
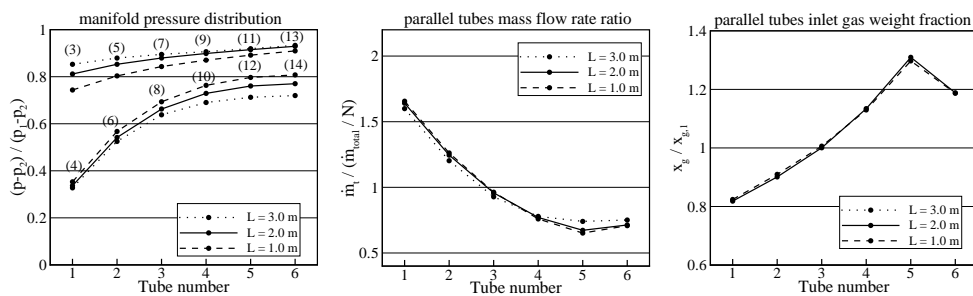

Figure 5.19: Numerical predictions for different parallel tubes lengths (manifold node positions in brackets).

Figure 5.19 depicts the numerical predictions where the influence of the parallel tubes length is studied. It is noticed that almost no significant changes occur in both the mass flow distribution and the phase split at the three simulated lengths (1, 2 and 3 m). The pressure difference between the dividing and the combining manifold nodes increases as the parallel tubes length increases. This is mainly due to the additional friction losses when the length of tubes is increased.
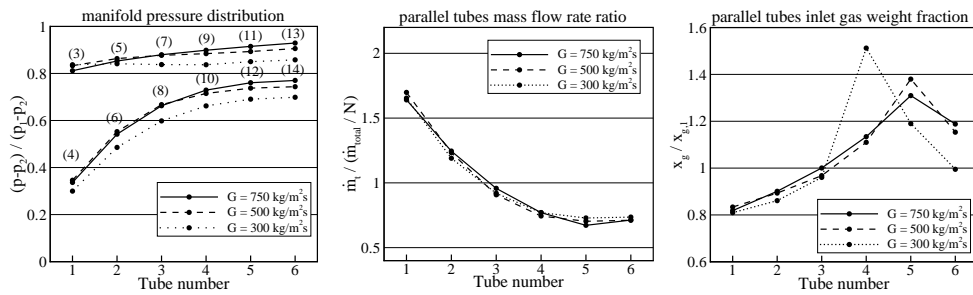

Figure 5.20: Numerical predictions for different manifold system inlet mass velocities (manifold node positions in brackets).
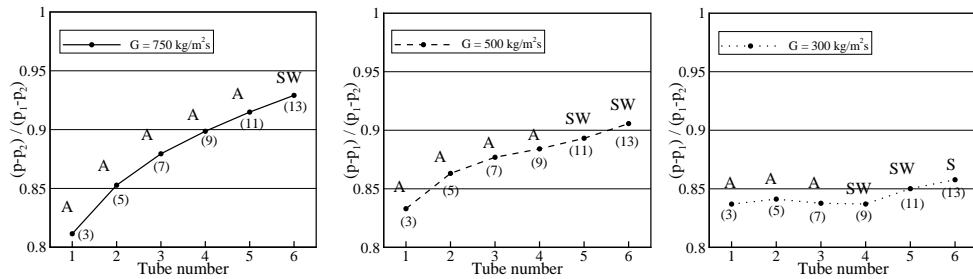
Figure 5.21: Flow pattern of the dividing manifold T-junctions incoming flow for different manifold system inlet mass velocities. Nomenclature: A, annular, SW, stratified-wavy and S, stratified (manifold node positions in brackets).

The influence of the manifold system inlet mass velocity is shown in Figure 5.20. Both the dividing and combining manifold pressure profiles are similar for the three cases studied (750, 500 and 300 kg/m^2s). No significant difference is observed for the mass flow distribution through the parallel tubes of the manifold system. However, the parallel tubes inlet gas weight fraction profile for the lower mass velocity case

($300 \ kg/m^2s$) is considerably different from the other two cases. This abrupt change is directly related to the flow pattern of the incoming flow in the dividing T-junctions as shown in Figure 5.21.

The numerical simulations of the manifold system for different inlet gas weight fractions are plotted in Figure 5.22. This flow condition has little influence in both the mass flow distribution and the phase split at dividing junctions. When larger inlet gas weight fractions are considered the dividing manifold pressure profile slope increases while the pressure profile of the combining manifold remains very similar but with an increased pressure level.

Figure 5.22: Numerical predictions for different manifold system inlet gas weight fractions (manifold node positions in brackets).
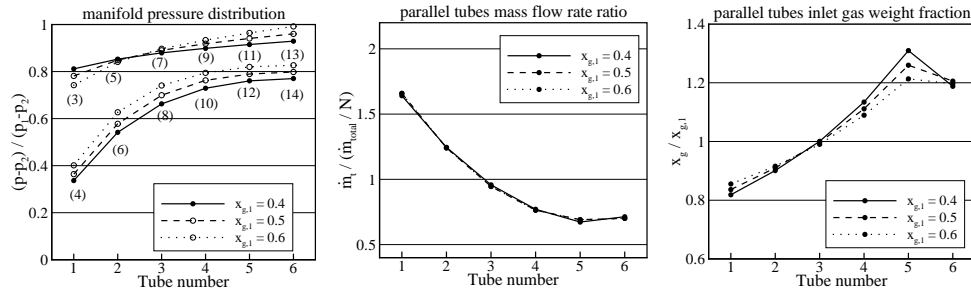
5.4.2 Two-phase flow distribution in a carbon dioxide manifold system at two different orientations

The two-phase flow manifold system with upwardly oriented parallel tubes (H-VU) that was validated in Section 5.3.2 has been simulated for a different orientation: horizontal manifold with horizontal parallel tubes (H-H). Both cases are compared in order to see the orientation influence. In the horizontal case (H-H), the phase separation in dividing T-junctions is simulated with the model of Tae and Cho [11] which consists in an extended version of the Hwang et al. [9] model. It can be used for horizontal junctions with diameter reduction but requires specific geometric relationships depending on the flow regime. According to the flow pattern map of Thome [17], the flow regime through the dividing manifold of the cases simulated in this section was of the type stratified/stratified-wavy. Therefore, the corresponding geometric relationships have been derived for this study (see Appendix A). The results are presented in Figures 5.23, 5.24 and 5.25 where a numerical comparison between both configurations is carried out as no experimental data were available for the

horizontal configuration (H-H). The flow conditions are the same of the reference case studied in Section 5.3.2 and detailed in Table 5.4 (x_g=0.28 and inlet counter-flow water temperature of 40 °C).
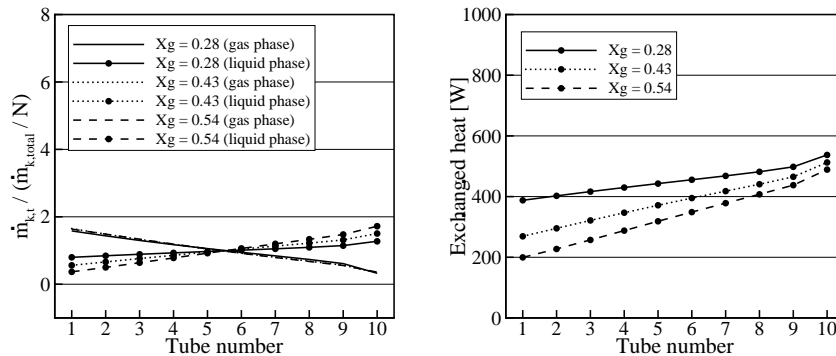

Figure 5.23: Model predictions for horizontal manifold with horizontal oriented tubes at different inlet gas weight fractions. Phase distribution (left) and heat exchanged by tubes (right).

Figure 5.23 (left) shows both the inlet liquid and gas mass flow ratios of the H-H manifold system parallel tubes for different dividing manifold inlet gas weight fractions. For all the considered gas weight fractions, the gas mass flow ratio is greater than the liquid mass flow ratio at the entrance of the first five tubes, while the opposite situation occurs in the last five tubes. The liquid mass flow ratio increases linearly between tubes number 1 to 10, while the gas mass flow ratio decreases linearly. In fact, the slope of the liquid mass flow ratio profile gently increases as the manifold inlet gas weight fraction increases, but the gas mass flow ratio profile slope remains almost equal. This situation is completely different for the H-VU manifold where both the gas and liquid mass flow ratio profiles present steeper variations (Figure 5.10, left). Thus, the studied parameter has little influence in the H-H manifold phase distribution in contrast to the H-VU orientation. Figure 5.23 (right) shows the heat exchanged by each tube in the H-H manifold system. The heat exchanged increases progressively from tube 1 to 10 due to the increasing linear tendency of the liquid mass flow ratio profile.

Both the manifold pressure profiles and the mass flow rate distribution of the reference manifold system are studied in Figure 5.24. The left graph shows that the dividing and combining manifold pressure profiles for both the H-H and the H-VU manifold systems are similar, however, the right graph shows a very unequal mass
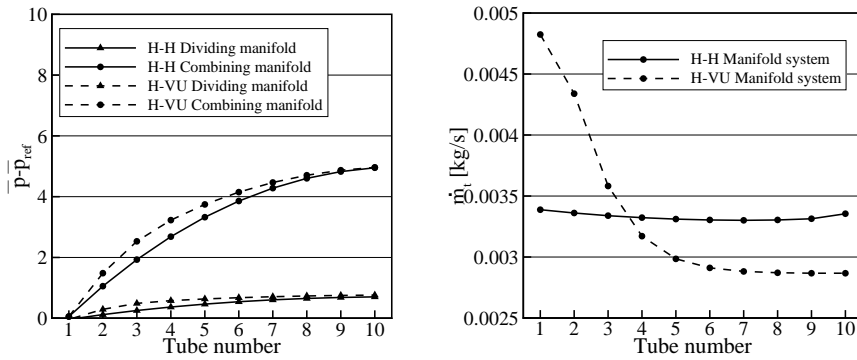
Figure 5.24: Manifold pressure profiles (left) and parallel tube mass flows (right) for manifold system at two orientations (H-H and H-VU).

flow distribution between both configurations. The H-H manifold presents a more uniform distribution because the liquid and gas phases are more evenly distributed.
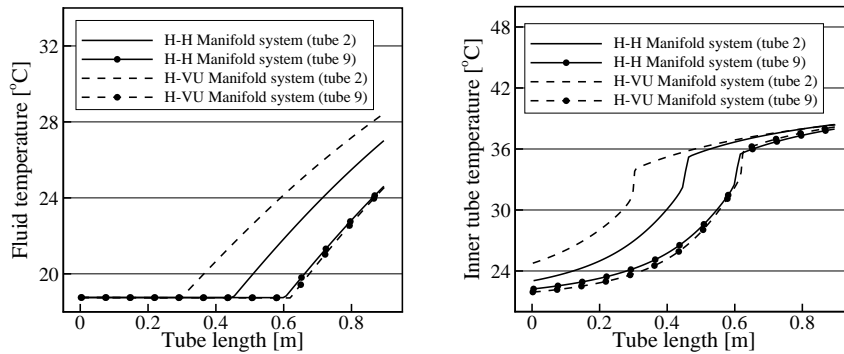
Figure 5.25: Fluid (left) and inner tube temperature evolution (right) along representative tubes of both manifold systems (H-H and H-VU).

The differences between both orientations are also seen in Figure 5.25 where the fluid temperature and the inner tube temperature evolution along tubes are plotted for the reference case. In fact, only two representative tubes are studied: one from the first part of the manifold (tube number 2), and the other from the last part of

the manifold (tube number 9). It can be observed that the thermal behavior of tube number 9 is similar for both configurations (single-phase starts at 0.6 m). This is not the case for tube number 2, where the single-phase flow condition starts at 0.3 m and 0.45 m for the H-VU and H-H manifold systems, respectively. Consequently, in both cases more heat is transferred by tube number 9 due to its longer lasting two-phase flow condition. However, the fluid temperature profile difference between tubes number 2 and 9 is greater for the H-VU manifold system due to the more significant gas phase predominance in its first tubes. This is directly related to the tube temperature evolution as seen in Figure 5.25 (right).

In both configurations, H-H and H-VU, the heat transferred by the last tubes is greater compared to the first tubes. However, the corresponding heat transfer profiles are very different as shown in Figures 5.13 (right) and 5.23 (right). This is mainly due to the flow distribution which is more uniform in the H-H manifold system.

5.5 Conclusions

A numerical model for predicting the flow distribution in multiple parallel tubes have been detailed and successfully validated. The simulations have been carried out for different manifold systems and considering a wide variety of aspects: i) single-phase and two-phase flows; ii) reverse and parallel manifold system arrangements; ii) horizontal manifolds with both horizontal and upward oriented parallel tubes; iv) different operating conditions (inlet mass flow rate, inlet weight fraction, etc.); v) different geometric sizes; and vi) different heat loads on the parallel tubes. The numerical model shows good qualitative agreement against experimental data as the effects of the studied parameters are well predicted. The model accuracy depends on the availability and appropriate selection of T-junction models as well as the manifold geometry which must be adequate to be represented by means of tubes and junctions. The numerical results presented in the last section allow to show the capabilities and level of detail of the developed model.

Nomenclature

A	area, m^2
a	distance of dividing streamline, m
C	coefficient of two-phase multiplier for T-junction
COP	coefficient of performance
D	tube diameter, m
d	relation among correction pressure and correction flow
E	tube pitch, m
e	specific energy, $J \cdot kg^{-1}$

F	extraction rate
$F_{<\rho v^3>i}$	steamline correction factor
G	mass velocity, $kg \cdot m^{-2} \cdot s^{-1}$
g	acceleration due to gravity, $m \cdot s^{-2}$
h	specific enthalpy, $J \cdot kg^{-1}$
K	single-phase friction loss coefficient
$k_{c,ij}$	contraction coefficient
L	length, m
$\dot{m}$	mass flow rate, $kg \cdot s^{-1}$
$\dot{m}_{total}$	manifold system inlet mass flow rate, $kg \cdot s^{-1}$
N	number of parallel tubes
p	pressure, Pa
$\bar{p}$	dimensionless pressure, $p \cdot \rho^{-1} \cdot v_{m,in}^{-2}$
$\dot{q}$	heat flux, $W \cdot m^{-2}$
R	radius of curvature, m
S	cross section, m^2
T	temperature, K
v	velocity, $m \cdot s^{-1}$
v_{sg}	gas superficial velocity, $m \cdot s^{-1}$
v_{sl}	liquid superficial velocity, $m \cdot s^{-1}$
X	Lockart-Martinelli parameter
x_g	gas weight fraction
z	axial position, m

Greek symbols

Δp	pressure change, Pa, ($\Delta p_{i-j} = p_j - p_i$)
Δp_{ad}	additional pressure change, Pa
Δz	axial step, m
ϵ_g	gas void fraction
ξ	flow resistance coefficient, convergence accuracy criterion
θ	inclination angle, rad
λ	thermal conductivity, $W \cdot m^{-1} \cdot K^{-1}$
ρ	density, $kg \cdot m^{-3}$
τ	shear stress, Pa
ϕ	discretized variable

Subscripts

c	kinetic

d	destination
exp	experimental
ext	external
g	gas phase
i	grid position
irr	irreversible
k	phase (gas or liquid)
l	liquid phase
m	manifold
num	numerical
o	origin
p	potential
ref	reference
rev	reversible
t	parallel tube

References

[1] M. Watanabe, M. Katsuta, and K. Nagata. General characteristics of two-phase flow distribution in a multipass tube. *Heat Transfer - Japanese Research*, 24(1):32–44, 1995.

[2] R. A. Bajura and E. H. Jones Jr. Flow distribution manifolds. *Journal of Fluids Engineering*, 98:654–665, 1976.

[3] X. A. Wang and P. Yu. Isothermal flow distribution in header systems. *International Journal of Solar Energy*, 7:159–169, 1989.

[4] G. F. Jones and N. Lior. Flow distribution in manifolded solar collectors with negligible buoyancy effects. *Solar Energy*, 52(3):289–300, 1972.

[5] A. C. Mueller and J. P. Chiou. Review of various types of flow maldistribution in heat exchangers. *Heat Transfer Engineering*, 9(2):36–50, 1988.

[6] Y. Hwang, D. H. Jin, and R. Radermacher. Refrigeration distribution in minichannel evaporator manifold. *HVAC and Research*, 13(4):543–555, 2007.

[7] A. Marchitto, F. Devia, M. Fossa, G. Guglielmini, and C. Schenone. Experiments on two-phase flow distribution inside parallel channels of compact heat exchangers. *International Journal of Multiphase Flow*, 34:128–144, 2008.

[8] W. Seeger, J. Reimann, and U. Muller. Two-phase flow in a T-junction with a horizontal inlet, Part I: phase separation. *International Journal of Multiphase Flow*, 12(4):575–585, 1986.

[9] S. T. Hwang, H. M. Soliman, and R. T. Lahey Jr. Phase separation in dividing two-phase flows. *International Journal of Multiphase Flow*, 14(4):439–458, 1988.

[10] F. Marti and O. Shoham. A unified model for stratified-wavy two-phase flow splitting at a reduced T-junction with an inclined branch arm. *International Journal of Multiphase Flow*, 23(4):725–748, 1997.

[11] S. Tae and K. Cho. Two-phase split of refrigerants at T-junction. *International Journal of Refrigeration*, 29(7):1128–1137, 2006.

[12] I. E. Idelchik. *Handbook of hydraulic resistance*. CRC Press, 1994.

[13] J. R. Buell, H. M. Soliman, and G. E. Sims. Two-phase pressure drop and phase distribution at a horizontal tee junction. *International Journal of Multiphase Flow*, 20(5):819–836, 1994.

[14] A. Gardel. Pressure drops in flows through t-shaped pipefittings. *Bull. Tech Suisse Romande*, 9:122–130, 1957.

[15] D. Chisholm and L. A. Sutherland. Prediction of pressure gradients in pipeline systems during two-phase flow. In *Proceedings of the Symposium on Fluid Mechanics and Measurements in Two-Phase Flow Systems*, 1969.

[16] H. Schmidt and R. Loth. Predictive methods for two-phase flow pressure loss in tee junctions with combining conduits. *International Journal of Multiphase Flow*, 20(4):703–720, 1994.

[17] J. R. Thome. Update on advances in flow pattern based two-phase heat transfer models. *Exp. Thermal and Fluid Science*, 29(3):341–349, 2005.

[18] N. Saba and R.T. Lahey Jr. The analysis of phase separation in branching conduits. *International Journal of Multiphase Flow*, 10(1):1–20, 1984.

[19] S. V. Patankar. *Numerical heat transfer and fluid flow*. McGraw-Hill, New York, 1980.

[20] C. Oliet. *Numerical simulation and experimental validation of fin-and-tube heat exchangers*. PhD thesis, Universitat Politècnica de Catalunya, 2006.

[21] V. Gnielinski. New equations for heat and mass transfer in turbulent pipe and channel flow. *International Chemical Engineering*, 16(2):359–368, 1976.

[22] S. W. Churchill. Frictional equation spans all fluid flow regimes. *Chemical Engineering*, 84(24):91–92, 1977.

[23] V. Sivert. *Two-phase flow distribution in heat exchanger manifolds*. PhD thesis, Norwegian University of Science and Technology, 2003.

[24] L. Friedel. Improved friction pressure drop correlation for horizontal and vertical two-phase pipe flow. In *Proceedings of the European Two-Phase Flow Group Meeting*, 1979.

[25] K. E. Gungor and R. H. S. Winterton. Simplified general correlation for saturated flow boiling and comparisons of correlations with data. *Chemical Engineering Research and Design*, 65(2):148–156, 1987.

[26] A. Premoli, D. Francesco, and A. Prima. An empirical correlation for evaluating two-phase mixture density under adiabatic conditions. In *Proceedings of the European Two-Phase Flow Group Meeting*, 1970.

Chapter 6

Transcritical Vapor Compression Refrigerating Cycles Working with R-744

ABSTRACT

In this chapter a numerical model to simulate single-stage vapor compression refrigerating cycles is presented. The cycle resolution procedure is based on a successive substitution method. The numerical subroutines that solve all the cycle elements (heat exchangers, tubes, compressor and expansion device) are called sequentially, transferring adequate information to each other until convergence is reached. The results are focused on carbon dioxide transcritical vapor compression cycles with the aim of showing the possibilities that this refrigerant offers for commercial refrigeration. The main aspect studied in this chapter is the effect of adding an internal heat exchanger (IHE) to the basic single-stage cycle.

In the first section of this chapter, the main aspects of the transcritical carbon dioxide refrigerating cycle together with the advantages/consequences of adding an internal heat exchanger are briefly exposed. In the second section, the experimental facilities built in the CTTC, specially designed to study transcritical cycles working with carbon dioxide, are described. In the third section, the refrigerating cycle numerical model is detailed. The specific numerical model of each element (heat exchangers, tubes, compressor and expansion device) is presented together with the global cycle resolution procedure algorithm. The fourth section is devoted to the model validation. The numerical model is compared against experimental data collected from the CTTC facilities considering both situations (with and without internal heat exchange). Two additional studies are presented in the fifth section: i) an experimental illustrative comparison between R-134a subcritical cycles against carbon dioxide transcritical cycles; and ii) a numerical analysis of the IHE length influence in transcritical cycles.

Finally, concluding remarks are given in the last section. The main contents of this chapter are published in the *International Journal of Refrigeration.*

6.1 Introduction

Recent research studies state that carbon dioxide is a suitable refrigerant for air conditioning systems, heat pump water heaters, and some refrigeration units [1]. For such applications, most of the carbon dioxide single-stage vapor compression systems work under transcritical conditions due to the particularly low critical temperature of this refrigerant (31.1°C). In a typical transcritical cycle, the heat absorption takes place below the critical point and the heat rejection takes place above it, as shown in Figure 6.1. The device where heat is transferred to the ambient is known as the gas-cooler because the refrigerant fluid remains in single-phase.
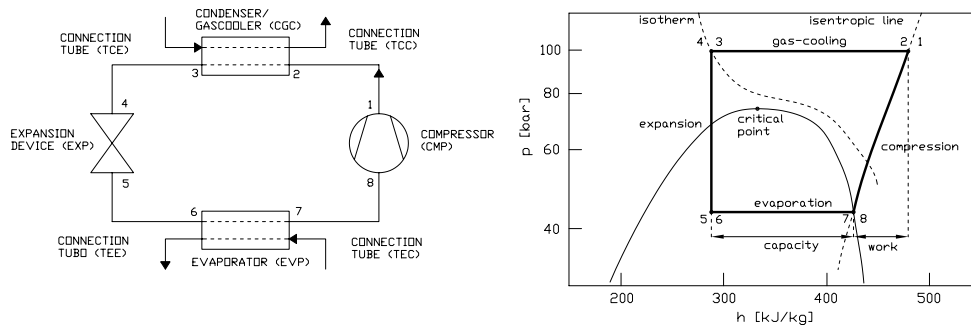

Figure 6.1: Transcritical cycle. Schematic diagram (left) and pressure vs. enthalpy evolution (right).

Figure 6.1 presents a thermodynamic cycle consisting in: an isobaric gascooling process (2-3), an isenthalpic expansion process (4-5), an isobaric evaporation process (6-7), an isentropic compression (8-1), and neglecting the pressure drop and heat losses in all the connection pipelines (1-2/3-4/5-6/7-8). For a fixed gas-cooler outlet temperature (3) it is noticed that an increase of the cycle gas-cooler pressure will result in higher compression work but better refrigeration capacity. However, due to the S-shaped transcritical isotherms, the coefficient of performance (COP), which is defined as the refrigeration capacity divided by the work consumption, can be maximized by adjusting the gas-cooler pressure. In subcritical cycles, considering similar conditions, the COP tends to decrease when the condenser pressure is increased.

In general, the heat transfer characteristics of carbon dioxide are better than those of halocarbons. In fact, for similar heat exchanger designs, the refrigerant evaporation temperature of transcritical units working with carbon dioxide is closer to the heat source temperature than for subcritical systems working with halocarbons, and similarly, the outlet refrigerant temperature of the gas-cooler is closer to the heat

sink temperature than the corresponding condensing temperature of halocarbons. However, from a thermodynamic comparison between a carbon dioxide transcritical cycle and a R-22 subcritical cycle, assuming that the refrigerant outlet temperature of the gas-cooler in the transcritical cycle equals to the condensing temperature of the conventional cycle, it is concluded that the transcritical cycle efficiency is lower [2]. Thus, in order to enhance the transcritical cycle efficiency several solutions have been proposed, namely expansion with work recovery, vortex tube expansion, ejector expansion, two-stage compression cycle, thermoelectric subcooler, and internal heat exchange cycle [1, 3].
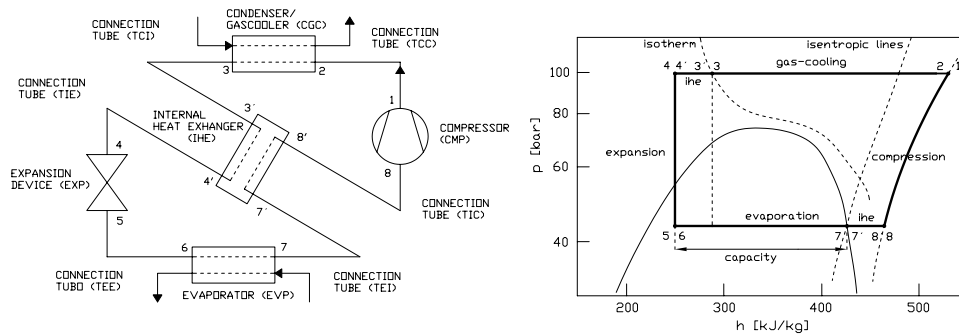

Figure 6.2: Transcritical cycle with an internal heat exchanger. Schematic diagram (left) and pressure vs. enthalpy evolution (right).

The highest efficiency improvement of the basic single-stage cycle is achieved by replacing the expansion device with a work recovery machine. However, such machines are costly compared to the use of an internal heat exchanger, which has no moving parts. Figure 6.2 depicts the main components of a transcritical cycle with an internal heat exchanger (IHE) and the related pressure vs. enthalpy diagram. These systems include an additional heat exchanger that transfers energy from the liquid line (3-4) to the suction line (7-8).

From a thermodynamic analysis the addition of an IHE allows: i) to initiate the evaporation process at a lower gas weight fraction with its obvious advantages due to the higher carbon dioxide heat transfer coefficient at two-phase conditions; and ii) to enlarge the enthalpy difference between the inlet and outlet evaporator cross sections, which helps to increase the COP of the system. Nevertheless, the addition of an IHE results on higher gas inlet compressor temperature which reduces the volumetric and isentropic mechanical efficiencies, and consequently reduces the system mass flow rate and increases the compressor specific work. Then, the addition of an IHE is a compromise between higher enthalpy difference in the evaporation process (cooling

capacity) and both mass flow reduction and power consumption increase.

In general, the efficiency benefits of including an IHE are more significant for transcritical cycles than for subcritical cycles. However, these devices are commonly used in subcritical systems for protective purposes, as they prevent flash gas at the expansion device and they ensure single-phase vapor to the compressor.

Different thermodynamic analysis, experimental works and simulation models have been presented in the literature in order to fully understand the influence of an IHE. In the later years, special emphasis has been put in studying the capabilities of carbon dioxide transcritical cycles with an IHE.

Domanski and Didion [4] carried out an extensive theoretical analysis about the internal heat exchanger influence in subcritical cycles. More than 25 refrigerants were evaluated and compared. It was concluded that the benefit of internal heat exchange was mainly due to the operating conditions and fluid properties (heat capacity, latent heat and coefficient of thermal expansion). It was shown that, for refrigerants with good performance in the basic cycle, internal heat exchangers may have a marginal - positive or negative - effect on cycle performance. The more significant improvements in cycle efficiency were reported for fluids with poor performance in the basic cycle.

Robinson and Groll [5] conducted an efficiency study of both a transcritical carbon dioxide cycle with internal heat exchange and an equivalent subcritical R-22 conventional cycle. Two thermodynamic numerical models, one with an expansion device and the other with a work recovery turbine, were developed. The simulations were carried out considering a heat source temperature from -35 to 10 $^{\circ}C$ (the refrigerant evaporation temperatures were assumed to be 5 $^{\circ}C$ higher). The sink source temperature was fixed at 35 $^{\circ}C$, hence the outlet gas-cooler temperature of the carbon dioxide transcritical cycle was assumed to be 40 $^{\circ}C$, and the condensation temperature of the subcritical R-22 cycle was assumed to be 50 $^{\circ}C$. The results showed that, depending on the evaporation temperature, the COP of carbon dioxide systems with IHE is about 72-118% of the COP of a conventional R-22 vapor compression cycle. It was also shown that the use of an internal heat exchanger in conjunction with an expansion valve increases the transcritical cycle COP by up to 7%.

Boewe et al. [6] carried out some experimental measurements for carbon dioxide air conditioning transcritical cycles with internal heat exchange. Their experimental tests were obtained for different IHE lengths (1.0, 1.5 and 2.0 m), at different compressor speeds (950 and 1800 rpm), at different heat sink temperatures (32.2 and 43.3 $^{\circ}C$), and for a heat source temperature of 26.7 $^{\circ}C$. The results showed that the use of an internal heat exchanger increases the system efficiency up to 25% for high ambient temperatures and up to 13% for low ambient temperatures. In the same work, a numerical model was developed and used for finding a convenient IHE geometry, by optimizing the trade-off between the IHE effectiveness and the suction pressure drop, in order to improve the system COP. The simulations showed that a cycle effectiveness

increase of 10% could be obtained with an IHE and with a material requirements reduction of 50%.

Kim et al. [7] investigated the performance of a transcritical carbon dioxide cycle with internal heat exchange for hot water heating. In their experimental data different IHE lengths were considered (0.0, 1.5, 3.0 and 4.5 m), the inlet temperature of the heat source ranged from 10 to 26.5 $^\circ C$, the inlet temperature of the heat sink ranged from 10 to 40 $^\circ C$, the discharge pressure ranged from 7.5 to 12 MPa, and a superheat of 5 $^\circ C$ was defined. From their experimental data, and by means of a simulation model, they concluded that, as the internal heat exchanger length increases, the compressor power consumption decreases as well as both the mass flow rate of the refrigerant and the COP optimum discharge pressure. They also observed an improved cycle COP when using internal heat exchange but only up to a certain discharge pressure.

Aprea and Maiorino [8] carried out an experimental study for residential air-conditioning carbon dioxide systems with and without the use of an internal heat exchanger. The basic cycle included a liquid receiver and a suction buffer. The gas-cooler and the evaporator were finned tube heat exchangers while the IHE was a double tube heat exchanger. The tests were obtained at ambient temperatures ranging from 25 to 40 $^\circ C$ and for an evaporation temperature of 5 $^\circ C$. The results showed that the COP increases up to 10% when the internal heat exchanger was used.

The aim of the work presented in this chapter is the development of a numerical model to predict the thermal and fluid-dynamic behavior of carbon dioxide transcritical refrigerating cycles with and without internal heat exchange, and study their performance for small capacity refrigeration applications. In the following section of the present chapter, the experimental facilities built to study transcritical carbon dioxide refrigerating systems are described, including its main elements and sensors. In the third section, the numerical models used to simulate each element of the cycle (heat exchangers, tubes, compressor and expansion device) are detailed, as well as the main resolution procedure for the whole refrigerating cycle. In the fourth section, the model is extensively validated against data collected from the experimental units: i) an extensive validation of the transcritical cycle (without IHE) and its components is carried out; ii) two different compressor prototypes are tested on a transcritical cycle without internal heat exchange; and iii) the effect of including and IHE is studied numerically and experimentally. The fifth section includes additional studies: i) an experimental illustrative comparison between R-134a subcritical cycles against carbon dioxide transcritical cycles; and ii) a numerical analysis of the IHE length influence.

6.2   Experimental facilities

Two experimental facilities, specially designed to study carbon dioxide transcritical cycles, were built in the CTTC (Centro Tecnológico de Transferencia de Calor). The

second experimental unit is the result of major modifications and improvements done to the first unit. The main aspects of the two experimental facilities used to study the carbon dioxide refrigerating cycles (geometry, elements, measuring instruments, etc.) are described in this section.

6.2.1 Carbon dioxide experimental facility

The former experimental facility consists in a single-stage vapor compression cycle. The system general view is schematically represented in Figure 6.3 where the position numbers are equivalent to those of Figure 6.1. The main loop is depicted as a solid line and is made up of the following elements: a carbon dioxide reciprocating compressor, a double pipe counter flow gas-cooler, a metering valve, and a double pipe counter flow evaporator.
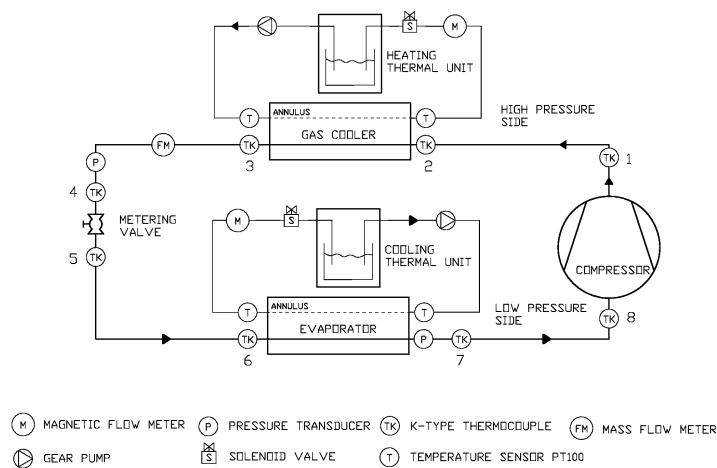

Figure 6.3: Schematic diagram of the transcritical carbon dioxide cycle facility.

The three main components of the system are briefly described in this paragraph. Firstly, the gas-cooler and the evaporator are counter flow double tube helicoidal heat exchangers with the refrigerant flowing through the inner tube. The auxiliary circuit of each heat exchanger consists in a gear pump (to drive the secondary fluid), a thermal unit (to set and control the secondary fluid temperature), a magnetic flow meter (to measure the secondary fluid mass flow rate), a modulating solenoid valve (to control the volumetric flow), and two Pt-100 temperature sensors (to measure the

COMPONENTS		MEASUREMENTS	
Tubing		*Pressure transducers*	
material	stainless steel	limits	0-100/0-160 *bar*
outer diameter	1/4 *in*	accuracy	<0.1% span
Heat exchangers		*Coriolis mass flowmeter*	
sample tube outer diam.	1/4 *in*	limits	0.3-100 *kg/h*
annulus outer diameter	1/2 *in*	accuracy	$\pm$0.5% + *stability*
length	4.5 *m*	repeatability	<0.05% + *stability*
insulation	2.0 *cm*	stability	$\pm0.015\%^a$
Metering valve		*Temperature sensors*	
PARKER	4Z-NSL-V-SS-V	Pt-100 accuracy (gas phase)	$\pm0.06^oC$
C_v	0.039	K-Thermocouples accuracy	$\pm1.5^oC^b$
chocked X_t	0.64		
limits	0-138 *bar*		
Compressor		*Security valve*	
cylinder capacity	1.5 cm^3	C_v	0.41
cyl. cap. (upgraded unit)	2.5 cm^3	chocked X_t	0.67
		spring	155-206 *bar*

^{a} Stability calculated from the maximum flow rate.
^{b} The thermocouples have been calibrated and lower accuracy has been reached ($\pm0.2^oC$).

Table 6.1: General characteristics of the carbon dioxide experimental facilities.

secondary fluid temperatures at the inlet and outlet positions of the heat exchanger). Water is used as the secondary fluid in both heat exchangers. However, for evaporation temperatures under 0 °C, the secondary loop of the evaporator is filled with an appropriate water/glycol mixture. Secondly, the main circuit metering valve consists in a commercial valve specially designed for research applications. It provides a fine degree or precision to regulate the system mass flow rate. And thirdly, the reciprocating compressor consists on a prototype of 1.5 *cm*^{3} cylinder capacity. In fact, several compressors have been tested including hermetic and semi-hermetic types.

The unit is equipped with several measuring instruments along the whole circuit. On one side, the refrigerant fluid temperature is measured at the inlet and outlet positions of each element by means of calibrated K-type thermocouples. On the other side, the system pressure is measured with two pressure transducers placed at the system high and low pressure sides, respectively. In addition to this, the mass flow is obtained from a Coriolis flow meter located between the gas-cooler and the metering valve. Each component of the whole facility - except the compressor - is covered with an insulation layer of 2 *cm* to prevent heat losses. The summarized description of the cycle components and instruments is presented in Table 6.1.

6.2.2 Upgraded carbon dioxide experimental facility

The upgraded experimental facility is an improved version of the unit described in Section 6.2.1. It was specially designed to test the thermal and fluid-dynamic behavior of carbon dioxide vapor compression cycles with internal heat exchange and/or additional compression stages. It includes new elements in the main circuit (internal heat exchanger, intercooler, and auxiliary compressor) and more measuring instruments in order to obtain more detailed experimental data sets. The schematic overview is presented in Figure 6.4 where the numbered positions are equivalent to those reported in Figure 6.2.
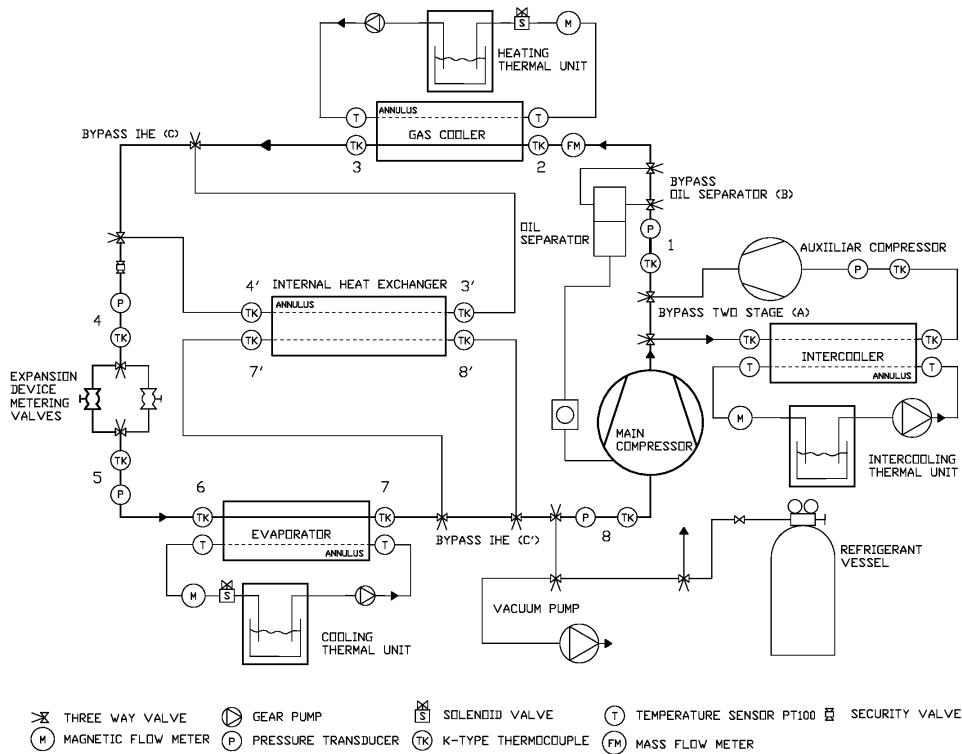

Figure 6.4: Schematic diagram of the upgraded transcritical carbon dioxide cycle facility.

The main loop is depicted as a solid line and consists of a single-stage vapor

compression cycle with two metering valves placed in parallel (to allow a wider range of operating conditions). The facility includes several bypasses achieved by means of three-way valves placed in series. They allow three independent optional modifications of the main loop, namely a two stage vapor compression process (bypass A), the use of an oil separator device (bypass B), and the inclusion of an internal heat exchanger (bypasses C/C').

This unit includes more measuring instruments. The main loop is provided with five pressure transducers (two at the high-pressure side, two at the low-pressure side and one at the intermediate-pressure side) and temperature sensors at the inlet and outlet positions of all the elements (including the internal heat exchanger). The mass flow rate is measured with a Coriolis flow meter located just before the gas-cooler entrance. The characteristics of the cycle elements are basically equal to those from the facility described in Section 6.2.1 (see Table 6.1). Two additional details are worth to be mentioned. Firstly, in the internal heat exchanger, the refrigerant of the suction line flows through the inner tube, while the refrigerant of the high-pressure side flows through the annulus. And secondly, the compressor prototypes tested in this facility have a cylinder capacity of 2.5 cm^3 instead of 1.5 cm^3.

6.2.3 Experimental uncertainty

The experimental uncertainty of a particular measurement (usually expressed as $\phi \pm \sigma_\phi$) is directly obtained from the sensor accuracy (see Table 6.1). However, the experimental uncertainty of a result derived from a collection of measurements (e.g. COP, cooling capacity, etc.) is obtained from a formula that calculates the propagation of uncertainty. The formula is based on the idea of a first-order Taylor series expansion of functions of many variables:

$$\sigma_f^2 = \sigma_x^2 \left(\frac{\partial f}{\partial x} \right)^2 + \sigma_y^2 \left(\frac{\partial f}{\partial y} \right)^2 + \sigma_z^2 \left(\frac{\partial f}{\partial z} \right)^2 + ... \tag{6.1}$$

Where f is a well-behaved function of physical variables $(x, y, z, ...)$ which have uncertainties $(\sigma_x, \sigma_y, \sigma_z, ...)$. For further details see Bervington and Robinson [9].

6.3 Numerical model and resolution procedure

The global vapor compression cycle is solved by means of a numerical model that includes different subroutines. The thermal and fluid-dynamic behaviour of each cycle component is obtained from the resolution of the appropriate equations. Most of the components are represented as a sequence of control volumes where the governing equations are solved iteratively and empirical information is used when needed.

Both single- and two-phase flows are considered. In the following sections the numerical model of each cycle component is described and the whole vapor compression refrigerating cycle resolution procedure is detailed.

6.3.1 Compressor numerical model and characterisation

Two types of compressors are used in the field of refrigeration: dynamic (centrifugal, axial, radial, etc.) and positive displacement (rotary, screw, scroll, reciprocating, etc.). Positive displacement compressors mechanically drive the refrigerant gas from the evaporator at the low-pressure side to the condenser at the high pressure-side, reducing the compressor chamber volume. Reciprocating compressors use pistons that are driven directly through a pin and a connecting rod from the crankshaft. In hermetic reciprocating compressors, the motor and crankshaft are contained within the same housing and are in contact with the lubrication oil.

Figure 6.5 shows a schematic representation of a commercial hermetic reciprocating compressor, which is representative of the compressors numerically and experimentally tested in this work. The low pressure dry gas from the evaporator enters to the space between the shell and the motor-compressor unit, i.e. crankcase and electrical motor. After that, it goes across the suction ducts to the cylinder, where the piston compresses the gas, raising its pressure. Leakage mass flow rate is considered. Finally, the high pressure gas is discharged from the cylinder to the discharge plenum and goes through the impulsion ducts to the condenser (or gas-cooler). The gas, on its way across the suction and discharge ducts, goes through different parts such as tubes, mufflers, manifolds, valves and the compression chamber.

Most cooling systems in use today rely on reciprocating piston type compressors. Hermetic reciprocating compressors are typically used in household refrigerators, freezers, residential air conditioners, low capacity commercial air conditioning, and commercial refrigerating units such as food services, ice machines, beverage dispensers, or condensing units.

Both hermetic and semi-hermetic reciprocating compressor prototypes have been experimentally and numerically studied in the CTTC. They were specially designed for small cooling capacity refrigeration applications with carbon dioxide (i.e. vending machines, display cabinets, etc.). In the present work, the experimental tests have been carried out using the facilities described in Section 6.2, while the numerical simulations have been done with the simulation model presented in Pérez-Segarra et al. [10]. Furthermore, the tested compressors have been characterised by means of different efficiencies. The main aspects of both the numerical model and the compressor characterisation are detailed in the following lines.
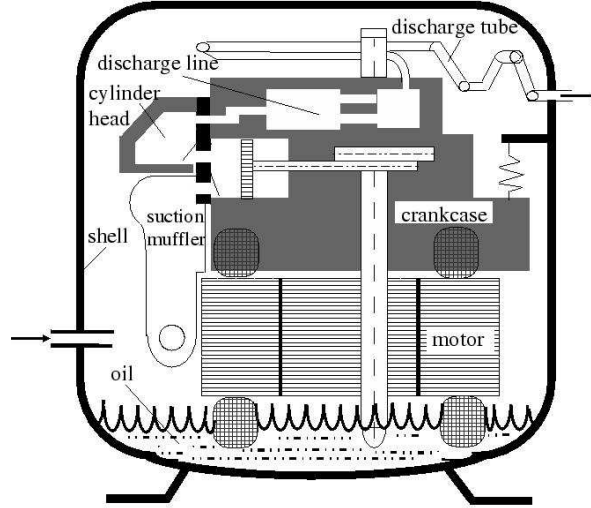
Figure 6.5: Hermetic reciprocating compressor.

Numerical model

The numerical model presented in Pérez-Segarra et al. [10], and extensively validated in subsequent works [11, 12], is based on the integration of the fluid equations (continuity, momentum, energy) in a transient and one-dimensional form along the whole compression domain (suction line, compression chamber and discharge line). Equations 6.2, 6.3 and 6.4 show the continuity, momentum and energy conservation expressions, respectively. Equation 6.3 has particular assumptions related to the uniform cross sectional area, the sudden enlargement/contraction and the compressible flow through valves. The fluid flow equations are discretized using an implicit control volume formulation and solved by means of a pressure-based algorithm of the SIMPLE type (Semi Implicit Method for Pressure Linked Equations) [13] extended to compressible flow.

$$\frac{\partial m}{\partial t} + \sum \dot{m}_o - \sum \dot{m}_i = 0 \tag{6.2}$$

$$\frac{\partial m\bar{v}}{\partial t} + \sum \dot{m}_o v_o - \sum \dot{m}_i v_i = F \tag{6.3}$$

$$\frac{\partial m\bar{h}}{\partial t} - V\frac{\partial \bar{p}}{\partial t} + \sum \dot{m}_o h_o - \sum \dot{m}_i h_i = \bar{\dot{Q}}_{wall} \tag{6.4}$$
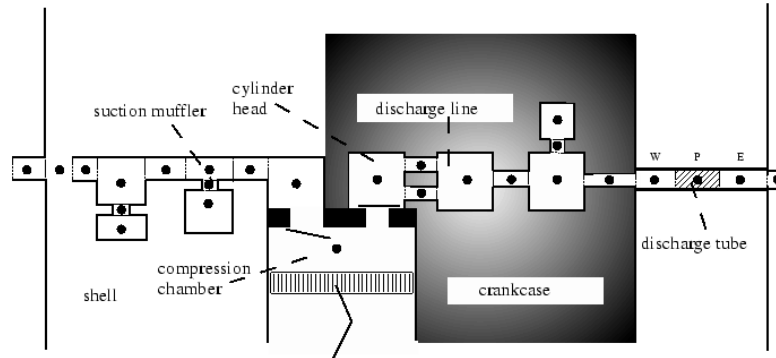
Figure 6.6: Discretization of an hermetic reciprocating compressor.

The discretization is based on the division of the whole compressor domain (both tubes and chambers where the gas is flowing, shell, crankcase, etc.) into strategically distributed control volumes. Some parts of the compressor, like the mufflers or the compression chamber, constitute a single control volume and can not be divided into smaller ones. Other parts, like the tubes or the different solid elements, can be divided into an arbitrary number of control volumes. For each control volume, a grid node is assigned at its center. Figure 6.6 shows a schematic representation of both the control volumes and the grid node distribution along the gas flow domain.

In addition to the gas flow equations: i) the valve positions and the effective flow areas are evaluated by means of a multidimensional approach based on the fluid interaction with the valve; ii) the force balances in the crankshaft and connecting rod mechanical system are simultaneously solved at each time step; and iii) the thermal analysis of the solid elements is achieved from global energy balances at each macro volume considered (shell, muffler, tubes, cylinder head, crankcase, motor, etc.). The model needs empirical inputs for closure (heat transfer correlations, friction factors and contract coefficients).

Compressor characterisation

The CPU time of the compressor numerical model needed to attain a periodical solution is significantly higher than the time needed to reach the steady state solution of the refrigerating cycle algorithm presented in Section 6.3.4. Thus, in order to reduce the compressor calculation time, the compressor modelling has been done on the basis of a global energy balance between its inlet and outlet cross sections considering cyclical steady state:

$$\dot{m}(h_1 - h_8) = \dot{Q}_{sh} - \dot{W}_e \tag{6.5}$$

The thermodynamic behavior of the compressor is defined by means of different efficiencies obtained from the comparison between the tested compressor vs. an ideal one. The comparisons are performed using both compressors (real and ideal) with the same fluid and under well defined refrigerating cycle conditions: evaporation and condensation temperatures, and superheating and subcooling temperatures. The refrigerating system is conceived with no pressure losses in both the evaporator and the condenser (or gas-cooler), under isenthalpic expansion and without heat transfer and pressure losses in the connecting tubes.

It is assumed that the ideal compressor has the same geometry (swept and clearance volume) and working conditions (inlet state, outlet pressure and nominal frequency) than the real one, but operating reversibly according to: adiabatic compression and expansion, and isobaric suction and discharge processes. Additional assumptions are considered: the refrigerant gas behaves as a perfect gas, neither the pressure nor the temperature change along the suction or discharge lines (no pressure losses and no heat transfer), and neither mechanical nor electrical losses are allowed.

Thus, the ideal compressor is defined from few parameters: inlet state and outlet pressure (p_8, T_8 and p_1 as shown in Figure 6.1 left), type of fluid (R, c_p), and compressor characteristics (V_{cl}, c and f_n). The volumetric flow pumped by the ideal (isentropic) compressor and the specific input work required are obtained as follows [14]:

$$\dot{G}_s = V_{cl}[1 - c(\Pi^{1/\gamma} - 1)]f_n \tag{6.6}$$

$$w_s = \frac{RT_8}{M} \frac{\gamma}{\gamma - 1}[\Pi^{(\gamma-1)/\gamma} - 1] \tag{6.7}$$

Where Π is the compression ratio (p_1/p_8) and γ is the adiabatic exponent ($c_p/(c_p - R/M)$). The specific heat is assumed constant and evaluated from the real fluid thermophysical properties at the arithmetic mean (temperature and pressure) between the suction and discharge lines of the ideal compressor. An even more ideal compressor can be imagined without clearance volume (c=0). This compressor will have a higher volumetric flow rate, $\dot{G}_s^{c=0} = V_{cl}f_n \geq \dot{G}_s$, for the same cycle operating conditions. The refrigerating effect and the compressor power consumption are also higher but both compressors have the same specific refrigerating effect and the same specific work.

The efficiencies obtained from the comparison between ideal and real compressors are now described. Firstly, the volumetric efficiency which is defined as the ratio of the actual volumetric flow rate at the inlet conditions and the maximum one: $\eta_v = (\dot{m}/\rho_8)/\dot{G}_s^{c=0}$. Secondly, the isentropic or compression efficiency, which is usually defined as the ratio of the specific work delivered to the gas by the ideal compressor and

the specific work delivered by the actual one: $\eta_s = w_s/w_{cp}$. Thirdly, the mechanical and electrical efficiencies. The energy supply to the compressor is greater than the energy delivered to the refrigerant gas due to mechanical friction losses and electrical motor inefficiencies: $\eta_m\eta_e = w_{cp}/w_e$. And fourthly, the heat transfer losses efficiency which represents the ratio between the heat transfer losses through the shell vs. the power consumption: $\eta_{Qsh} = 1 - \varepsilon_{Qsh} = 1 - (q_{sh}/w_e)$. The compressor parameters mentioned above are function of the compressor geometry, working refrigerant fluid, compression ratio, compressor inlet temperature, etc. A more detailed description of the compressor characteristic efficiencies used in this work is reported in [15].

6.3.2 Numerical simulation of in-tube two-phase flow and the solid elements. Heat exchangers and connecting tubes

The numerical simulation model of the thermal and fluid-dynamic behavior of two-phase flow inside tubes is obtained from the integration of the fluid governing equations along the flow domain, which is split into a number of finite control volumes as is shown in Figure 2.1. Considering a steady-state quasi-homogeneous fully-implicit one-dimensional model, the discretized governing equations (continuity, momentum and energy) show the following form:

$$\dot{m}_i - \dot{m}_{i-1} = 0 \tag{6.8}$$

$$\dot{m}_i v_i - \dot{m}_{i-1} v_{i-1} = (p_{i-1} - p_i)S - \bar{\tau}_i\pi D\Delta z_i - \bar{\rho}_i g sin(\theta)S\Delta z_i \tag{6.9}$$

$$\dot{m}_i(h_i + e_{c,i} + e_{p,i}) - \dot{m}_{i-1}(h_{i-1} + e_{c,i-1} + e_{p,i-1}) = \bar{\dot{q}}_i\pi D\Delta z_i \tag{6.10}$$

This formulation requires the use of empirical correlations to evaluate the void fraction, the shear stress and the heat transfer coefficient. The most important details of this model have been presented in Chapter 2. The resolution is carried out on the basis of a SIMPLE-like algorithm or a step-by-step numerical scheme. In the latter case, the governing equations are rearranged and solved for the control volume downstream node. Thus, from the inlet flow conditions (i.e. $\dot{m}_1, p_1, h_1$) each control volume outlet state is calculated sequentially. The tube wall temperature map acts as the boundary condition for the whole internal flow.

The energy balance over the solid part of the tube is also considered. The tube is discretized in a way, that for each fluid control volume, there is a corresponding tube temperature (see Figure 2.1). The balance takes into account the conduction heat transfer along the tube itself together with the heat transferred to/from the external environment and the heat exchanged with the internal fluid. The discretized energy equation applied at each solid control volume is expressed as follows:

$$\lambda_{i_-}\frac{T_i - T_{i-1}}{z_i - z_{i-1}}S + \lambda_{i_+}\frac{T_{i+1} - T_i}{z_{i+1} - z_i}S + \bar{\bar{q}}_{ext,i}\pi D_{ext}\Delta z_i - \bar{\bar{q}}_i\pi D\Delta z_i = 0 \qquad (6.11)$$

The process of solving in a segregated way the inner fluid, the solid tube and the external condition (if necessary), is carried out iteratively until a converged solution is obtained. The solution is given when all the variables (mass flow rate, pressure, enthalpy, tube temperatures and external variables) agree with the convergence criteria $(|(\phi^* - \phi)/\phi| \le \xi)$.

6.3.3 Expansion device

Two types of expansion devices can be considered in the numerical simulation model: capillary tube or expansion valve.

The capillary tube is evaluated in a similar way as the fluid refrigerant in the heat exchangers, but considering the entropy creation equation. The inlet mass flow rate, or alternatively the inlet pressure, is iteratively estimated by means of a numerical algorithm in order to obtain critical flow conditions. The critical condition is reached when entropy creation is not verified. After the evaluation of critical conditions, the critical pressure is compared against the discharge pressure. If the critical pressure is greater than or equal to the discharge pressure the flow is critical and the discharge shock wave is solved. Otherwise, the flow is non-critical and the capillary tube is solved in the same way as the auxiliary tube connections. A detailed description of the numerical model implemented is presented in Chapter 4.

In the experimental cases herewith presented, instead of a capillary tube, a commercial expansion device was used in order to accurately adjust the cycle flow rate. The numerical model is based on considering the flow through the valve as an isenthalpic sudden contraction along the tube. The mass flow rate is evaluated following the hydraulics equation:

$$\dot{m} = A_D C_D \sqrt{2\rho_4(p_4 - p_5)} \qquad (6.12)$$

For single-phase incompressible fluids the flow coefficient C_D is constant, however for two-phase flow mixtures it must be determined by experiments. Wile [16] proposed Equation 6.13 where the flow coefficient C_D is expressed from the valve inlet liquid refrigerant density and the valve outlet specific volume. The correlation was based on a painstaking study of the mass flow characteristic of thermal expansion valves.

$$C_D = 0.02005\sqrt{\rho_4} + \frac{0.634}{\rho_5} \qquad (6.13)$$

The flow area A_D is evaluated from the geometric characteristics of the selected valve and its adjusting screw position, which is directly related to the valve number

of turns. The valve installed in the experimental unit of Section 6.2.1 has an internal diameter of 0.8 mm and an inclination angle of 0.8°.

6.3.4 Refrigerating cycle global resolution procedure

The numerical simulation model is based on a global algorithm that solves all the system elements based on a successive substitution method. The algorithm takes into account both the basic refrigerating cycle and the refrigerating cycle with internal heat exchange. In fact, the cycle resolution without IHE represents a particular case from the general resolution.

The algorithm structure consists in a main program that couples the specific subroutines that solve each one of the system elements. Thus, at each global iterative step, the subroutines are called sequentially, transferring adequate information to each other until convergence is reached. The boundary conditions for the simulation of the whole system are: the evaporator and gas-cooler external conditions (inlet pressure, inlet temperature and mass flow rate of the secondary fluid), the compressor parametric information (efficiencies expressions), the ambient conditions (pressure and temperature) and the position of the valve adjusting screw (used to calculated the expansion valve cross section A_D).
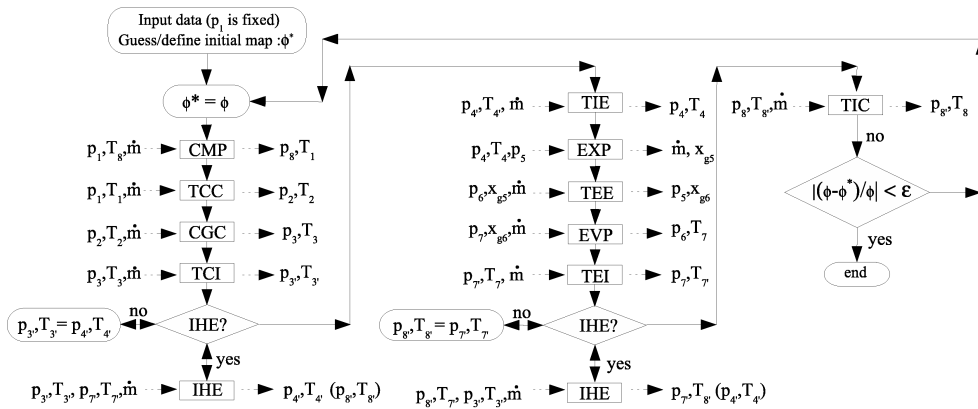

Figure 6.7: Numerical resolution algorithm of transcritical cycle with and without IHE (steady state).

Figure 6.7 shows how the subroutines of the cycle elements are called sequentially and which information is transferred from one component to another. The nomenclature correspond to that from Figure 6.2. The different elements evaluated in the

numerical simulation are: the compressor (see Section 6.3.1), the expansion device (see Section 6.3.3), the gas-cooler, the evaporator, the internal heat exchanger and the connecting tubes (see Section 6.3.2). Thus, eight points represent the inlet/outlet cross sections of the basic elements and four more points represent the corresponding cross sections of the internal heat exchanger. The governing equations of the IHE are solved twice along the iterative cycle resolution, although each time two of the four outlet conditions are considered for the next step (i.e. after solving points 1, 2, and 3 the IHE is evaluated to obtain the fluid conditions at point 4', and after solving the positions 4, 5, 6 and 7 the IHE is evaluated to obtain both the fluid pressure at point 7' and the enthalpy at point 8').

The cases studied in this work have been conducted under steady state conditions. Therefore, the mass flow rate in the whole domain is constant. Among the whole variables of the cycle (pressures, enthalpies and mass flow rate), the outlet compressor pressure (p_1) has been chosen to be fixed in the numerical model in order to have the same number of equations and unknown variables. It may be noticed that the information transferred between elements changes according to the cycle element position. The elements on the high-pressure side of the cycle are fed with their inlet conditions (the outlet conditions are returned) while the elements on the low-pressure side are fed with their inlet enthalpy and outlet pressure (the outlet enthalpy and inlet pressure are returned). In the latter case, if the two-phase flow inside ducts is solved by means of a SIMPLE algorithm the solution is directly calculated but, if the solution is attained from a step-by-step algorithm, additional iterations must be carried out in each element of the low-pressure side.

6.4   Numerical vs. experimental results

The experimental data collected from the facilities described in Section 6.2 are compared against the numerical model described in Section 6.3. The validation process includes three different steps. Firstly, three experimental cases have been performed in order to tune up the former transcritical carbon dioxide facility built in the CTTC and to make the first comparison against the model numerical predictions. The compressor characterisation is presented together with both the experimental data and the numerical model predictions for the whole cycle. Secondly, an additional experimental work is carried out in the same experimental unit with the aim of comparing the performance of two compressor prototypes and extend the numerical code validation. Thirdly, the upgraded facility has been experimentally tested considering the internal heat exchanger effect. The measurements have been compared against the numerical model for both cases: with and without internal heat exchanger.

6.4.1 Transcritical cycles

The simulation of a single-stage vapor compression refrigerating cycle working with carbon dioxide at transcritical conditions is presented and compared against experimental data. Three different transcritical cases have been conducted in the experimental unit detailed in Section 6.2.1. The experimental measurements have been carried out for a fixed gas-cooler pressure (about 100 bar) and three different evaporation temperatures (-10, -5 and 0 ^oC). The metering valve is used to regulate both the system mass flow rate and the system pressures as it provides a fine degree of precision. The main boundary conditions of the experimental cases are summarized in Table 6.2.

	cycle		gas-cooler		evaporator	
	$p_{gc}(bar)$	$\dot{m}(kg/s)$	$T_{aux,i}(^oC)$	$\dot{m}_{aux}(kg/s)$	$T_{aux,i}(^oC)$	$\dot{m}_{aux}(kg/s)$
case a	102.63	0.001528	25.92	0.034500	24.73	0.026666
case b	102.64	0.001862	25.91	0.034167	24.73	0.027500
case c	101.31	0.002723	25.87	0.035333	24.70	0.028333

Table 6.2: Parameters of the former experimental tests.

The facility has been equipped with a 1.5 cm^3 cylinder capacity compressor. The characterisation of this element has been evaluated by means of the advanced compressor model presented in Section 6.3.1. The results are presented in Figure 6.8 (the electrical/mechanical efficiency is nearly constant in all the studied cases and has a value of approximately 75-76%) where the thick line represents the fitted curve for the relationship between the pressure ratio and the efficiencies. The expression used for the curve fitting is the following:

$$\eta = a_1 + a_2\Pi + a_3\Pi^2 \qquad (6.14)$$

The numerical predictions have been done for each element separately and for the whole refrigerating system. Table 6.3 shows some comparative results between the compressor simulation (using the characteristic parameters and without considering the whole cycle resolution) and the experimental measurements, while Table 6.4 shows comparative results between the gas-cooler and the corresponding experimental data. In both cases, a quite good agreement is observed (e.g. the gas-cooler outlet secondary fluid temperature prediction is within 1.1%). Similar evaluations - not reported in the present text - have been made for the evaporator and the expansion device obtaining the same grade of accuracy.

The complete refrigerating system comparison for the three cases is detailed in Table 6.5 (the indexes are equivalent to those of Figure 6.1). The boundary conditions used in the numerical model are: inlet flow conditions of secondary fluids, gas-cooler
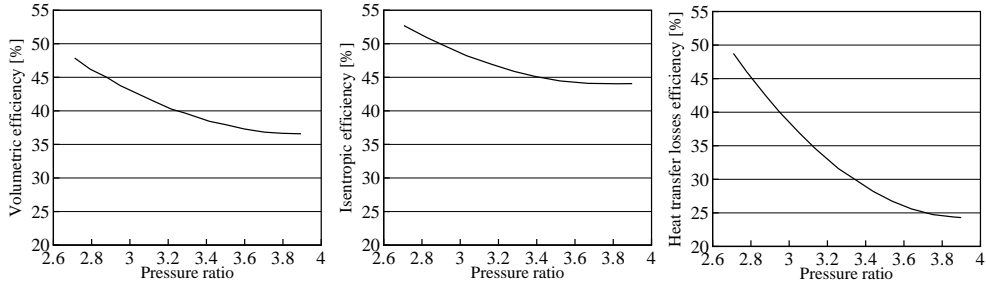
Figure 6.8: Numerical parameters of carbon dioxide hermetic reciprocating compressors.

	$T_i(^oC)$	$T_o(^oC)$	$P_i(bar)$	$P_o(bar)$	$\dot{m}(kg/s)$
Numerical	(24.28)	119.47	26.615	(102.630)	(0.001528)
Experimental	(24.28)	119.44	26.610	(102.630)	(0.001528)

Table 6.3: Compressor: experimental vs. numerical results (boundary conditions in brackets).

	T_i (^oC)	T_o (^oC)	P_i (bar)	P_o (bar)	$\dot{m}$ (kg/s)	$\dot{m}_{aux}$ (kg/s)	$T_{aux,i}$ (^oC)	$T_{aux,o}$ (^oC)
Numerical	(119.44)	25.92	(102.630)	102.625	(0.001528)	(0.0345)	(25.92)	28.86
Exp.	(119.44)	25.31	(102.630)	102.630	(0.001528)	(0.0345)	(25.92)	28.55

Table 6.4: Gas-cooler: experimental vs. numerical results (boundary conditions in brackets).

pressure and circuit mass flow rate. A reasonable accordance between experimental and numerical data has been obtained. For all variables, except for the inlet temperature of the evaporator, the numerical prediction is within 3% of the experimental data. Regarding the evaporation temperature, it is not appropriate to calculate its discrepancy with the experimental data by means of a percent value because of its proximity to 0 ^oC. However, in these cases, the temperature differences are relatively small (0.61 ^oC for T_5 in case c).

Finally, the general behavior of transcritical cycles is observed in Figures 6.9 and 6.10 where both the pressure vs. enthalpy and the temperature vs. entropy diagrams are depicted, respectively.

	$P_{ev}(bar)$	$P_{gc}(bar)$	$T_1(^oC)$	$T_3(^oC)$	$T_5(^oC)$	$T_7(^oC)$	x_{g5}	$\dot{m}(kg/s)$
case a								
Numerical	26.681	(102.630)	119.71	25.92	-9.69	24.54	0.314	(0.001528)
Exp.	26.610	(102.630)	119.44	25.31	-10.04	24.28	0.308	(0.001528)
case b								
Numerical	30.120	(102.640)	116.78	25.91	-5.36	24.53	0.288	(0.001862)
Exp.	30.020	(102.640)	116.41	25.38	-5.72	24.21	0.283	(0.001862)
case c								
Exp.	35.560	(101.310)	113.26	25.41	0.49	24.18	0.242	(0.002723)
Numerical	35.836	(101.310)	113.42	25.87	1.10	24.42	0.245	(0.002723)

Table 6.5: Refrigerating cycle: experimental vs. numerical results (boundary conditions in brackets).
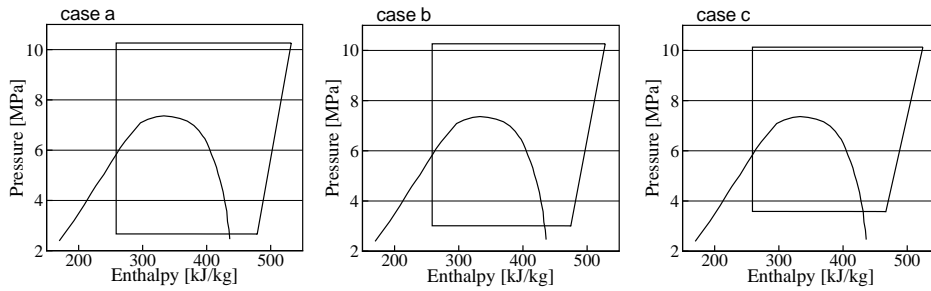

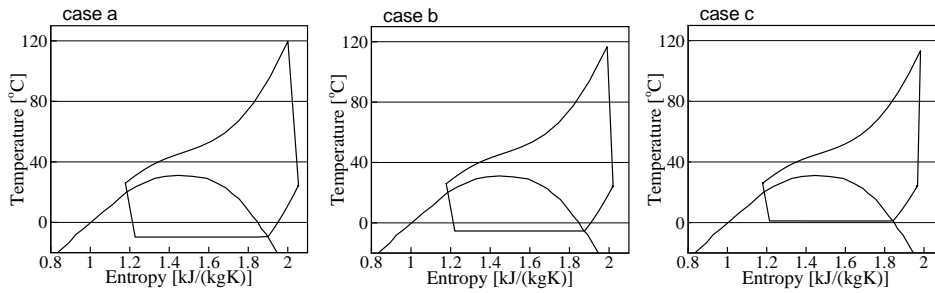**Figure 6.9:** Pressure vs. enthalpy diagrams.

Figure 6.10: Temperature vs. entropy diagrams.

6.4.2 Transcritical cycles. Hermetic compressor prototypes comparison

Two different carbon dioxide compressor prototypes provided by ACC Spain S.A. have been tested (CL15H1 and CL15H2) in the experimental facility described in Section 6.2.1. The main geometric parameters of both the first and the second carbon dioxide compressor prototypes are detailed in Table 6.6. The second one is an improvement of the first prototype, reducing the clearance volume, the shell volume and the piston leakage, and improving the direct suction line.

CL15H1 (prototype 1)		CL15H2 (prototype 2)	
Suction line		*Suction line*	
inlet diameter	5.8 mm	inlet diameter	6.2 mm
chambers	5.1/1.6 cm^3	chambers	5.1/1.6 cm^3
plenum	1.0 cm^3	plenum	1.2 cm^3
shell	3350 cm^3	shell	1570 cm^3
Discharge line		*Discharge line*	
outlet diameter	5.0 mm	outlet diameter	5.0 mm
chambers	9.0/6.5 cm^3	chambers	9.0/6.0 cm^3
plenum	6.5 cm^3	plenum	6.5 cm^3
clearance ratio	5.42%	clearance ratio	4.66%
Crankcase		*Crankcase*	
bore diameter	14.0 mm	bore diameter	14.0 mm
suction stop	0.8 mm	suction stop	0.8 mm
suction orifice diameter	3.2 mm	suction orifice diameter	4.0 mm
length stroke	9.744 mm	length stroke	9.744 mm
discharge stop	0.8 mm	discharge stop	0.8 mm
discharge orifice diameter	3.0 mm	discharge orifice diameter	3.0 mm

Table 6.6: Main parameters of the two carbon dioxide hermetic reciprocating compressor prototypes (CL15H1 and CL15H2).

Both compressors have been numerically studied with the model described in Section 6.3.1 and characterised with four different efficiencies, namely, the volumetric efficiency (η_v), the isentropic efficiency (η_s), the mechanical and electrical efficiency (η_{me}) and the heat transfer losses efficiency (η_{Qsh}). The results are shown in Figure 6.11 where the efficiencies are plotted vs. the compressor pressure ratio for different evaporation temperatures. This characterisation allows to speed up the compressor resolution procedure in order to couple it with the global vapor compression refrigerating cycle algorithm presented in Section 6.3.4 (the resolution time is drastically reduced).

The numerical vs. experimental results of the whole refrigerating cycle are shown in Tables 6.7 and 6.8. The experimental uncertainty of the power consumption is about $\pm 1\%$ while for the COP and cooling capacity is about $\pm 2\%$ (see Equation 6.1). In this case, the boundary conditions used in the numerical model are: inlet flow
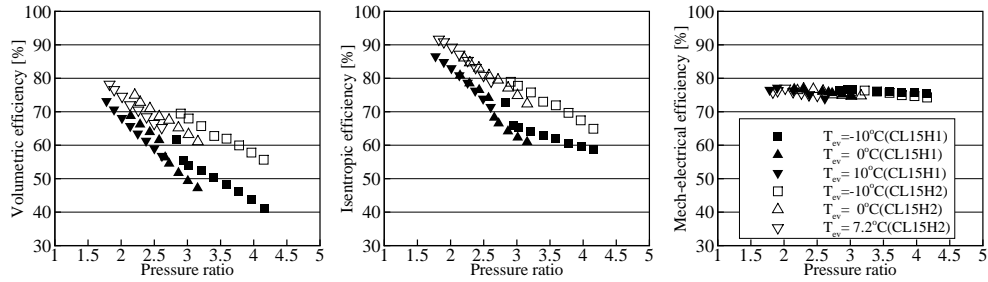
Figure 6.11: Numerical parameters of both carbon dioxide hermetic reciprocating compressors (CL15H1 and CL15H2).

conditions of secondary fluids, gas-cooler pressure and valve aperture degree (instead of the refrigerant mass flow rate).

The cycle numerical and experimental results for the first carbon dioxide compressor (CL15H1) are detailed in Table 6.7. The conditions considered were: inlet fluid compressor temperature 35 ^oC, outlet gas-cooler temperature 35 ^oC, gas-cooler pressure 90 bar, and evaporation temperatures -10, 0 and 10 ^oC. The percentage difference between the numerical prediction and the experimental measurement of the compressor power consumption ($\dot{W}_e$), the cooling capacity ($\dot{Q}_{ev}$), the mass flow rate ($\dot{m}$) and the COP are lower than 4.7, 4.4, 7 and 6.4%, respectively. For the temperatures T_1, T_3 and T_7, the differences are lower than 4.6%. Due to the difficulty of accurately measuring the mean temperature of a two-phase flow, the temperature at the evaporator inlet (T_5) is deduced from the pressure measurement and considering an isenthalpic expansion.

The cycle numerical and experimental results for the second carbon dioxide compressor (CL15H2) are presented in Table 6.8. In this case, the conditions considered were: inlet fluid compressor temperature 32 ^oC, outlet gas-cooler temperature 32 ^oC, gas-cooler pressure 85 bar, and evaporation temperatures -10, 0 and 7.2 ^oC. The differences between the numerical predictions and the experimental data for the compressor power consumption ($\dot{W}_e$), the cooling capacity ($\dot{Q}_{ev}$), the mass flow rate ($\dot{m}$) and the COP are lower than 4, 7.1, 9.4 and 9%, respectively. For the temperatures T_1, T_3 and T_7, the differences are lower than 9.9%.

Two conclusions are drawn from the results. On one side, the experimental validation presented for carbon dioxide transcritical cycles is acceptable (the maximum difference between the measured and calculated values is lower than 10%). The discrepancies are higher than those obtained in Section 6.4.1 due to the fact that the

		T_{ev}=-10 ^oC		T_{ev}=0 ^oC		T_{ev}=10 ^oC	
		Num.	Exp.	Num.	Exp.	Num.	Exp.
p_{gc}	(bar)	89.71	89.71	90.37	90.37	90.14	90.14
p_{ev}	(bar)	26.78	25.48	33.33	32.97	44.45	44.40
T_1	(^oC)	132.50	127.29	124.97	126.00	101.36	96.87
T_3	(^oC)	35.24	35.24	35.38	35.23	36.34	36.45
T_5	(^oC)	-9.56	-11.30	-1.62	-2.03	9.53	9.48
T_7	(^oC)	34.39	35.38	34.52	35.62	34.44	35.42
x_{g5}		0.482	0.471	0.445	0.433	0.416	0.412
η_v	$(\%)$	48.7	45.5	58.1	56.3	68.1	68.8
$\dot{W}_e$	(W)	323.12	326.47	357.79	343.65	350.87	335.11
η_{sme}	$(\%)$	46.8	46.3	52.6	54.8	62.8	65.7
$\dot{Q}_{ev}$	(W)	367.25	351.65	544.63	525.11	816.03	832.70
$\dot{m}$	(kg/h)	6.95	6.49	10.74	10.41	18.24	18.42
COP		1.136	1.077	1.522	1.557	2.325	2.485

Table 6.7: Global comparative carbon dioxide cycle numerical results vs. experimental data (compressor prototype CL15H1).

		T_{ev}=-10 ^oC		T_{ev}=0 ^oC		T_{ev}=7.2 ^oC	
		Num.	Exp.	Num.	Exp.	Num.	Exp.
p_{gc}	(bar)	84.95	84.95	84.98	84.98	85.78	85.78
p_{ev}	(bar)	26.24	25.31	33.90	33.24	39.74	40.03
T_1	(^oC)	118.00	107.35	105.50	102.12	95.29	95.23
T_3	(^oC)	32.04	31.94	32.50	31.94	32.89	32.11
T_5	(^oC)	-10.27	-11.58	-0.99	-1.77	5.09	5.32
T_7	(^oC)	31.19	31.06	31.17	31.56	31.03	31.83
x_{g5}		0.420	0.431	0.403	0.386	0.373	0.346
η_v	$(\%)$	62.7	59.1	69.9	64.6	73.2	68.9
$\dot{W}_e$	(W)	335.54	331.57	345.22	351.66	345.59	360.06
η_{sme}	$(\%)$	55.3	56.0	61.7	60.6	65.6	64.5
$\dot{Q}_{ev}$	(W)	488.58	469.09	695.93	649.51	851.32	842.02
$\dot{m}$	(kg/h)	8.87	8.36	13.32	12.17	17.27	16.22
COP		1.456	1.415	2.015	1.847	2.464	2.285

Table 6.8: Global comparative carbon dioxide cycle numerical results vs. experimental data (compressor prototype CL15H2).

mass flow rate is not considered as a boundary condition in the numerical model. And

on the other side, according to the conditions presented in Tables 6.7 and 6.8, the second compressor prototype shows better COP for the evaporation temperatures of -10 and 0 ^oC (up to 30% higher), while similar COP values are obtained between the CL15H1 compressor at 10 ^oC and the CL15H2 compressor prototype at 7.2 ^oC.

6.4.3 Transcritical cycles with internal heat exchange

In this section, the numerical model predictions have been compared against experimental data for transcritical cycles with internal heat exchange. The experimental data have been obtained from the upgraded experimental facility described in Section 6.2.2. Both the experimental work and the simulations have been done in order to validate the numerical model when the internal heat exchanger (IHE) is taken into account. The results have been oriented with the aim to analyse: i) the influence of an optimal discharge pressure (different to conventional subcritical cycles) depending on the ambient temperature when real working conditions are considered (instead of the calorimeter test conditions of Sections 6.4.1 and 6.4.2); and ii) the system performance improvement when an internal heat exchanger is added to the cycle.

Working fluid	carbon dioxide
Evaporation temperature	-10 ^oC
Degree of superheat	5 ^oC
Discharge pressure	85 to 115 bar
Evaporator secondary fluid inlet temperature	-5 to 0 ^oC
Gas-cooler secondary fluid inlet temperature	30/40/48 ^oC
Mass flow rate of secondary fluid	3.0 kg/s

Table 6.9: Experimental/numerical test conditions.

The experimental tests have been carried out for different discharge pressures and considering typical commercial refrigeration operational conditions. In all the cases, the refrigerant evaporation temperature was set at -10 $^\circ C$, while three different working ambient temperatures were considered (25, 35, and 43 ^oC). It is worth to mention that the working ambient temperature does not represent the ambient temperature during the experimental data acquisition process. On the contrary, the effect of the ambient temperature was obtained by adjusting the refrigerant temperature at the outlet of the gas-cooler in order to attain the same value than that of commercial units. The double tube counter flow gas-cooler was large enough to obtain similar values between the secondary fluid inlet temperature and the refrigerant outlet temperature, therefore, based on a typical heat exchanger performance where the refrigerant temperature at the outlet of the gas-cooler is approximately 5 ^oC above the working ambient temperature, the secondary fluid inlet temperatures were set at

30, 40, and 48 ^oC, in order to simulate the working ambient temperatures of 25, 35, and 43 ^oC, respectively. Regarding the evaporator refrigerant outlet conditions, the degree of superheat was kept constant at 5 $^{\circ}C$ for all the cases. In order to fulfil the latter condition, since the evaporator was not large enough, the inlet temperature of its secondary fluid was gently modified for each test. The secondary fluids of the gas-cooler and the evaporator were water and a water/glycol mixture (40% propylene glycol), respectively. The details of the experimental test conditions are presented in Table 6.9.

The compressor used for this validation is a semi-hermetic reciprocating compressor prototype of 2.5 cm^3 developed by ACC Spain S.A. It has been numerically studied with the model of Section 6.3.1 and characterised by means of different efficiencies (η_v, η_s, η_{me} and η_{Qsh}). These efficiencies are function of both the pressure ratio and the superheating temperature (which varies when the internal heat exchanger is added to the experimental refrigerating cycle). The efficiencies are expressed by means of a fitting curve of the following type:

$$\eta = a_1 + a_2\Pi + a_3\Pi^2 + a_4\Delta T_{sh} + a_5\Delta T_{sh}^2 + a_6\Pi\Delta T_{sh} \qquad (6.15)$$

Where Π is the pressure ratio, ΔT_{sh} is the superheat temperature degree, and a_i are coefficients which must be appropriately correlated for each efficiency.
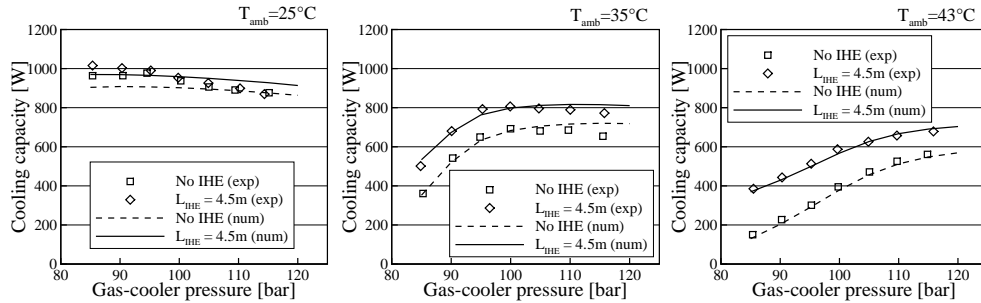

Figure 6.12: Numerical and experimental comparative results of the system cooling capacity with and without IHE vs. gas-cooler pressure, for different ambient temperatures.

The model numerical predictions of both the cooling capacity and COP are compared against the experimental results in Figures 6.12 and 6.13, respectively. The experimental uncertainty of the COP and cooling capacity is about ±2% (see Equation 6.1). Both figures show that the experimental data is basically under predicted

when the IHE is not considered (except at $T_{amb} = 35^oC$ and high gas-cooler pressure), while the data is under predicted at gas-cooler pressure lower than 100 *bar* and over predicted at gas-cooler pressure higher than 100 *bar* when the IHE is considered. In all the cases, there is a reasonable good agreement between predictions and experimental data with percentage differences below 10%.
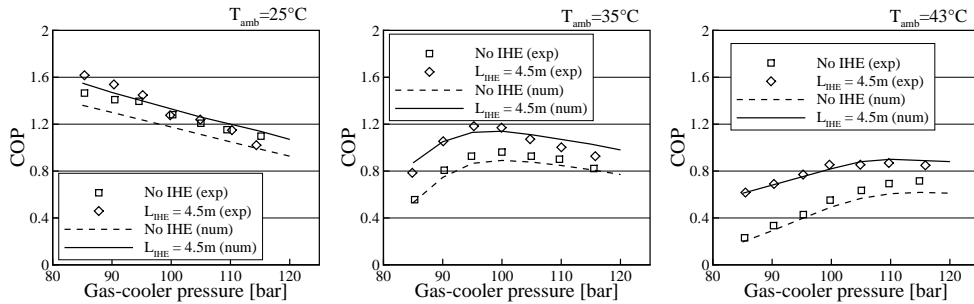

Figure 6.13: Numerical and experimental comparative results of the system COP with and without IHE vs. gas-cooler pressure, for different ambient temperatures.

Some interesting conclusions are drawn from Figure 6.13. In general lines, the COP of the refrigerating system increases when the IHE is considered - except for some of the experimental data reported at the lowest ambient temperature ($T_{amb} = 25^oC$) -. It is observed that the system COP is higher at low ambient temperatures. However, according to all the numerical results and most of the experimental data, the COP increase is more significant at higher ambient temperatures when the IHE is considered. Moreover, the COP evolution is different at each temperature level: i) for low ambient temperatures (25 ^oC) the COP evolution is similar to subcritical cycles as it decreases when the gas-cooler pressure rises; ii) for medium ambient temperatures (35 ^oC) the COP presents a clearly defined optimal gas-cooler pressure; and iii) for high ambient temperatures (43 ^oC) the COP increases but no optimal gas-cooler pressure is attained.

6.5 Studies on carbon dioxide cycles

Two works are reported in this section (one experimental and one numerical) in order to show the possibilities that transcritical carbon dioxide refrigerating cycles have for small cooling capacity systems. The experimental study consists in an illustrative comparison of transcritical carbon dioxide cycles vs. R-134a subcritical cycles at similar operating conditions, while the numerical work is focused on the IHE effect

and its length influence. The results show a promising perspective considering that the compressors used for this work are prototypes under development.

6.5.1 Experimental comparison between R-744 transcritical cycles and R-134a subcritical cycles

In the present section an experimental comparative study of refrigerating cycles between R-134a conventional systems and carbon dioxide transcritical systems is presented. The experimental data of the R-134a cycle were provided by ACC Spain S.A. while the experimental data of the carbon dioxide cycle have been collected from the experimental facility described in Section 6.2.1.
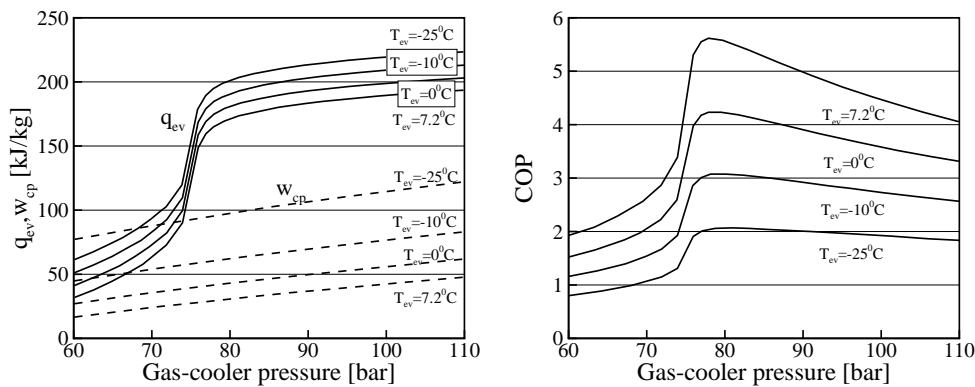

Figure 6.14: Thermodynamic evolution of specific evaporation cooling, specific compression work and COP depending on both gas-cooler pressure and evaporation temperature.

The appropriate test conditions to compare subcritical and transcritical cycles are difficult to establish due to the different phenomena present when heat rejection occurs in each type of cycle (the fluid temperature varies through the gas-cooler but remains constant through the condenser). For R-134a subcritical cycles the experimental tests have been carried out in a calorimeter set-up following ISO 917 where the working conditions were: inlet compressor temperature 35 ^oC, condenser temperature 55 ^oC and subcooling temperature 46 ^oC. The compressor model for the R-134a system is the GLY80 which has a cylinder capacity of 8 cm^3. For carbon dioxide transcritical cycles the working conditions of the experimental tests were: gas-cooler pressure 85 bar and both inlet fluid compressor and outlet gas-cooler temperatures 32 ^oC. Two

compressor prototypes have been used in the carbon dioxide experimental facility: i) a second version of the hermetic compressor (CL15H2) presented in Section 6.4.2; and ii) an upgraded semi-hermetic prototype (SCL15H2). The latter, is an upgraded version of the first semi-hermetic compressor prototype (SCL15H1).

The gas-cooler pressure for the carbon dioxide experimental tests has been chosen from a thermodynamic analysis of the transcritical cycle considering isentropic compression, isenthalpic expansion and isobaric heat exchangers. Figure 6.14 shows the refrigerating system parameters for evaporation temperatures ranging between -25 and 7.2 ^oC and considering that both the inlet compressor and outlet gas-cooler temperatures are 32 ^oC. In all the cases, the system specific compression work increases linearly as the gas-cooler pressure is increased. The system cooling capacity also increases but not linearly (high increase between 60 and 80 *bar* and much less significant increase after 80 *bar*). The COP shows a maximum value at around 80 *bar* for all the evaporation temperatures. Thus, the gas.cooler optimum value must be a compromise between the COP value and an adequate cooling capacity. The gas-cooler pressure selected for the experimental measurements was 85 *bar*.

The experimental tests have been carried out at three different evaporation temperatures (-10, 0 and 7.2 ^oC) and the results are shown in Table 6.10.

	$T_{ev}(^oC)$	$\dot{m}(kg/h)$	$\eta_v(\%)$	$\dot{W}_e(W)$	$\eta_{sme}(\%)$	$\dot{Q}_{ev}(W)$	COP
GLY80 (R-134a)	-10	8.13	67.1	222.3	55.4	375.0	1.687
CL15H2 (CO_2)	-10	8.45	59.0	333.8	53.0	463.8	1.389
SCL15H2 (CO_2)	-10	9.72	67.8	368.8	55.1	533.5	1.447
GLY80 (R-134a)	0	13.02	72.3	273.0	57.6	594.5	2.178
CL15H2 (CO_2)	0	13.07	66.1	353.5	59.1	681.2	1.927
SCL15H2 (CO_2)	0	15.13	76.5	374.4	64.6	788.6	2.106
GLY80 (R-134a)	7.2	17.42	73.9	310.7	56.6	788.2	2.537
CL15H2 (CO_2)	7.2	17.01	66.7	365.2	61.1	841.6	2.313
SCL15H2 (CO_2)	7.2	19.50	76.6	353.6	72.4	964.8	2.728

Table 6.10: Global comparative results (conventional R-134a compressor vs. hermetic and semi-hermetic carbon dioxide compressor prototypes).

The results reported in Table 6.10 indicate that the hermetic and semi-hermetic improved carbon dioxide prototypes (1.5 cm^3 cylinder capacity) are able to produce cooling capacities of 400, 600 and 800 W at evaporation temperatures of -10, 0 and 7.2 ^oC, respectively. The mass flow rate of the carbon dioxide hermetic compressor is similar to that of the GLY80 conventional R-134a compressor. However, the semi-hermetic carbon dioxide prototype presents higher mass flow rates (the values are 19,

16 and 12% higher at the evaporation temperatures of -10, 0 and 7.2 ^oC, respectively). Despite of this the semi-hermetic compressor COP is about 7.5% higher compared to the R-134a conventional compressor at the evaporation temperature of 7.2 ^oC. In all the studied cases, the carbon dioxide semi-hermetic compressor COP is 4, 9 and 18% higher compared to the carbon dioxide hermetic compressor at the evaporation temperatures of -10, 0 and 7.2 ^oC, respectively.

The illustrative experimental comparison presented in this section show promising perspectives due to the fact that carbon dioxide compressors are still prototypes under development.

6.5.2 Numerical study of the IHE length influence

The influence of the internal heat exchanger length has been numerically studied based on both the single-stage transcritical refrigerating cycle presented in Section 6.2.2 and the semi-hermetic reciprocating compressor used in Section 6.4.2. The internal heat exchanger has been simulated as a double tube counter flow device considering different lengths ranging from 0 to 4.5 m. Three different ambient temperatures are considered (25, 35 and 43 ^oC), while the evaporation temperature is fixed at -10 ^oC. The numerical conditions are summarized in Table 6.9. Both the calculated COP and the cooling capacity of the system are plotted in Figures 6.15 and 6.16, respectively.
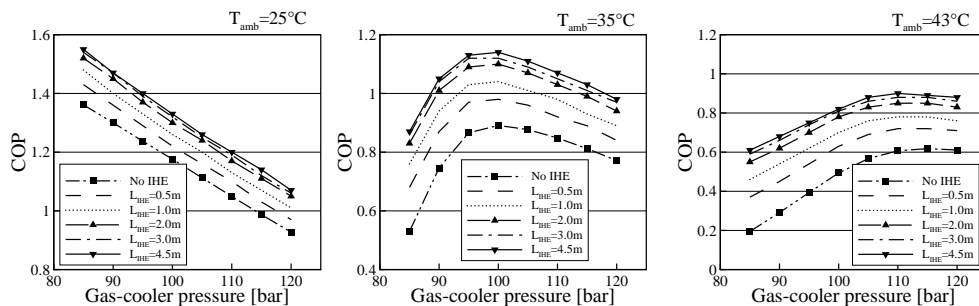

Figure 6.15: Numerical results of COP vs. gas-cooler pressure, for different IHE lengths at different ambient temperatures.

Figure 6.15 shows the influence of the internal heat exchanger length on the refrigerating system COP. It is noticed that for all the simulated ambient temperatures the COP increases when the IHE length increases (although the same COP vs. gas-cooler pressure profile is preserved). The numerical results show that, considering an IHE of 2 m under an ambient temperature of 25 ^oC and with a gas-cooler pressure
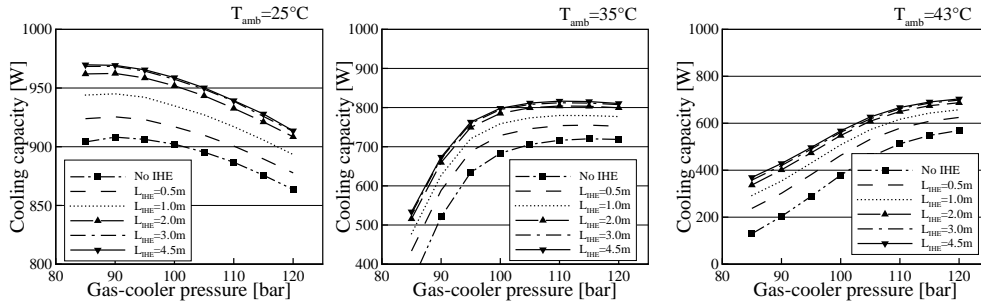
Figure 6.16: Numerical results of cooling capacity vs. gas-cooler pressure, for different IHE lengths at different ambient temperatures.

of 100 *bar*, the cycle COP is increased up to 10% compared to a cycle without IHE. Similarly, for an ambient temperature of 35 ^oC and a gas-cooler pressure of 100 *bar*, the COP is increased up to 23%, and for an ambient temperature of 43 ^oC and a gas-cooler pressure of 115 *bar*, the COP is increased up to 35%. If the IHE length considered is 4.5 *m* instead of 2 *m*, the COP additional increase is 2, 3 and 4% for the ambient temperatures of 25, 35 and 43 ^oC, respectively. It is concluded that the inclusion of an IHE clearly represents an important COP improvement in comparison with a single-stage transcritical cycle without IHE. However, the system performance is significantly enhanced when the IHE length is increased up to 2 *m*, while for larger lengths the COP improvement is less notorious. Similar conclusions are drawn from Figure 6.16.

The influence of the internal heat exchanger length is studied with more detail for the particular case with an ambient temperature of 35 ^oC, a gas-cooler pressure of 100 *bar* and an evaporation temperature of -10 ^oC. The pressure-enthalpy and temperature-entropy diagrams are shown in Figure 6.17. The global refrigerating cycle is modified when the internal heat exchanger length increases. On one side, the evaporator inlet enthalpy decreases and the evaporative two-phase flow region becomes larger. On the other side, both the compressor inlet and outlet temperatures are increased.

The detailed evolution of the refrigerating system parameters is shown in Table 6.11. The refrigerating system performance is improved when longer internal heat exchangers are considered because of two reasons: the increase of the evaporator cooling capacity and the decrease of the compressor power consumption. However, considering that the system mass flow rate decreases (less mass flow is pumped by the compressor due to the lower density of the fluid at the suction line), it is more
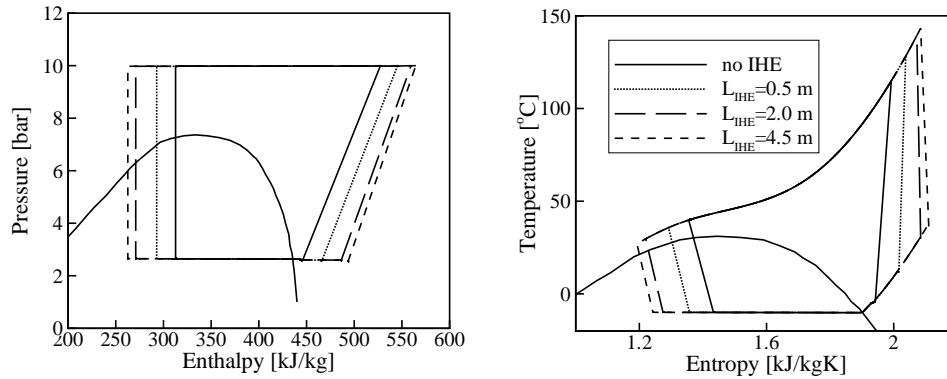
Figure 6.17: Numerical pressure-enthalpy and temperature-entropy diagrams of the refrigerating cycle with and without IHE (T_{amb}=35 ^oC, p_{gc}=100 bar and p_{ev}=26.47 bar).

L_{IHE}	T_8 (^oC)	T_1 (^oC)	x_{g6}	$\dot{Q}_{IHE}$ (W)	$\dot{m}$ (kg/h)	$\dot{W}_e$ (W)	$\dot{Q}_{ev}$ (W)	COP
0	-3.93	115.01	0.53	0.0	18.95	766.9	683.32	0.89
0.5	11.91	128.36	0.45	96.9	17.56	743.9	728.64	0.98
1	20.53	133.96	0.41	145.8	17.06	731.9	758.84	1.04
2	29.7	139.37	0.37	192.4	16.51	716.7	785.21	1.1
3	33.88	141.72	0.35	212.3	16.25	708.9	795.12	1.12
4.5	36.5	143.32	0.34	223.8	16.02	703.2	798.25	1.14

Table 6.11: Numerical results for the whole cycle (T_{amb}=35 ^oC, p_{gc}=100 bar and p_{ev}=26.47 bar).

appropriate to compare the specific compressor work against the evaporator specific heat as shown in Figure 6.18. In this case, the specific evaporation heat increases as well as the specific compression work, but the cycle performance is enhanced because the increase rate of the specific heat is higher. The COP can not be further enhanced with internal heat exchangers longer than 4.5 m as no additional internal heat is transferred between the gas-cooler outlet position and the compressor suction line.
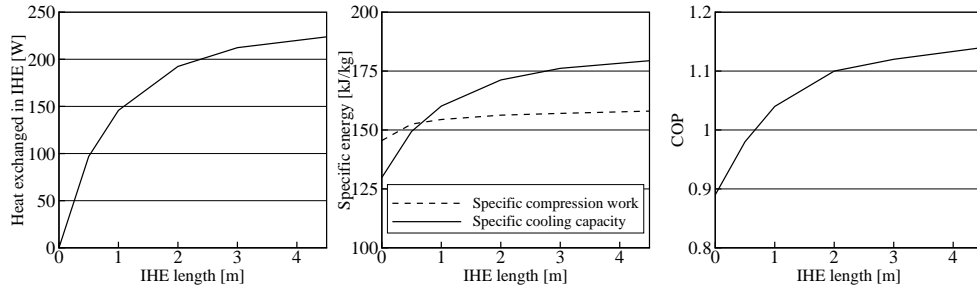
Figure 6.18: Evolution of the refrigerating cycle parameters when the IHE length varies (T_{amb}=35 ^oC, p_{gc}=100 bar and p_{ev}=26.47 bar).

6.6 Concluding remarks

A numerical model to simulate refrigerating cycles has been described and successfully validated. The global resolution procedure allows the consideration of an internal heat exchanger. All the cycle components (evaporator, gas-cooler, expansion device and compressor) have been specifically modeled in order to be used in carbon dioxide transcritical cycles according to the geometry and conditions of the experimental facilities built in the CTTC. The heat exchangers have been modeled by means of the two-phase flow model presented in Chapter 2 but including appropriate correlations for carbon dioxide. The expansion device has been modeled from the valve geometry, an hydraulic equation, and an specific equation for the flow coefficient. The compressor has been numerically studied and characterised by means of efficiencies in order to reduce its calculation time.

The use of carbon dioxide as the refrigerant fluid in small capacity equipments has been experimentally and numerically studied. The numerical model has been compared against experimental data obtained from the CTTC facilities considering transcritical cycles with and without heat internal heat exchange. In both cases good agreement between the numerical model and the measurements has been observed. Different studies have been carried out (experimental comparison between transcritical carbon dioxide cycles and conventional units working with R-134a, numerical study of the transcritical cycle with internal heat exchange) and have shown promising perspectives for the use of this refrigerant in small cooling capacity refrigerating systems.

Nomenclature

A_D	expansion valve cross section, m^2
a_i	curve fitting constants
c	clearance ratio, m^3, $(c = \frac{V_{min}}{V_{cl}})$
C_D	expansion valve flow coefficient
c_p	specific heat capacity, $J \cdot kg^{-1} \cdot K^{-1}$
COP	coefficient of performance
D	tube diameter, m
e	specific energy, $J \cdot kg^{-1}$
F	forces in the flow direction, $kg \cdot m \cdot s^{-2}$
f_n	nominal compressor frequency, Hz
$\dot{G}$	volumetric flow rate, $m^3 \cdot s^{-1}$
g	acceleration due to gravity, $m \cdot s^{-2}$
h	specific enthalpy, $J \cdot kg^{-1}$
IHE	internal heat exchanger
m	mass, kg
$\dot{m}$	mass flow rate, $kg \cdot s^{-1}$
M	molecular weight, $kg \cdot kmol^{-1}$
p	pressure, Pa
$\dot{Q}$	heat transfer, W
$\dot{Q}_{ev}$	evaporator cooling capacity, W
$\dot{Q}_{sh}$	compressor shell heat losses, W
q_{ev}	evaporator specific heat, $J \cdot kg^{-1}$
q_{sh}	compressor shell losses specific heat, $J \cdot kg^{-1}$
$\dot{q}$	heat flux, $W \cdot m^{-2}$
R	gas constant, $J \cdot K^{-1} \cdot kmol^{-1}$
S	cross section, m^2
T	temperature, K
t	time, s
V	volume, m^3
V_{cl}	swept volume, m^3
v	fluid velocity, $m \cdot s^{-1}$
$\dot{W}_e$	compressor power consumption, W
w_{cp}	compression specific work, $J \cdot kg^{-1}$
w_e	electrical specific work, $J \cdot kg^{-1}$
w_s	isentropic specific work, $J \cdot kg^{-1}$
z	axial position, m

Greek symbols

γ	isentropic index, $(\gamma = \frac{c_p}{c_v})$
ΔT_{sh}	degree of superheating, K
Δz	axial step, m
ε_{Qsh}	deviation respect to the reference case
η_e	electrical efficiency
η_m	mechanical efficiency
η_{Qsh}	compressor heat transfer shell losses efficiency
η_s	isentropic efficiency
η_v	volumetric efficiency
ξ	convergence accuracy criterion
λ	thermal conductivity, $W \cdot m^{-1} \cdot K^{-1}$
Π	pressure ratio, $(\Pi = \frac{p_{out}}{p_{in}})$
ρ	fluid density, $kg \cdot m^3$
σ	uncertainty
τ	shear stress, Pa
ϕ	measured/discretized variable

Subscripts

amb	ambient
aux	auxiliary fluid
c	kinetic
ev	evaporator
ext	external
gc	gas-cooler
i	inlet cross section, grid position
o	outlet cross section
p	potential
s	isentropic

References

[1] E. A. Groll and J. H. Kim. Review of recent advances toward transcritical CO_2 cycle technology. *HVAC and Research*, 13(3):499–520, 2007.

[2] D. M. Robinson and E. A. Groll. Theoretical performance comparison of CO_2 transcritical cycle technology versus HCFC-22 technology for a military packaged

air conditioner application. *HVAC and Research*, 6(4):325–348, 2000.

[3] M. H. Kim, J. Pettersen, and C. W. Bullard. Fundamental process and system design issues in CO_2 vapor compression systems. *Progress in Energy and Combustion Science*, 30:119–174, 2004.

[4] P. A. Domanski and D. A. Didion. Evaluation of suction-line/liquid-line heat exchange in the refrigeration cycle. *International Journal of Refrigeration*, 17(7):487–493, 1994.

[5] D. M. Robinson and E. A. Groll. Efficiencies of transcritical CO_2 cycles with an without an expansion turbine. *International Journal of Refrigeration*, 21(7):577–589, 1998.

[6] D. E. Boewe, C. W. Bullard, J. M. Yin, and P. S. Hrnjak. Contribution of internal heat exchanger to transcritical R-744 cycle performance. *HVAC and Research*, 7(2):155–168, 2001.

[7] S. G. Kim, Y. J. Kim, G. Lee, and M. S. Kim. The performance of a transcritical CO_2 cycle with an internal heat exchanger for hot water heating. *International Journal of Refrigeration*, 28:1064–1072, 2005.

[8] C. Aprea and A. Maiorino. An experimental evaluation of the transcritical CO_2 refrigerator performances using an internal heat exchanger. *International Journal of Refrigeration*, 31(6):1006–1011, 2008.

[9] Volfango Bertola. *Modelling and experimentation in two-phase flow.* Springer-Verlag Wien New York, 2003.

[10] C. D. Pérez-Segarra, J. Rigola, and A. Oliva. Modeling and numerical simulation of the thermal and fluid dynamics behavior of hermetic reciprocating compressors.Part I: Theoretical basis. *International Journal of Heat Ventilation Air Conditioning and Refrigeration Research*, 9(2):215–236, 2003.

[11] J. Rigola, C. D. Pérez-Segarra, and A. Oliva. Modeling and numerical simulation of the thermal and fluid dynamics behavior of hermetic reciprocating compressors. Part II: Experimental investigation. *International Journal of Heat Ventilation Air Conditioning and Refrigeration Research*, 9(2):237–250, 2003.

[12] J. Rigola, G. Raush, C. D. Pérez-Segarra, and A. Oliva. Detailed experimental validation of the thermal and fluid dynamic behavior of hermetic reciprocating compressors. *International Journal of Heat Ventilation Air Conditioning and Refrigeration Research*, 10(3):291–306, 2004.

[13] S. V. Patankar. *Numerical heat transfer and fluid flow.* McGraw-Hill, New York, 1980.

[14] G. Rogers and Y. Mayhen. *Reciprocating expanders and compressors.* 4th ed. Engineering thermodynamics, work and heat transfer, Longman Singapore Publishers, Singapore, 1995.

[15] C. D. Pérez-Segarra, J. Rigola, M. Soria, and A. Oliva. Detailed thermodynamic characterization of hermetic reciprocating compressors. *International Journal of Refrigeration*, 28(4):579–593, 2005.

[16] D. D. Wile. The measurement of expansion valve capacity. *Refrigeration Engineering*, 8:108–112, 1935.

Chapter 7

Conclusions and Future Actions

7.1 Concluding remarks

The present Thesis represents a summary of the work carried out by the author during the last years together with the several contributions provided by other members of the CTTC research group. The work done throughout the making of this Thesis has led to the development of a numerical platform which allows the study of vapor compression refrigeration cycles and their individual elements (e.g. heat exchangers, expansion devices, compressors).

The numerical infrastructure developed in this work has proven to be a flexible tool. It has allowed the detailed simulation of several elements and configurations which may be present in vapor compression refrigeration systems, namely connection tubes, double tube heat exchangers, single- and two-phase flow manifold systems, expansion valves, capillary tubes, compressors (from appropriate parametrizations), and single-stage vapor compression cycles with and without internal heat exchange. The numerical infrastructure has also proven to be reliable as the simulations conducted with its constitutive numerical procedures have been compared against numerical results and/or experimental data from other authors obtaining good agreement between them. Several specific conclusions have been drawn from the whole set of numerical models and simulations:

- In Chapter 2 the numerical model for two-phase flow inside tubes has been presented and verified. Two resolution procedures have been successfully implemented and compared: SIMPLE and step-by-step. The model has been used for studying the heat transfer characteristics of carbon dioxide at transcritical conditions. The experimental data reported in the technical literature shows

that the carbon dioxide transcritical heat transfer coefficient presents uncommon trends at the vicinity of the pseudo-critical temperature. Consequently, typical single-phase empirical correlations are not appropriate to be used and the importance of choosing appropriate empirical correlations becomes evident. The parametric study conducted for double tube counter flow gas-coolers working with water as the secondary fluid has shown that the heat flow increases as the mass flow rate increases but also as the inlet temperature decreases and as the heat exchanger length increases (up to a value). However, little influence is due to the carbon dioxide transcritical heat transfer coefficient particular characteristics (because the heat transfer coefficient of the annular fluid was lower than that of the refrigerant and therefore it represented a limiting condition).

- An attempt to find appropriate heat transfer coefficient correlations for in-tube ammonia evaporation at typical liquid overfeed conditions has been carried out in Chapter 3. The most relevant data from the open literature has been selected and compared against the predictions of several empirical correlations in order to compare their accuracy. The results show both an important lack on the experimental data available and large prediction discrepancies among the tested correlations. It is suggested that new experimental data are necessary to fully understand the heat transfer phenomena at such conditions and that more appropriate empirical correlations should be developed.

- In Chapter 4 a numerical model to simulate capillary tubes has been implemented and used to carry out an extensive parametric study in order to analyze the heat transfer and fluid-dynamic behavior of such devices. The influence of different aspects (metastable region, heat exchange with the suction line, length, diameter size, roughness, subcooling and superheating degree, saturation temperature, etc.) has been observed considering particular geometric and operational conditions typical of low capacity household refrigerators working with isobutane. The whole set of results represents an interesting tool for designing capillary tubes for new refrigeration applications with natural substances.

- The two-phase flow distribution model developed in Chapter 5 allows the prediction of the flow distribution (and phase split) in heat exchangers with branching tubes like manifold systems. The model has shown a good level of accuracy at single-phase conditions but a limited level of accuracy when two-phase flows were considered due to both the system phenomena complexity (different flow patterns, reverse flow, effect between consecutive junctions, phase split at junctions, etc.) and the significant amount of empirical information needed (which does not take into account all the aspects of the phenomena involved). However, the qualitative information extracted from the two-phase flow simulations (pressure profiles, mass flow rate distribution, and phase split trends) is useful

for initial predictions in a manifold system design process. The model ranges of application are closely related to the empirical information available in the literature. The model capabilities have been observed from the simulations carried out on air conditioning two-phase flow manifold systems working with carbon dioxide.

- Chapter 6 has been devoted to study conventional vapor compression refrigerating cycles working with R-134a and transcritical cycles working with carbon dioxide. The experimental data and the numerical results reported have been used to show the system behavior at transcritical conditions together with the influence of an internal heat exchanger. It has been observed that the performance of small capacity transcritical refrigerating cycles working with carbon dioxide at typical ambient temperatures is improved when an internal heat exchanger is used (the COP increases as the internal heat exchanger length increases). The results represent useful infomation for designing such equipments and show promising perspectives for the use of carbon dioxide in units with small cooling capacities. In addition to this, the experimental work carried out to acquire experimental data from the CTTC facilities has been useful to increase the CTTC research group experience in both data acquisition procedures and facilities setting up methods.

To summarize, the work achieved in this Thesis represents the synthesis of different numerical procedures to predict the thermal and fluid-dynamic aspects occurring at vapor compression cycles, as well as a further step towards a better understanding and use of natural refrigerants in vapor compression refrigerating cycles.

7.2   Future actions

The numerical infrastructure implemented throughout this Thesis together with the increased knowhow in experimental data acquisition allow a wide variety of further studies concerning numerical and experimental procedures for vapor compression refrigerating cycles and their components (heat exchangers, compressors, expansion devices, etc.). The immediate future work to be carried out is directly related to the main research topics of the CTTC group. The following aspects are currently being studied or will be tackled soon:

- The numerical procedures presented in this Thesis must be continuously fed with the latest scientific community research contributions in order to keep up to date with the latest empirical information (heat transfer, friction factor, void fraction, and T-junctions) and therefore improve the numerical procedures flexibility by extending their geometric, operational and phenomenological ranges

of application. This task is necessary due to the lack of empirical information related to the use of natural substances in refrigeration systems.

- The resolution of the whole vapor compression refrigeration unit considering the capillary tube as the expansion device follows straightforwardly from the work reported in this Thesis. The model validation will be achieved by comparing the numerical results against experimental data from both the technical literature and the CTTC facilities (which are currently equipped with capillary tubes). The numerical simulations will certainly contribute to a better understanding of the capillary tube influence in the whole cycle. Initially, the results will be focused on household refrigerators working with R-600a.

- In the medium term, the research is oriented towards the study of transient responses of the vapor compression refrigerating cycle. This topic is of great interest as many refrigerating units work under cyclic conditions (e.g. household refrigerators, working with R-600a, where the compressor continuously starts and stops). The first attempts of the CTTC research group to study transient systems have already been carried out experimentally. Additional efforts are needed to modify the numerical models of both the refrigerating cycle and its components in order to adequately simulate the thermal and fluid-dynamic phenomena occurring when transient conditions are considered.

Beyond the work summarized in the previous lines, the whole numerical infrastructure developed will remain as a flexible tool which may be adapted, extended or modified with the aim of studying any specific geometric and/or operational condition in vapor compression refrigerating cycles and their constitutive elements.

Appendices

Appendix A

Streamlines geometrical relationships

The T-junction phase split model of Hwang et al. [1] is based on dividing liquid and gas streamlines. The relationship between the distance of the dividing streamlines, a_l and a_g, and the corresponding flow areas, A_{l3} and A_{g3}, are presented for both the annular and the stratified flow pattern configurations.
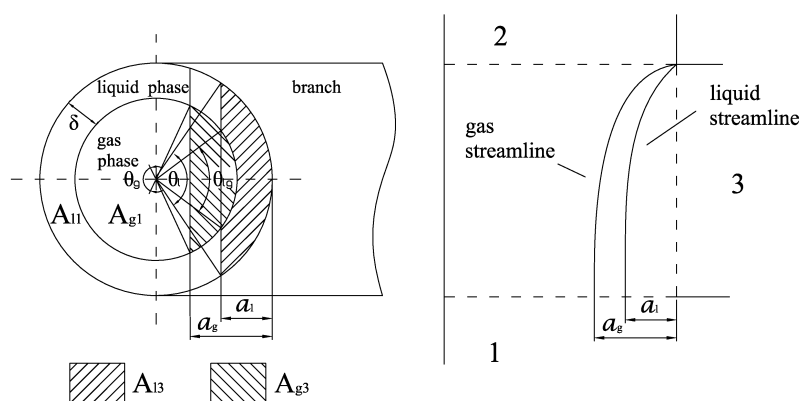
A.1 Annular geometry

Figure A.1: Dividing streamlines for gas and liquid two-phase flows (annular configuration).

Tae and Cho [2] reported a set of equations for the relationships between the dividing

streamlines and the annular geometric configuration. The liquid film thickness (δ) in the annular configuration is considered constant (see Figure A.1). Thus the gas and liquid cross-sectional areas at the T-junction inlet (A_{g1} and A_{l1}) are calculated as follows:

$$A_{g_1} = \frac{\pi}{4}(D - 2\delta)^2 \tag{A.1}$$

$$A_{l_1} = \pi\delta(D - \delta) \tag{A.2}$$

On one side, the relationships related to a_l are as follows:

$$A_{lg_3} = \frac{\theta_{lg}}{2}\left(\frac{D}{2} - \delta\right)^2 - \left(\frac{D}{2} - \delta\right)\left(\frac{D}{2} - a_l\right)sin\frac{\theta_{lg}}{2} \tag{A.3}$$

$$A_{l_3} = \frac{\theta_l}{8}D^2 - \frac{D}{2}\left(\frac{D}{2} - a_l\right)sin\frac{\theta_l}{2} - A_{lg_3} \tag{A.4}$$

Where θ_l and θ_{lg} depend on a_l:

$$\begin{cases} a_l \leq 0 & \theta_l = 0 \\ a_l \geq D & \theta_l = 2\pi \\ D > a_l > 0 & \theta_l = 2cos^{-1}\left(\frac{D - 2a_l}{D}\right) \end{cases} \tag{A.5}$$

$$\begin{cases} a_l \leq \delta & \theta_{lg} = 0 \\ a_l \geq D - \delta & \theta_{lg} = 2\pi \\ D - \delta > a_l > \delta & \theta_{lg} = 2cos^{-1}\left(\frac{D - 2a_l}{D - 2\delta}\right) \end{cases} \tag{A.6}$$

On the other side, the relationships related to a_g are as follows:

$$A_{g_3} = \frac{\theta_g}{2}\left(\frac{D}{2} - \delta\right)^2 - \left(\frac{D}{2} - \delta\right)\left(\frac{D}{2} - a_g\right)sin\frac{\theta_g}{2} \tag{A.7}$$

Where θ_g depends on a_g:

$$\begin{cases} a_g \leq \delta & \theta_g = 0 \\ a_g \geq D - \delta & \theta_g = 2\pi \\ D - \delta > a_g > \delta & \theta_g = 2cos^{-1}\left(\frac{D - 2a_g}{D - 2\delta}\right) \end{cases} \tag{A.8}$$
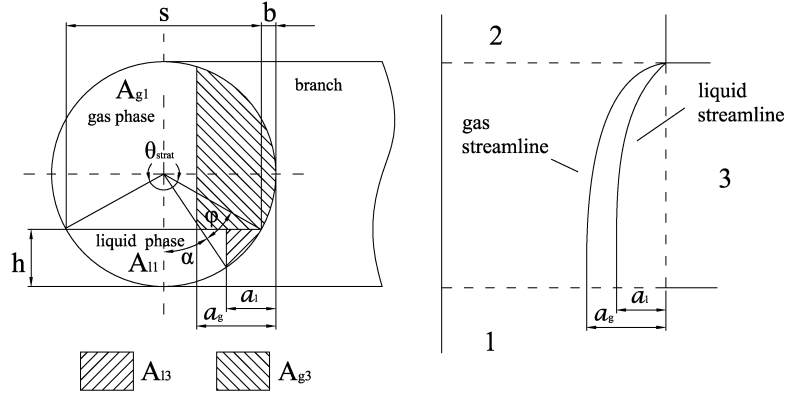
Figure A.2: Dividing streamlines for gas and liquid two-phase flows (stratified configuration).

A.2 Stratified geometry

The geometric relationships are more complex for the stratified than for the annular configuration. In the following lines the equations for the case where $\theta_{strat} \geq \pi$ are presented. The calculation of the stratified angle, θ_{strat}, the liquid height, h, and other geometric parameters are deduced as follows (see Figure A.2):

$$A_{l_1} = 0.5 \left(\frac{D}{2}\right)^2 ((2\pi - \theta_{strat}) - sin(2\pi - \theta_{strat})) \tag{A.9}$$

$$h = \frac{D}{2} - \frac{D}{2}cos\left(\frac{2\pi - \theta_{strat}}{2}\right) \tag{A.10}$$

$$s = \sqrt{1 - \left(2\frac{h}{D} - 1\right)^2} \tag{A.11}$$

$$b = \frac{1}{2}(D - s) \tag{A.12}$$

On one hand the equations related to a_l are the following:

$$A_{l_3} = \frac{(a_l - b)L}{2} + \frac{D^2}{2}\left(\frac{\phi}{2} - \frac{sin\phi}{2}\right) \tag{A.13}$$

For the case where $A_{l_3} < \frac{A_{l_1}}{2}$:

$$
\begin{cases}
a_l \leq b & L = 0 & \phi = 0 \\
a_l \geq R & L = h & \phi = \frac{2\pi - \theta_{strat}}{2} \\
b < a_l < R & L = h - R(1 - cos(\alpha)) & \phi = \frac{2\pi - \theta_{strat}}{2} - \alpha
\end{cases}
\tag{A.14}
$$

Where,

$$
\alpha = sin^{-1}\left(\frac{R - a_l}{R}\right)
\tag{A.15}
$$

And for the case where $A_{l_3} \geq \frac{A_{l_1}}{2}$:

$$
\begin{cases}
a_l \leq R & L = h & \phi = \frac{2\pi - \theta_{strat}}{2} \\
a_l \geq s + b & L = 0 & \phi = 2\pi - \theta_{strat} \\
R < a_l < s + b & L = h - (R - Rcos(\alpha)) & \phi = \frac{2\pi - \theta_{strat}}{2} + \alpha
\end{cases}
\tag{A.16}
$$

Where,

$$
\alpha = sin^{-1}\left(\frac{a_l - R}{R}\right)
\tag{A.17}
$$

On the other hand the equations related with a_g are described in the following lines. For the case where $b \leq a_g < R$:

$$
\begin{cases}
\alpha = sin^{-1}\left(\frac{R - a_g}{R}\right) \\
\phi = \frac{\theta_{strat}}{2} - \alpha \\
L = Rcos(\alpha) + R - h \\
A_{g_3} = R^2\left(\frac{\phi}{2} - \frac{sin(\phi)}{2}\right) + \frac{L(a_g - b)}{2}
\end{cases}
\tag{A.18}
$$

For the case where $R \geq a_g \leq s + b$:

$$
\begin{cases}
\alpha = sin^{-1}\left(\frac{a_g - R}{R}\right) \\
\phi = \frac{\theta_{strat}}{2} + \alpha \\
L = Rcos(\alpha) + R - h \\
A_{g_3} = R^2\left(\frac{\phi}{2} - \frac{sin(\phi)}{2}\right) + \frac{L(a_g - b)}{2}
\end{cases}
\tag{A.19}
$$

For the case where $a_g < b$:

$$
\begin{cases}
\phi = 2cos^{-1}\left(\frac{R - a_g}{R}\right) \\
A_{g_3} = R^2\left(\frac{\phi}{2} - \frac{sin(\phi)}{2}\right)
\end{cases}
\tag{A.20}
$$

For the case where $a_g > s + b$:

$$\begin{cases} \phi = 2cos^{-1}\left(\frac{a_g - R}{R}\right) \\ A_{g_3} = A_{g_1} - R^2\left(\frac{\phi}{2} - \frac{sin(\phi)}{2}\right) \end{cases} \tag{A.21}$$

Nomenclature

A	cross-sectional area, m^2
a	distance of dividing streamline, m
D	tube diameter, m
R	radius, m

Greek symbols

α	angle, rad
δ	liquid film thickness, m
θ	angle, rad
ϕ	angle, rad

Subscripts

1	dividing T-junction inlet position
2	dividing T-junction outlet position
3	dividing T-junction branch position
g	gas phase
l	liquid phase

References

[1] S. T. Hwang, H. M. Soliman, and R. T. Lahey Jr. Phase separation in dividing two-phase flows. *International Journal of Multiphase Flow*, 14(4):439–458, 1988.

[2] S. Tae and K. Cho. Two-phase split of refrigerants at T-junction. *International Journal of Refrigeration*, 29(7):1128–1137, 2006.